EDGE ION TEMPERATURE MEASUREMENT IN THE STOR-M TOKAMAK

A Thesis Submitted to the
College of Graduate Studies and Research
in Partial Fulfillment of the Requirements
for the Degree of Master of Science
in the Department of Physics and Engineering Physics
University of Saskatchewan
Saskatoon

By
Kyaw Minn Hthu

Permission to Use

In presenting this thesis in partial fulfillment of the requirements for a Postgraduate degree from the University of Saskatchewan, I agree that the Libraries of this University may make it freely available for inspection. I further agree that permission for copying of this thesis in any manner, in whole or in part, for scholarly purposes, may be granted by the professor or professors who supervised my thesis work or, in their absence, by the Head of the Department or the Dean of the college in which my thesis work was done. It is understood that any copying or publication or use of this thesis or parts thereof for financial gain shall not be allowed without my written permission. It is also understood that due recognition shall be given to me and to the University of Saskatchewan in any scholarly use which may be made of any material in my thesis.

Requests for permission to copy or to make other use of material in this thesis in whole or part should be addressed to:

Head of the Department of Physics and Engineering Physics
116 Science Place
University of Saskatchewan
Saskatoon, Saskatchewan
Canada
S7N 5E2

Abstract

A newly developed bidirectional Retarding Field Energy Analyzer, RFEA, which measures ion temperatures from both sides (downstream and upstream), was commissioned in the STOR-M tokamak. Its entrance slit width follows one of the design criteria, $< 2\lambda_{De}$. The dimension of the RFEA is small enough to avoid creating a shadow effect. The probe is the replacement of previous RFEA which measures ion temperature, T_i, from one side only. An external cable used as an antenna parallel to the cables, connected to the collector, is used to suppress noise picked up by the cable. A similar technique was used in the previous RFEA. By operating the probe in standard ramping mode, T_i in the scrape-off layer (SOL) region between 15.5cm and 12cm from the chamber center is measured (minor radius). The probe performs T_i measurement campaign twice with different entrance slits. The entrance slit 1 provides higher collector current than the entrance slit 2, but the entrance slit 1 on the downstream side did not survive during the first T_i campaign. T_i measured by the entrance slit 2 in the SOL region of the STOR-M is between 19eV and 34eV. The probe operation is validated by T_e values simultaneously measured by the Triple probe. $\frac{T_i}{T_e}$ is between 1.8 and 2.8 in the STOR-M SOL. RFEA in DC mode operation demands higher ion current to estimate T_i fluctuation. The 2011 T_i campaign shows that the direction of magnetic field largely affects the current RFEA operation both in conventional ramping mode and in DC mode.

Acknowledgements

First of all, my grateful thanks to my supervisor, Dr. Akira Hirose, whose encouragement, guidance, and support throughout enabled me to complete this thesis. Dr. Hirose also renewed my funding, semester after semester, while I was setting up the second experiment. I had fruitful discussions with Dr. Chijin Xiao with regard to probe design and data analyzing technique. This thesis would not have been possible without the knowledge of choosing material for the probe design and electronics from Dave Mccoll. I would like to thank Ted Toporowski, Perry Balon, and Blair Chomyshen, in the machine shop, Department of Physics and Engineering Physics, for making the probe design possible. I would like to express my gratitude to former graduate student Damain Rohraff for passing on his knowledge of material, and Solidworks 3D CAD program. To Mykola Dreval, who made simultaneous measurements of electron temperatures possible, and also thank him for DC mode measurement. I want to thank Yue Ding for her data. I profited from discussions with Kurt Kruger regarding data analyzing technique and the paper he forwarded to me. I want to thank Dr. Brian P. Colquhoun for his proofreading. I offer my regards to the entire STOR-M team who supported me in so many aspects during the completion of the project. This research was sponsored by the Natural Sciences and Engineering Research Council (NSERC) of Canada and the Canada Research Chair (CRC) program.

Dedicated to my family

Contents

List of Tables

List of Figures

List of Abbreviations

DAQ	Data acquisition system
e	electron temperature measurement mode. V_{G1} and V_{G2} are reversed from ion mode.
he	hot electron
hi	hot ion
i	ion
ion mode	ion temperature measurement mode. The electrical configuration is shown in Fig.2.1.
ISO-AMP	isolation amplifier. The circuit is shown in Fig.6.4.
IST	Instituto Superior Tcnico.
$I-V$	current-voltage characteristic curve
JET	Joint European Torus
PIC	Particle In Cell simulation
RC	resistance capacitor time constant
RFEA	Retarding Field Energy Analyzer
SOL	Scrape-off layer region
STOR-M	Saskatchewan Torus-Modified
Tokamak	Toroidal Chamber with Magnetic Coils

Symbols

a	minor radius of the plasma column (m)
a_0	minor radius of the STOR-M tokamak (m)
$\mathbf{B}$	magnetic field (Wb)
B_θ	poloidal magnetic field (Wb)
B_ϕ	toroidal magnetic field (Wb)
$c_s, \sqrt{\frac{kT_e}{m_i}}, \sqrt{\frac{eT_e(\mathrm{eV})}{m_i}}$	ion sound speed ($\mathrm{m\,s^{-1}}$)
Down i_c	the current collected from the downstream analyzer (A)
$D_\perp^{amb}$	cross-field diffusion coefficient ($\mathrm{m^2\,s^{-1}}$)
e, q	electronic charge (C)
i_c	collector current (A)
i_{G2}	current at the grid 1 (A) (in DC mode)
I_p	plasma current (A)
k	Boltzmann constant ($\mathrm{m^2\,kg\,s^{-2}\,K^{-1}}$)
m_e	electron mass (kg)
m_i	ion mass (kg)
n_e	electron density in plasma ($\mathrm{m^{-3}}$)
n_i	ion density ($\mathrm{m^{-3}}$)
n_0	density of particles (either electrons or ions) at the sheath edge or in plasma ($\mathrm{m^{-3}}$)
r_c	minor radius of the tokamak chamber (cm)
$r_{Le}, \frac{m_e v_\perp}{eB}$	electron Larmor radius (m)
$r_{Li}, \frac{m_i v_\perp}{eB}$	ion Larmor radius (m)
R_0	major radius of the STOR-M tokamak (m)
s	entrance slit width(m)
T_e	electron temperature (K)
$T_e(\mathrm{eV}), \frac{kT_e}{e}$	electron temperature (eV)
$T_{e0}(\mathrm{eV})$	unperturbed electron temperature (eV)
T_i	ion temperature (K)
$T_i(\mathrm{eV}), \frac{kT_i}{e}$	ion temperature in eV (eV)
$T_i^d(\mathrm{eV}), \frac{kT_i^d}{e}$	ion temperature measured by the downstream analyzer in eV (eV)
$T_{i0}(\mathrm{eV})$	unperturbed ion temperature (eV)
$T_i^u(\mathrm{eV}), \frac{kT_i^u}{e}$	ion temperature measured by the upstream analyzer in eV (eV)
Up i_c	current collected from the upstream analyzer (A)
$v_{ix}, v_{iy}, \& v_{iz}$	ion velocity in $x, y, \& z$ directions ($\mathrm{m\,s^{-1}}$)
$v_\parallel, v_x$	velocity of a particle in the parallel, x, direction of magnetic field ($\mathrm{m\,s^{-1}}$)
$v_\perp, \sqrt{v_y^2 + v_z^2}$	velocity of a particle in the perpendicular, $x - y$, direction of magnetic field ($\mathrm{m\,s^{-1}}$)

v_{Te}, $\sqrt{\frac{kT_{e0}}{m_e}}$	electron thermal velocity ($\mathrm{m\,s^{-1}}$)
v_{Ti}, $\sqrt{\frac{kT_{i0}}{m_i}}$	ion thermal velocity ($\mathrm{m\,s^{-1}}$)
V_{en}	voltage externally applied at the entrance slit (V)
V_{G1}	voltage externally applied at the grid 1 (V)
$V_{shift} = \phi_p - V_{en}$	knee potential of $i_c - V_{G1}$ characteristic curve caused by the combined action of the plasma potential and the entrance slit potential (V)
λ_{De}, $\sqrt{\frac{\epsilon_0 kT_e}{e^2 n_0}}$	electron Debye length (m)
λ_{Di}, $\sqrt{\frac{\epsilon_0 kT_i}{e^2 n_0}}$	ion Debye length (m)
δ	sheath thickness (m) in Appendix.A.3. percentage error in Chap.2.3
δ_{en}	entrance slit thickness (m)
ϕ	electric potential (V)
ϕ_f	floating potential (V)
ϕ_p	plasma potential (V)
ϕ_{pre}	presheath potential (V)
ϕ_{she}	sheath potential (V)
τ, $\frac{T_{i0}}{T_{e0}}$	ratio of ion temperature at the sheath edge to electron temperature at the sheath edge
τ_i, $\frac{T_i}{T_{i0}}$	ratio of ion temperature at a point with respect to the ion temperature at the sheath edge
τ_E	energy confinement time (s)
θ	direction of magnetic field on the $x - z$ plane (°)

Chapter 1

Introduction

Due to an increasing demand for energy coupled with rising environmental and sustainability issues, the requirement for abundant clean energy is becoming critical. Nuclear fusion offers the world the potential for an abundant and clean source of power [1][2]. It is a leading candidate amongst all forms of alternative energy to meet the world's rising demands [3].

1.1 Principle of Fusion Reactor

In the sun, the energy is mainly obtained from a cycle of proton-proton reactions [4]. They can be summarized as

$$\begin{aligned} \mathrm{p} + \mathrm{p} &\rightarrow \mathrm{D} + \mathrm{e}^{+} + 2\nu_e + 0.42\mathrm{MeV} \\ \mathrm{D} + \mathrm{p} &\rightarrow \mathrm{He}_2^3 + \gamma + 5.5\mathrm{MeV} \\ \mathrm{He}_2^3 + \mathrm{He}_2^3 &\rightarrow \mathrm{He}_2^4 + 2\mathrm{p} + 12.86\mathrm{MeV} \end{aligned} \tag{1.1}$$

where p represents protons, e^{+} represents positrons, and ν_e represents neutrinos. The cross sections of these reactions are small. In practice, reactions with larger cross sections are needed. The reaction with the largest cross section at 10 keV temperatures is a mix of two isotopes of hydrogen, deuterium (D) and tritium (T), which produces a neutron (n) and a helium-4 nucleus (α):

$$\mathrm{D}+\mathrm{T}\rightarrow\mathrm{n}(14.1\mathrm{MeV}) + \alpha(3.5\mathrm{MeV})$$

In this reaction, the neutron contains 14MeV energy and α 3.5MeV. Tritium does not occur in nature as it decays with a short twelve year half-life to helium-3. Thus it must be

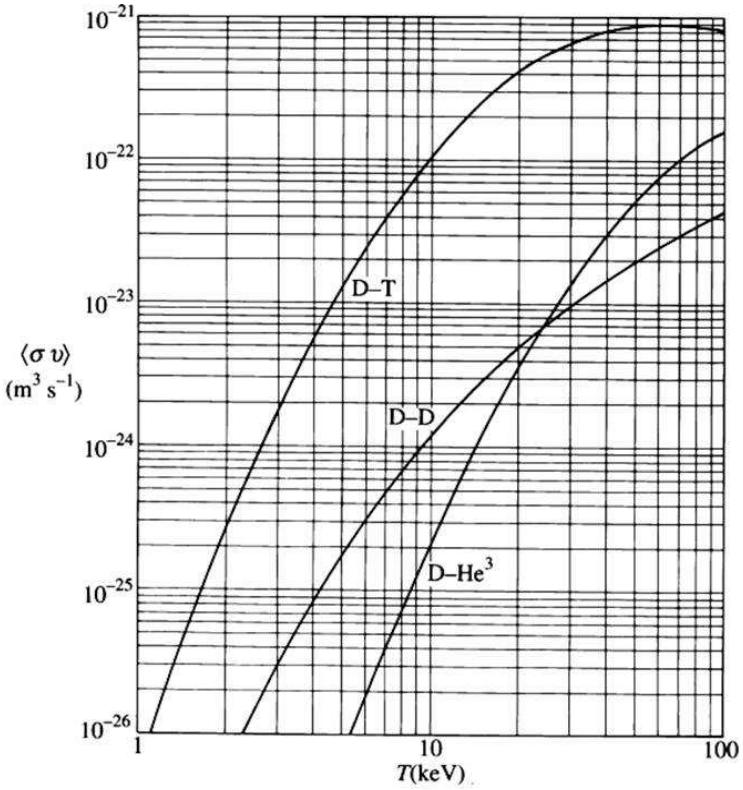

Figure 1.1: Reaction rate parameters for nuclear fusion reactions with the highest cross section in keV (image courtesy of `http://fds.oup.com/www.oup.com/pdf/13/9780198509226.pdf`).

"bred" from lithium, Li, using the neutron produced in the deuterium-tritium, DT, fusion reaction.

$$\mathrm{Li}^6 + \mathrm{n} \rightarrow \alpha + \mathrm{T} + 4.8\mathrm{MeV} \tag{1.2}$$

A neutron causes a tritium breeding (see Fig.1.2) reaction with the isotope lithium-6, which comprises roughly 75% of naturally occurring lithium [3]. DT reaction has greatest cross section. It needs at least 10keV to overcome electrostatic repulsion. The reaction rate, $\langle \sigma v \rangle$, for DT reaction is $10^{-22}\mathrm{m}^3\,\mathrm{s}^{-1}$.

The Lawson criterion for DT fusion, $n\tau_E > 10^{20}\mathrm{s\,m}^{-3}$ at temperature, T=10keV, can be derived from the condition, fusion power>energy loss. For fusion energy gain, the energy out must exceed the energy in. For an equal mix of deuterium and tritium fuel, $n_D = n_T = \frac{n_e}{2}$ and $n_D + n_T = n_e$. The energy out, E_f, is given by

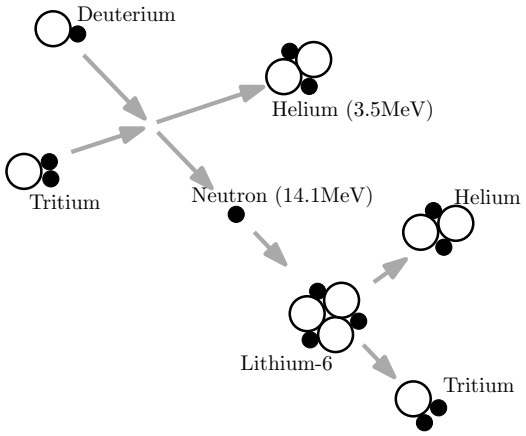

Figure 1.2: The processes of D-T reaction and tritium breeding.

$$E_f = n_D n_T \langle \sigma \upsilon \rangle E \tau_E = (\frac{n_e}{2})(\frac{n_e}{2}) \langle \sigma \upsilon \rangle E \tau_E \tag{1.3}$$

where $\langle \sigma \upsilon \rangle$ represents reaction rate in $\mathrm{m^3\,s^{-1}}$, τ_E represents confinement time in s, n_e is the electron density in $\mathrm{m^{-3}}$, and E is the energy of the charged fusion products in J. Eq.1.3 must exceed the energy required to heat the plasma to the temperature required for fusion, E_t:

$$E_t = 2 \times \frac{3}{2} n_e k T \tag{1.4}$$

where E represents energy per reaction (symbol E used also as electric field in Appendix.A.3), k represents Boltzmann constant, and T is temperature in K. For fusion energy gain, $\frac{E_f}{E_t} > 1$:

$$\begin{aligned} \left(\frac{n_e}{2}\right)\left(\frac{n_e}{2}\right) \langle \sigma \upsilon \rangle E \tau_E &> 2 \times \frac{3}{2} n_e k T \\ n_e \tau_E &> \frac{12kT}{\langle \sigma \upsilon \rangle E} \quad \text{or} \quad \frac{12T(\mathrm{eV})}{\langle \sigma \upsilon \rangle E(\mathrm{eV})} \end{aligned} \tag{1.5}$$

By including the temperature in the above inequality, the triple product becomes

$$n_e T \tau_E > \frac{12T^2(\mathrm{eV})}{\langle \sigma \upsilon \rangle E(\mathrm{eV})} \tag{1.6}$$

Referring to Fig.1.1, for a temperature of 10keV, $\langle \sigma \upsilon \rangle \approx 10^{-22} \mathrm{m^3\,s^{-1}}$, and $E \approx 17.6$MeV, the characteristics must satisfy the following criterion:

$$
\begin{aligned}
nT\tau_E &> 10^{21}\mathrm{keV\,s\,m^{-3}} \\
\text{or} \qquad n\tau_E &> 10^{20}\mathrm{s\,m^{-3}} \qquad (1.7)
\end{aligned}
$$

In fusion research, two methods, magnetic confinement fusion (MCF) and inertial confinement fusion (ICF), have been pursued in the quest for a viable fusion reactor. MCF tries to confine the plasma at low densities, $\approx 10^{20}\mathrm{m}^{-3}$, for the relatively long times of several seconds, $\approx$ 10s, whereas ICF yields to achieve extremely high densities, $\approx 10^{32}\mathrm{m}^{-3}$, for a very short time, $\approx 10^{-11}$s [4].

In the ICF scheme, a pellet which contains a mixture of deuterium and tritium is compressed to very high densities and temperatures by applying strong external forces. To compress and heat the fuel, high energy-beams of laser light or ion beams are irradiated to heat the outer layer of the target symmetrically. The outer shell explodes. As the outer part of the shell blasts off, the fuel is strongly accelerated toward the center of the sphere, as a consequence of momentum conservation. As the fuel implodes toward the center of the capsule, it is compressed to high densities and thermonuclear fusion [4].

1.2 Magnetic Confinement

Due to Lorentz force, $\mathbf{v} \times \mathbf{B}$, particles (such as fuel ions) will gyrate around the magnetic field lines as shown in Fig.1.3. Reactor concepts based on this approach are referred to as "magnetic confinement fusion". The following paragraphs discuss how a magnetic field confines charged particles.

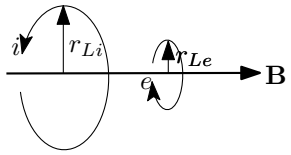

Figure 1.3: Electron and ion with magnetic field line.

A single particle of charge, e, and mass, m, moving with velocity, $\mathbf{v}$, in a magnetic field, $\mathbf{B}$, experiences the Lorentz force, $\mathbf{F}$:

$$\mathbf{F} = e(\mathbf{v} \times \mathbf{B}) \tag{1.8}$$

Since the direction of the force is given by the cross product of the velocity and magnetic field, the Lorentz force will always act perpendicular to the direction of motion, causing the particle to gyrate around the magnetic field line with Larmor radii:

$$\begin{aligned} r_{Le} &= \frac{m_e v_\perp}{eB} \\ r_{Li} &= \frac{m_i v_\perp}{eB} \end{aligned} \tag{1.9}$$

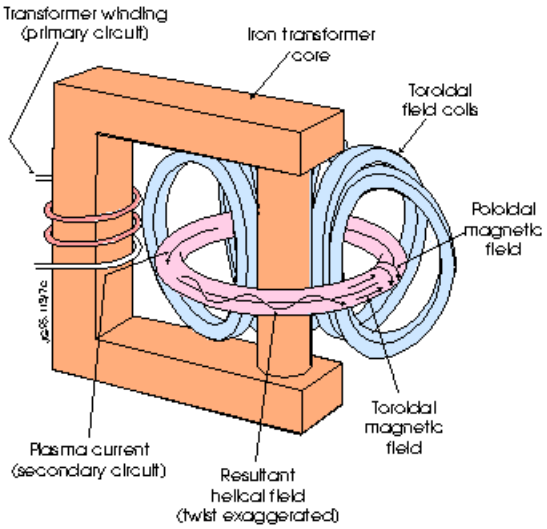

Figure 1.4: Schematic of main components of a tokamak (image courtesy of `http://www.michaelcapewell.com/creative_content/fusion.htm`).

where r_{Le} and r_{Li} are the electron Larmor radius and ion Larmor radius respectively. $v_\perp$ is the particle velocity with direction perpendicular to the magnetic field. The magnetic field thus confines charged particles by restricting their motion. If the two ends of the magnetic field lines are connected, a toroidal confinement system may be realized. Unfortunately, a simple toroidal magnetic field is unable to confine a plasma. A schematic diagram of a tokamak is shown in Fig.1.4.

1.3 Tokamak Equilibrium

The concept of tokamak was conceived by Sakharov and Tamm in the 1950's [5]. Closed magnetic confinement devices must be "toroidal" in a topological sense. A simple toroidal magnetic field is unable to confine a plasma because the magnetic curvature/gradient causes magnetic drifts of electrons and ions in opposite directions which creates a vertical electric field $E_\perp$. This in turn let the plasma $\mathbf{E} \times \mathbf{B}$ drift radially outward and the plasma is lost to the vacuum chamber wall.

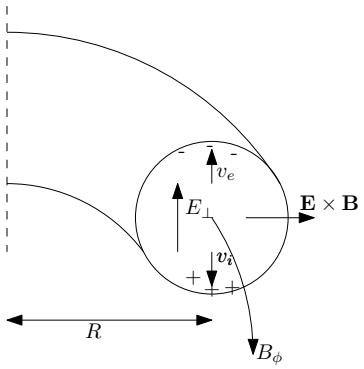

Figure 1.5: $\mathbf{E} \times \mathbf{B}$ drift.

$$\begin{aligned} v_{Di} &= -\frac{2T_i}{eB_\phi R} \\ v_{De} &= \frac{2T_e}{eB_\phi R} \end{aligned} \tag{1.10}$$

If a "poloidal" magnetic field B_θ is added, either externally (as in a stellarator) or internally (as in a tokamak) by a toroidal current J_ϕ, closed, nested magnetic surfaces can be formed. For a confined plasma to be in equilibrium, the following equilibrium condition must be satisfied,

$$-\nabla p + \mathbf{J} \times \mathbf{B} = \mathbf{0} \tag{1.11}$$

where p is the plasma pressure and $\mathbf{J} \times \mathbf{B}$ is the magnetic Lorentz force. Since

$$\mathbf{J} = \frac{1}{\mu_0} \nabla \times \mathbf{B}, \tag{1.12}$$

by plugging Eq.1.12 into Eq.1.11, and by using the vector relation, $\mathbf{B}\times(\nabla\times\mathbf{B})+(\mathbf{B}\cdot\nabla)\mathbf{B} = \nabla(\frac{B^2}{2})$ [6], Eq.1.11 can be written as

$$\nabla\left(p+\frac{B^2}{2\mu_0}\right)=\frac{1}{\mu_0}(\mathbf{B}\cdot\nabla)\mathbf{B} \tag{1.13}$$

This indicates that the total pressure gradient (plasma+magnetic) is to be balanced by a magnetic curvature. Considering the minor radial component of Eq.1.13, and noting the curvature term $(\mathbf{B}\cdot\nabla\mathbf{B})_r = -\frac{B_\theta^2}{r}$ (B_z is assumed to be straight) [3], the previous equation then leads to

$$\frac{\partial}{\partial r}\left(p+\frac{B_\theta^2}{2\mu_0}+\frac{B_z^2}{2\mu_0}\right)=-\frac{1}{\mu_0}\frac{B_\theta^2}{r} \tag{1.14}$$

Eq.1.14 can be arranged as

$$\frac{\partial}{\partial r}\left(p+\frac{B_z^2}{2\mu_0}\right)=-\frac{1}{2\mu_0}\frac{1}{r^2}\frac{\partial}{\partial r}(rB_\theta)^2 \tag{1.15}$$

If Eq.1.15 is multiplied by r^2, it can be integrated from the axis to the plasma edge ($r = 0$ to $r = a$), obtaining the basic equilibrium equation.

In a simple tokamak with circular cross-section, Eq.1.15 yields the following condition,

$$\overline{p}+\frac{1}{2\mu_0}\left[\overline{B_\phi^2}-\overline{B_\phi^2(a)}\right]=\frac{1}{2\mu_0}B_\theta^2(a) \tag{1.16}$$

where $\overline{p}$ is the pressure averaged over the plasma cross section,

$$\overline{p}=\frac{1}{\pi a^2}\int_0^a p(r)2\pi r dr \tag{1.17}$$

Likewise

$$\overline{B_\phi^2}=\frac{1}{\pi a^2}\int_0^a B_\phi^2(r)2\pi r dr \tag{1.18}$$

and $B_\theta(a)$ is the poloidal magnetic field at the plasma edge,

$$2\pi a B_\theta(a)=\mu_0 I_p=\mu_0\int_0^a J_\phi(r)2\pi r dr \tag{1.19}$$

In tokamak discharges created by Ohmic heating alone, the so-called poloidal beta, defined by

$$\beta_\theta = \frac{\overline{p}}{\frac{1}{2\mu_0} B_\theta^2(a)} \tag{1.20}$$

is approximately 0.5.

The force balance condition given in Eq.1.16 is for the minor radius direction. For the major radius (R) direction, another magnetic field, the vertical magnetic field $B_\perp$, is required. This is given by

$$B_\perp = \frac{\mu_0 I_p}{4\pi R}\left[\ln\left(\frac{8R}{a}\right) + \beta_\theta + \frac{l_i}{2} - \frac{3}{2}\right] \tag{1.21}$$

where l_i is the internal inductance parameter. (For uniform plasma current, $l_i = 0.5$, and for a skin current profile, $l_i < 0.5$.)

Another basic property of magnetically confined plasmas is charge neutrality:

$$\nabla \cdot \mathbf{J} = 0 \tag{1.22}$$

where $\mathbf{J}$ is the current density in the plasma. Plasma confinement is realized by the current perpendicular to the magnetic field,

$$\mathbf{J}_\perp = \frac{\mathbf{B} \times \nabla p}{B^2} \tag{1.23}$$

Charge neutrality condition $\nabla \cdot \mathbf{J} = 0$ requires

$$\nabla \cdot \mathbf{J}_\parallel + \nabla \cdot \left(\frac{\mathbf{B} \times \nabla p}{B^2}\right) = 0 \tag{1.24}$$

Eq.1.24 can be integrated as

$$J_\parallel = -\frac{2r}{RB_\theta}\frac{dp}{dr}\cos\theta \tag{1.25}$$

where its divergence form is

$$\nabla_\parallel \cdot \mathbf{J}_\parallel = \frac{1}{qR}\frac{\partial J_\parallel}{\partial \theta} \tag{1.26}$$

A MHD treatment is applicable to diffusion phenomena when the electron-to-ion collision frequency is large and the mean free path is shorter than the connection length of the inside regions of good curvature and the outside region of bad curvature of the torus; i.e.,

$$\begin{aligned} \frac{v_{Te}}{\nu_{ei}} &\lesssim \frac{2\pi R}{\iota} \\ \nu_{ei} &\gtrsim \frac{1}{R}\frac{\iota}{2\pi} v_{Te} \end{aligned} \tag{1.27}$$

where v_{Te} is electron thermal velocity and ν_{ei} is electron to ion collision frequency. From Ohm's law

$$\mathbf{E} + \mathbf{v} \times \mathbf{B} - \frac{1}{en}\nabla p_i = \eta \mathbf{j}, \tag{1.28}$$

the motion of plasma across the lines of magnetic force is expressed by

$$\begin{aligned} n\mathbf{v}_\perp &= \frac{1}{B}\left(\left(n\mathbf{E} - \frac{kT_i}{e}\nabla n\right) \times \mathbf{b}\right) - \frac{m_e \nu_{ei}}{e^2}\frac{\nabla p}{B^2} \\ &= \frac{1}{B}\left(\left(n\mathbf{E} - \frac{kT_i}{e}\nabla n\right) \times \mathbf{b}\right) - r_{Le}^2 \nu_{ei}\left(1 + \frac{T_i}{T_e}\right)\nabla n \end{aligned} \tag{1.29}$$

If the first term in the right-hand side can be neglected, the classical diffusion coefficient D is given by

$$D = r_{Le}^2 \nu_{ei}\left(1 + \frac{T_i}{T_e}\right) \tag{1.30}$$

However the first term of the right-hand side of Eq.1.29 is not always negligible. In toroidal configuration, the charge separation due to the toroidal drift is not completely cancelled along the magnetic field lines and an electric field E arises. Therefore the $\mathbf{E} \times \mathbf{b}$ term in Eq.1.29 contributes to the diffusion.

If the electric conductivity along the lines of magnetic force is $\sigma_\parallel$, the parallel electric field is $E_\parallel = \frac{J_\parallel}{\sigma_\parallel}$. The relation

$$\frac{E_\theta}{E_\parallel} \approx \frac{B}{B_\theta} \tag{1.31}$$

holds. From $\frac{B_\theta}{B} \approx \frac{r\iota}{2\pi R}$, the θ component of the electric field is given by

$$E_\theta = \frac{B}{B_\theta} E_\theta = \frac{2\pi R}{r\iota\sigma_\parallel} J_\parallel = \frac{2}{\sigma_\parallel} \frac{R}{r} \left(\frac{2\pi}{\iota}\right)^2 \frac{1}{B} \frac{\partial p}{\partial r} \cos\theta \tag{1.32}$$

Accordingly Eq.1.32 is reduced to

$$\begin{aligned} nv_r &= -n\frac{E_\theta}{B} - r_{Le}^2 \nu_{ei} \left(1 + \frac{T_i}{T_e}\right) \frac{\partial n}{\partial r} \\ &= -\left(\frac{R}{r} 2 \left(\frac{2\pi}{\iota}\right)^2 \frac{nkT_e}{\sigma_\parallel B^2} \cos\theta \left(1 + \frac{r}{R}\cos\theta\right) + \frac{nkT_e}{\sigma_\perp B^2} \left(1 + \frac{r}{R}\cos\theta\right)^2\right) \\ &\quad \times \left(1 + \frac{T_i}{T_e}\right) \frac{\partial n}{\partial r} \end{aligned} \tag{1.33}$$

Noting that the area of a surface element is dependent of θ, and taking the average of nv_r over θ, we find that

$$\begin{aligned} \langle nv_r \rangle &= \frac{1}{2\pi} \int_0^{2\pi} nv_r \left(1 + \frac{r}{R}\cos\theta\right) d\theta \\ &= -\frac{nkT_e}{\sigma_\perp B^2} \left(1 + \frac{T_i}{T_e}\right) \left(1 + \frac{2\sigma_\perp}{\sigma_\parallel} \left(\frac{2\pi}{\iota}\right)^2\right) \frac{\partial n}{\partial r} \end{aligned} \tag{1.34}$$

where the electric conductivity perpendicular to the magnetic field is $\sigma_\perp = \frac{ne^2}{m_e \nu_{ei}}$. Using the relation $\sigma_\perp = \frac{\sigma_\parallel}{2}$, we obtain the diffusion coefficient of a toroidal plasma:

$$D_{ps} = \frac{nT_e}{\sigma_\perp B^2} \left(1 + \frac{T_i}{T_e}\right) \left(1 + \left(\frac{2\pi}{\iota}\right)^2\right) \tag{1.35}$$

The above derivation follows [7]. The current $J_\parallel$ is known by Pfirsch-Schlüter current which enhances the classical collisional diffusivity Eq.1.30 by a factor,

$$D_{ps} = D(1 + q_s^2) \tag{1.36}$$

where $q_s = \frac{r_0 B}{R B_\theta} = \frac{2\pi}{\iota}$ is the safety factor, $r_{Le} = \frac{v_{Te}}{\omega_c}$ is the electron (thermal) Larmor radius, and ν_{ei} is the collision frequency. The safety factor $q_s(a)$ of the STOR-M tokamak is usually about 4 [8]. As the plasma temperature increases, the tokamak discharge approaches the banana regime

$$D_{Banana} = \frac{\nu_{ei} r_{Le}^2 q_s^2}{\epsilon^{\frac{3}{2}}} \tag{1.37}$$

where $\epsilon = \frac{r}{R}$ is the inverse aspect ratio.

1.4 Current Status of Tokamak Research

The breakeven condition,

$$Q = \frac{\text{fusion power output}}{\text{heating power}} > 1 \tag{1.38}$$

has been demonstrated in JET and JT-60 (Deuterium plasma was used in those tokamaks, and $Q \gtrsim 1$ was based on the assumption that DT plasma would behave without causing surprises). The next generation of tokamak research is demonstration of burning plasma (DT plasma) in which fusion product particle, He^{++} (3.5MeV), heats fusion fuels through collisions (α particles mainly heat electrons which in turn heat ions). When born, α particles hardly have Maxwellian distributions and they may cause high energy ion plasma instabilities. ITER will be operated at $Q = 5 \sim 10$ (burning plasma). At ignition, $Q = \infty$.

The performance of ITER will be influenced by various factors including suppression of ELM (edge localized mode) [9], bootstrap current [6]

$$J_{BS} = -\frac{\sqrt{\epsilon}}{eB_\theta} \frac{dp_e}{dr} \tag{1.39}$$

and accumulation of impurities at the plasma core. Fueling the core region of ITER remains unsolved problem.

The roles of the toroidal flow and its shear have been recognized in plasma stability problems. The toroidal flow velocity is related to the radial electric field and ion pressure gradient.

1.5 The Radial Force Balance Equation

Let's consider the fluid equation of motion for ions.

$$m_i n_i[\frac{\partial \mathbf{v}}{\partial t} + (\mathbf{v}\cdot\nabla)\mathbf{v}] = q n_i[\mathbf{E} + \mathbf{v}\times\mathbf{B}] - \nabla p_i \tag{1.40}$$

where m_i is the ion mass, n_i is ion density, $\mathbf{v}$ is plasma velocity, q is ion charge, p_i is ion pressure, $\mathbf{E}$ is electric field, and $\mathbf{B}$ is magnetic field. For slow drifts compared with ion cyclotron frequency $\omega_{c,i}$, time derivative of velocity, $\frac{\partial}{\partial t}$, can be neglected. If we neglect the convection term, $(\mathbf{v}\cdot\nabla)\mathbf{v} = 0$. The derivation follows [8]. Then the equation of motion can be written as

$$q n_i[\mathbf{E} + \mathbf{v}\times\mathbf{B}] - \nabla p_i = 0 \tag{1.41}$$

Eq.1.41 can be used to derive the radial force balance equation for a tokamak plasma

$$E_r = \frac{1}{q n_i}\frac{\partial p_i}{\partial r} + v_\phi B_\theta - v_\theta B_\phi \tag{1.42}$$

where the subscripts r, θ, and ϕ, represent the radial, poloidal, and toroidal directions respectively. Eq.1.42 indicates that the toroidal flow velocity is related to the radial electric field and ion temperature, $p_i = n_i k T_i$. The Rake probe measures ion density and radial electric field. The Gundestrup probe provides perpendicular and parallel flow velocities. A magnetic probe provides the magnetic field, and the RFEA measures ion temperature.

1.6 Edge Physics

An important part of the edge plasma is the SOL region. It is defined as the outer layer of a magnetically confined plasma, where the field lines come in contact with a material surface (such as a divertor or limiter). The definition of SOL region of divertor tokamak and limiter tokamak are shown in Fig.1.6. RFEA measures T_i in SOL region.

1.7 Motivation

There are several plasma diagnostic tools for SOL T_i measurements, e.g., plasma ion mass spectrometer [10], RFEA [11][12][13][14][15][16][17], Kasumata tunnel probe [18], $\mathbf{E}\times\mathbf{B}$ analyzer, rotating double probe, carbon resistance probe, and surface collection probe [19].

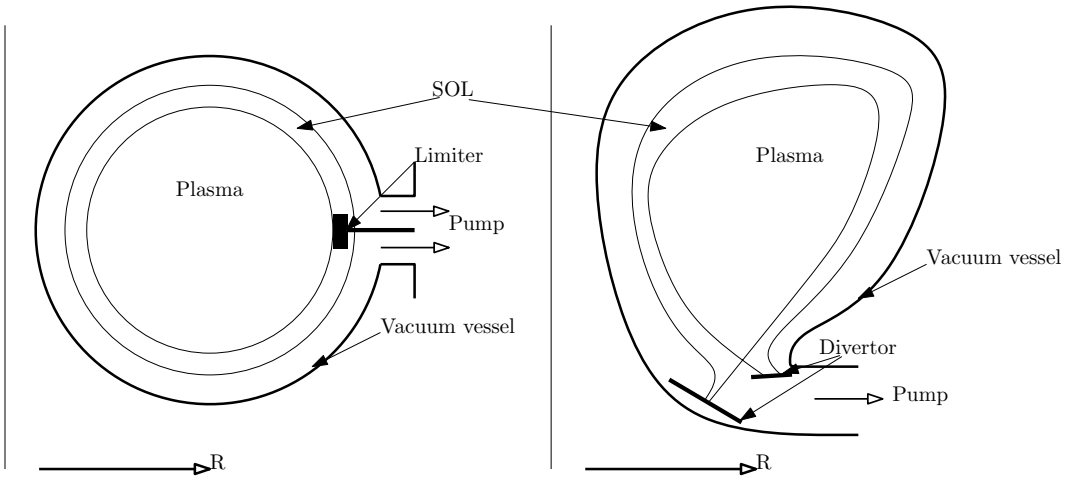

Figure 1.6: SOL concepts of the poloidal plane of limiter tokamak (left) and divertor tokamak (right).

The straightforward data interpretation makes a RFEA one of the only widely accepted diagnostics for SOL T_i measurements. For example, to measure parallel ion temperature, $T_{i,\parallel}$, in Kasumata tunnel probe, the precise relation between the ratio of the current at the two tunnel segments, $\frac{I_{i,2}}{I_{i,1}}$, has to be determined by PIC simulation of that probe (see Chap.3.5). Extensive shadow effect for RFEA (Chap.2.5) is also studied in a number of tokamaks [20][21][10][13][8]. Moreover, most of the newly developed diagnostics only demonstrate the capability to measure SOL T_i. Systematic studies of SOL T_i are very rare.

1.8 Goals of the Thesis

A compact, simple, and economical RFEA was developed for investigations of ion temperature in the SOL region of the STOR-M tokamak. The objective of this thesis is to demonstrate the utility of the newly developed bidirectional RFEA as an SOL T_i diagnostic in the STOR-M tokamak.

1.9 Organization of the Thesis

This thesis includes the followings: the background principle for modeling of a RFEA (Chap.2), T_i profile, T_e measured by the RFEA in electron mode validated by the Triple

probe, and the importance of magnetic field direction on T_i measurements (Chap.4), and the mechanical structure and electronics of the RFEA (Chap.5 and Chap.6). Appendices include broad discussion about sheath theory with and without magnetic field, and Matlab data analyzing code used for T_i estimation.

In brief, this thesis provides the operation of RFEA in the STOR-M tokamak, and it focuses on the validation of the RFEA T_i measurement.

Chapter 2

Principle of RFEA

2.1 Introduction

Measurements of SOL T_i are rare. The most widely accepted diagnostic for SOL T_i measurements is the retarding field energy analyzer, RFEA. Design of a RFEA has to follow two criteria: (1) An entrance slit width should be less than 2 Debye length. (2) The surface area, A, of a RFEA should follow the condition, $\frac{c_s A}{16 D_{\perp}^{amb}} < L_{\parallel}$. RFEA can be operated in two modes, standard ramping mode and DC mode. In standard ramping mode, ions are transmitted through a slit into the analyzer and their parallel velocity distribution is analyzed by means of a retarding electric field applied at a grid. The collected current gives the $I - V$ characteristic curve and the slope of $I - V$ curve provides ion temperature information. In DC mode, current ratio at two points on the exponentially decaying region of $I - V$ curve with two different dc biases applied at two different electrodes gives T_i value.

2.2 Standard Ramping Mode

The sheath at the entrance slit repels electrons and accelerates ions into the analyzer. The voltage at grid 1, V_{G1}, is swept, only ions with energy greater than qV_{G1} will be collected, so that the logarithmic slope of the collected current should give the ion temperature. The lowest negative bias is applied to the grid 2, so that the grid 2 suppresses the secondary electrons emitted from the collector or from either of the two grids due to ion impact. It also repels residual high energy electrons coming from the entrance slit. The collector is negative (but not as much as the grid 2) ensuring good ion collection as shown in Fig.2.1.

A question arises. Why cannot simple Langmuir probes measure T_i? In Langmuir probe,

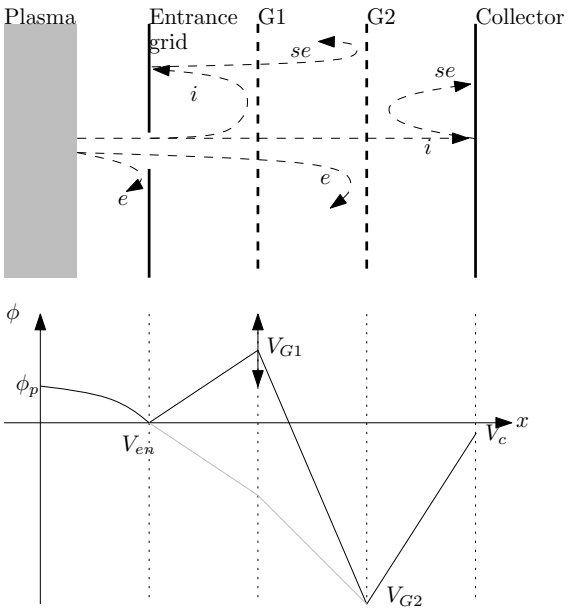

Figure 2.1: Top: schematic diagram of a RFEA. Bottom: biasing scheme for a RFEA

ion and electron are determined by the electron temperature, ion temperature information cannot be provided because of sheath formation.

The ion collector current, i_c, is a measure of the integral ion parallel velocity distribution:

$$i_c(V_{G1}) = A_{orifice} q T_T \int_{qV_{G1}}^{\infty} v_{\parallel} f(E_{\parallel})\, dv_{\parallel} \tag{2.1}$$

where $A_{orifice}$ is the total entrance slit area and V_{G1} is the sweeping potential at the grid 1. $v_{\parallel}$ and $f(E_{\parallel})$ are the parallel ion velocity and the parallel ion energy distribution respectively. T_T is the total transmission coefficient. The following discussion follows [21]. $f(E_{\parallel})$ will not reflect the actual distribution due to potential variation along the field line. Particles gain energy from the combined nature of the externally applied potential at the entrance slit, V_{en}, and the plasma potential, ϕ_p (Appendix.A.3). Here we assume the voltage at the grid 1 and the voltage at the grid 2 does not affect the energies of particles. Particles gain energy when they are coming to the electrodes, and they lose energy again when they are leaving. It is complicated to understand the complete physical phenomenon. For simplicity, the ion fluxes with high energy overcomes V_{G1}, and they are recorded by a collector. The collector current yields information on the ion parallel energy distribution and the plasma potential. From the exponential slope of $I - V$ characteristic curve, the ion temperature information and ϕ_p

information can be extracted.

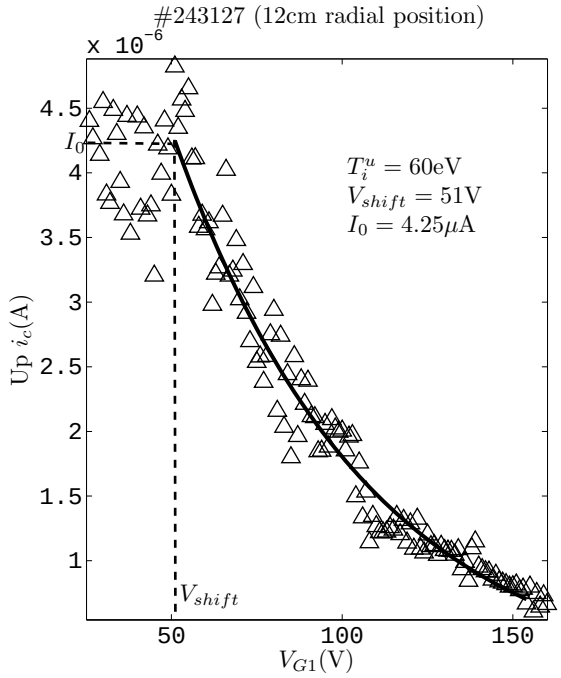

Figure 2.2: Typical RFEA $I-V$ characteristic curve. Collector current, i_c, is plotted against with the scanning voltage, V_{G1}.

For a Maxwellian distribution function of the analyzed ions, the current at the collector as a function of V_{G1} in a hydrogen plasma is given by

$$i_c = I_0, \qquad V_{G1} \leq V_{shift} \tag{2.2}$$

$$i_c = I_0 \exp\left[\frac{-(V_{G1}-V_{shift})}{T_i(\text{eV})}\right], \qquad V_{G1} > V_{shift} \tag{2.3}$$

where I_0 in A is the ion current collected when none of the ions is repelled by V_{G1}, i_c in A is the ion current collected by the collector plate, and T_i(eV) in eV is the ion temperature. Eq.2.3 can be rewritten as

$$\frac{T_i(\text{eV})}{Z} = \frac{V_{G1}-V_{shift}}{\ln\frac{i_c}{I_0}} = -\left(\frac{d\ln i_c}{dV_{G1}}\right)^{-1} \tag{2.4}$$

For the $I-V$ curve shown in Fig.2.2, the ion temperature on the upstream side is 60eV, I_0 is 4.25μA, and V_{shift} is 51V.

Kinetic theory (Emmert) predicts that V_{shift} is the potential equal to the difference between the plasma potential and the entrance slit potential, $V_{shift} = \phi_p - V_{en}$ [22]. Sheath voltage can be written as $\phi_{she} = \phi_p - \phi_f$ [21]. If $V_{en} = 0$, $V_{shift} = \phi_p$. ϕ_p can be determined by Langmuir probe [10] via $\phi_p = \phi_f - 3.33T_e(\text{eV})$.

2.3 DC Mode

In the standard ramping mode, the method is based on the $I - V$ characteristic curve resulting from the logarithmic slope of the analyzed ions. Current ratio at two points on the exponentially decaying region of the $I-V$ curve (standard ramping mode) with two different dc biases applied to the RFEA electrodes gives T_i in DC mode. The biasing configuration for the electrodes is shown in Fig.2.3. The following discussion follows [23].

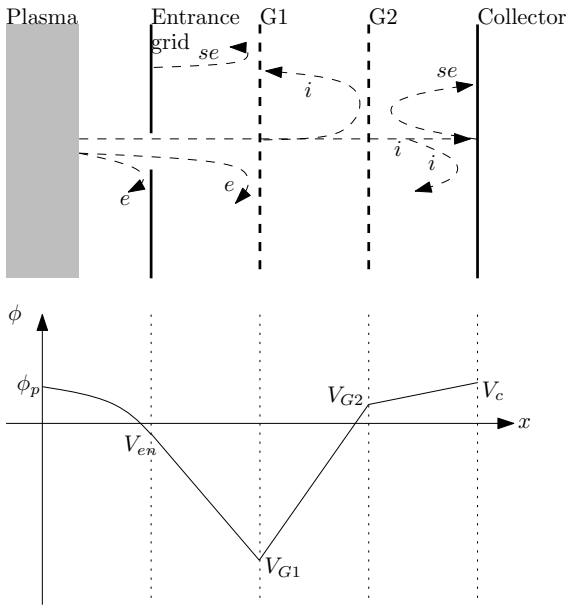

Figure 2.3: Main components of a RFEA and the biasing scheme applied for ion temperature measurement in DC mode.

The error in the ion temperature determination, $\delta T_i = \frac{\Delta T_i}{T_i}$, due to an error $\Delta I = i_{G2} - i_c$ can be estimated from Eq.2.5.

$$\delta T_i \approx \left(\frac{V_c - V_{G2}}{T_i(\text{eV})}\right)^{-1} \exp\left(\frac{V_{G2} - V_{shift}}{T_i(\text{eV})}\right)\left(1 + \exp\left(\frac{V_c - V_{G2}}{T_i(\text{eV})}\right)\right)\delta I \qquad (2.5)$$

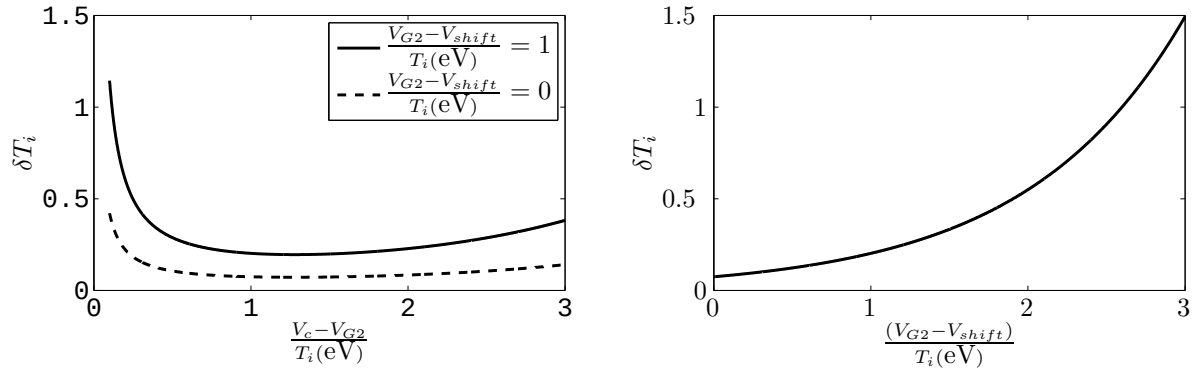

Figure 2.4: Left: dependence of δT_i on $\frac{V_c - V_{G2}}{T_i(\mathrm{eV})}$ for two values of $\frac{V_{G2}-V_{shift}}{T_i(\mathrm{eV})} = 0$ and 1. Right: dependence of δT_i on $\frac{(V_{G2}-V_{shift})}{T_i(\mathrm{eV})}$ while $\frac{V_c - V_{G2}}{T_i(\mathrm{eV})} = 1$.

If $\delta I = \frac{\Delta I}{I_0} = 2\%$, the analytical results are shown in Fig.2.4. From the plot, the limits of V_{G2}, externally applied voltage at the grid 2, and V_c, externally applied voltage at the collector, are determined. The T_i error is minimum in the range of $2 > \frac{V_c - V_{G2}}{T_i(\mathrm{eV})} > 0.5$ as shown on the left side of the figure. The condition, $0.3 > \frac{V_{G2}-V_{shift}}{T_i(\mathrm{eV})} > 0$, is applied for ion temperature estimation less than 10%. For $T_i = 35$eV on the upstream side (discharge average value measured by RFEA in the standard ramping mode), $V_c - V_{G2}$ should be between 17.5V and 70V from the first limit. From the existing data with the grounded entrance slit, the averaged value of the V_{shift} measured by the RFEA in the standard ramping mode is 38V. So the applied voltage of V_{G2} should be between 38V and 48.5V from the second limit. From the calculation, the average V_{G2} value is 43V, and the average V_c value is 87V. These values are reasonable because V_{G2} is in the region which is higher than V_{shift}, and V_c is around half of the maximum V_{G1} of the standard ramping mode. By following these limits, the estimated T_i value which is in the saturated current region or the flatter region of $I - V$ characteristic curve is avoided. Note: different V_{G2} and V_c should be applied on the different analyzers, upstream and downstream side.

The measured currents at the grid 2 and the collector should give the real-time T_i value by the following equation:

$$T_i(\text{eV}) = \frac{V_c - V_{G2}}{\ln\left[\frac{(\frac{i_{G2}}{i_c})|_{V_{G2}<V_c}}{(\frac{i_{G2}}{i_c})|_{V_{G2}=V_c}}\right]} \tag{2.6}$$

where i_{G2} is the current at the grid 1, i_c is the current at the collector, V_c is the applied voltage at the collector, and V_{G2} is the applied voltage at the grid 2. The ratio at the denominator of the equation is the ratio of currents at different potentials and at equipotential electrodes at the grid 2 and the collector.

In conclusion, even though the DC mode is rather simple (and it has some advantages compared to the traditional ramping mode regarding temporal resolution), V_{G2} and V_c are initially required. The limits of V_{G2} and V_c are limited by T_i and V_{shift}.

2.4 Entrance Slit

Entrance slit, grid 1, grid 2, and collector are the four electrodes of a RFEA. Among them, the entrance slit is the most important one to be carefully considered regarding to its hole size and material.

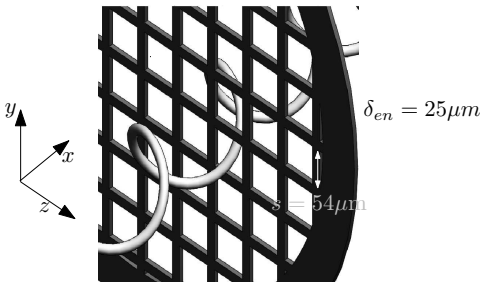

Figure 2.5: A trajectory of a particle in the entrance slit.

Choosing the proper thickness of the entrance slit is important for ion transmission as well as thermal properties for surviving in hostile environments. The entrance slit must be thin enough to permit adequate flux transmission. To keep away from the wall absorption, the entrance slit dimensions must satisfy the following condition:

$$\frac{v_{\parallel}}{v_{\perp}} \geq \frac{\delta_{en}}{s} \tag{2.7}$$

where $v_{\parallel}$ is the parallel ion velocity, $v_{\perp}$ is the perpendicular ion velocity, δ_{en} is the ratio of entrance slit thickness, and s is the entrance slit width. To have good transmission, a thin wall or large entrance slit is the best option. For particles with isotropic temperature and the entrance slit with 54µm hole, the thickness of the grid, δ_{en}, should be less than 38µm. For good signal to noise ratio, high ion current is preferable up to the Child-Langmuir current limit (Chap.2.6), $I_{max}^{C-L} < 110$µA. In DC mode, the positive ion current and the positive grid 2 current are strictly needed to estimate real-time T_i measurement (Chap.2.3).

In principle, the entrance slit width must be sufficiently small enough to assure the the plasma potential continuity across the entrance slit surface, $s < 2\lambda_{De}$ [24][21][25][12][26]. This design constraint assures that the charge particle distribution functions are not perturbed by an uneven distribution of the sheath potential. The entrance slit is also responsible for repelling electrons. λ_{De} in the STOR-M is 33µm. Entrance slit 1 with 54µm width and entrance slit 2 with 40µm width are suitable for STOR-M SOL region.

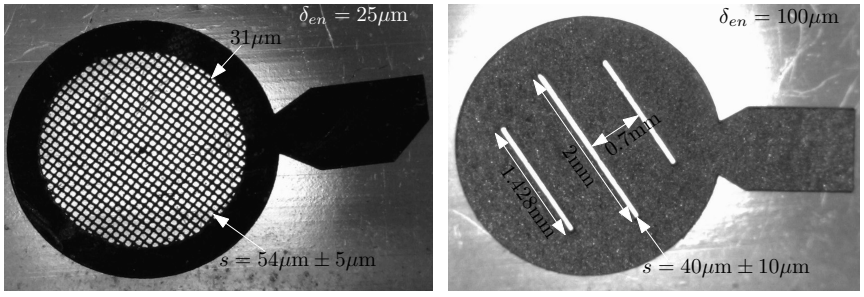

Figure 2.6: The entrance slits used in the bidirectional RFEA. The entrance slit on the left side, slit 1, was used in the 2010 T_i campaign. The entrance slit on the right, slit 2, was used in the 2011 T_i campaign.

Two slit designs are shown in Fig.2.6. A commercially available entrance grid (PYHD300-MO, Science Services GmbH, Goerzer Strasse 70 81549 Munich, Germany) is made out of molybdenum. Molybdenum was chosen because it survives in a very high temperature environment. During the 2010 T_i campaign, the entrance slit 1 on the downstream side (where drift velocity is caused by electrons) failed to survive. A more robust entrance slit was required for edge T_i measurement.

The slit 2 made out of tungsten is 4 times thicker than the molybdenum slit 1. Tungsten has a better melting point, 3695K, and better thermal conductivity, $173\text{W}\,\text{m}^{-1}\,\text{K}^{-1}$, than

the slit 1. The thicker slit design with the better thermal properties make the new slit much more robust than the old entrance slit 1. To achieve good ion transmission for thick entrance slit, tapered entrance slit surface design is suggested [21][12]. Only 3D laser micro machining can access the micro tapering surface.

2.5 The Perturbing Effects of a Large Probe in the Edge Plasma

By inserting a solid probe, the plasma is perturbed such that the parameters measured at the probe surface might be different from the unperturbed parameters in the absence of the probe. The degree of perturbation depends on the dimension of the inserted probe. Regarding the inserted solid probe, there is a corresponding ambipolar disturbance length, L_{col}^{amb}. L_{col}^{amb} is the parallel length required such that the parallel flux lost on the surface can be balanced by the perpendicular flux entering the collecting flux tube [21]. The flux tube is defined as the extending field lines when the solid material is inserted into the plasma. The probe is small enough for non-perturbation, if

$$L_{col}^{amb} < L_{\parallel} \tag{2.8}$$

where $L_{\parallel}$ is the connection length. If the Eq.2.8 is not satisfied, the probe acts effectively as a limiter [27]. The ambipolar connection length [22] is calculated by,

$$L_{col}^{amb} \approx \frac{c_s A}{16 D_{\perp}^{amb}} \tag{2.9}$$

where $c_s^2 = \frac{q(T_e(\mathrm{eV})+T_i(\mathrm{eV}))}{m_i}$ is the ion sound speed, A is the surface area perpendicular to the magnetic field, and $D_{\perp}^{amb} = \frac{T_i(\mathrm{eV})}{16B}$ [13][22] is the cross-field diffusion coefficient. For $T_i = 30\mathrm{eV}$, $T_e = 12\mathrm{eV}$, and $B = 0.75\mathrm{T}$, c_s is $63.43\mathrm{km\,s^{-1}}$ and $D_{\perp}^{amb}$ is approximately equal to $2.5\mathrm{m^2\,s^{-1}}$. Since the surface area, A, for the bidirectional RFEA in the STOR-M is $13.76\mathrm{mm} \times 21.76\mathrm{mm} = 0.0003\mathrm{m^2}$, by Eq.2.9, the ambipolar collection length for the RFEA is 0.47m.

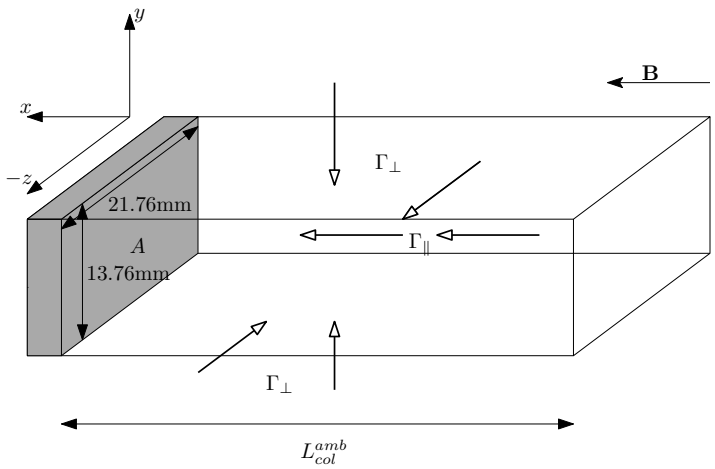

Figure 2.7: The figure shows the parallel flux, $\Gamma_{\parallel}$, lost on the solid surface with the perpendicular surface area, A, balanced by the incoming perpendicular flux, $\Gamma_{\perp}$, inside the collecting flux tube. Note: subscripts $\parallel$ and $\perp$ are the directions regarding to magnetic field, **B**, direction.

In the shadow of the poloidal limiter, the connection length, $L_{\parallel}$, which describes the parallel connection length along the flux tube to the solid surface, is limited to $\approx \frac{3}{2}\pi R_0$ for upstream direction and $\approx \frac{1}{2}\pi R_0$ for downstream direction as shown in Fig.2.8. The detail explanation of $L_{\parallel}$ is available in [27]. For $R_0 = 0.46$m, the connection length for the downstream side is 0.72m, and the connection length for the upstream side is 2.16m. Since $L_{\parallel}$ on both sides are larger than $L_{col}^{amb} = 0.47$m, the bidirectional RFEA probe used in STOR-M satisfies Eq.2.9. It is concluded that the RFEA fulfills basic design requirements, and T_i measurement on both sides by the current RFEA can be trusted.

2.6 Child-Langmuir Space Charge Limitation

Several effects such as ion transmission, entrance slit potential continuity, space charge limitation, and secondary electron emission have been considered as potential causes for abnormal behavior.

The maximum allowed incoming current due to space charge limitation, I_{max}^{C-L}, is determined by the potential difference between the electrodes and the electrode separation distance. This maximum current is limited by the Child-Langmuir current,

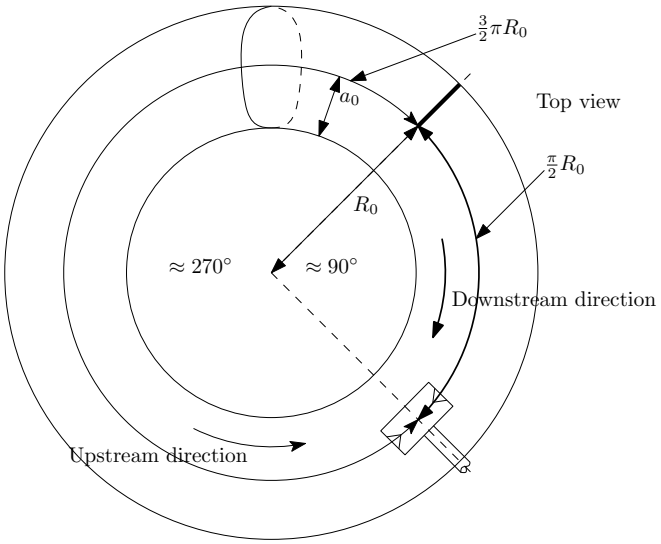

Figure 2.8: The location of the RFEA probe in the STOR-M Tokamak (top view).

$$I_{max}^{C-L} = 3.85 \times 10^{-8} \frac{(-V_{G2} + E_{\parallel})^{\frac{3}{2}}}{(x_{G2} - x_{\max(\phi)})^2} [1 + 0.0247 \sqrt{\frac{T_i}{-V_{G2} + E_{\parallel}}}] [\pi {r_{Li}}^2] \qquad (2.10)$$

where $I_{max}^{C-L} \equiv J_{max}^{C-L}[\pi r_{Li}^2]$ in A is the maximum limited current to avoid space charge effect, V_{G2} in V is the potential applied to the electron repelling grid, $E_{\parallel}$ in eV is ion parallel energy (Fig.2.9) that just overcomes the positive potential hill established by the ion space charge, $x_{G2} - x_{\max(\phi)}$ in cm is the distance between the grid 2 and the maximum potential due to the space charge, T_i in eV is the ion temperature, and πr_{Li}^2 in cm^2 is the area of ion Larmor radius in cm [12].

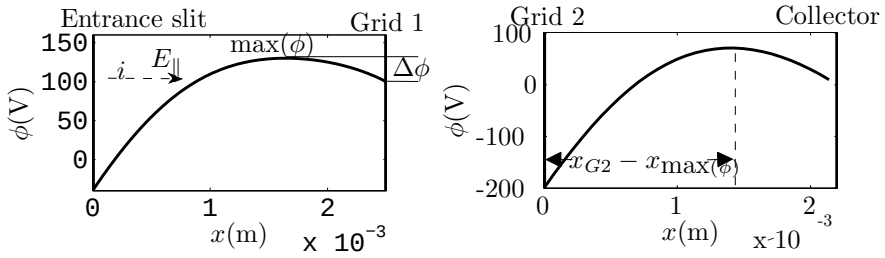

Figure 2.9: External applied voltage influenced by space charge effect (for illustration purpose only). Left: potential profile between the entrance slit and the grid 1. Right: potential profile between the grid 2 and the collector.

Since it is impossible to estimate $x_{G2} - x_{\max(\phi)}$, the distance between the grid 2 and the

collector were used for estimation (see the right side of Fig.2.9). For $E_{\|} = 50\text{eV}$, $V_{G2} = -220\text{V}$, $T_i = 30\text{eV}$, and $x_{G2} - x_{\max(\phi)} = 0.25\text{cm}$, Eq.2.10 yields $I_{max}^{C-L} \approx 110\mu\text{A}$. The space charge limited current can be increased either by reducing the distance between the grid 2 and the collector or by raising the external applied voltage between the two electrodes.

In the RFEA, grid 1 is used to reflect charged particles which have kinetic energy lower than the grid 1 potential. When incoming ion current overflows and high sufficient amount of ion particles trap, ion energy is determined by the maximum potential in the analyzer $\max(\phi)$ rather than the grid 1 bias as shown on the left side of Fig.2.9. Since ion temperature calculation is based on the result of $i_c - V_{G1}$ slope, $\Delta\phi$ can cause the contribution of inaccurate T_i estimation.

We can experimentally investigate the space charge problem by studying the pattern of the collected current as a function of sweeping V_{G1}. The following discussion follows [10]. If the space charge limit is violated, the collected current will exhibit a hysteresis pattern in $i_c - V_{G1}$ curve. While a physical mechanism like space charge could explain the hysteresis, in this case the hysteresis is more likely due to an electronics artifact. Since time appears as a parameter when plotting the $I - V$ curve, the passive filters (resistor, capacitor, etc...) used in the grid electronics can possibly be the reason for causing hysteresis pattern. The hysteresis could be reduced experimentally by sweeping the selector bias more slowly, but this reduces the number of characteristics that can be collected during plasma discharge. The choice of optimized frequency of V_{G1} in the STOR-M will be discussed in Chap.4.1.

Another feature of space charge effects is that a negative disruption current appeared at the collector. One possible contribution of this feature could be that the production of secondary electrons generated by the ion impacts on the electron repeller grid and the formation of localized discharge [12].

Chapter 3

STOR-M Tokamak

The Saskatchewan Torus-Modified (STOR-M) tokamak is the upgraded version of STOR-1M tokamak (major radius, $R_0 = 0.22$m, and minor radius, $a_0 = 0.035$m,) which was also built for turbulent heating, the application of a short, intense spike in the plasma current [28]. The STOR-M tokamak has been involved in numerous studies: Turbulent Heating [29], AC operation [30], electrode biasing [31], and Compact Torus (CT) Injection [32], etc. After the closure of tokamak de Varennes in 1997, STOR-M is the only device in Canada devoted to magnetic fusion. The parameters of the STOR-M tokamak are:

Major Radius, R_0	0.46m
Minor Radius, a_0	0.158m
Toroidal Magnetic Field, B_t	$0.5 \rightarrow 1$T
Plasma Current, I_p	50kA
Average Electron Density, n_e	$1 \sim 3\times\ 10^{19}\text{m}^{-3}$
Electron Temperature, T_e	$200 \sim 300$eV
Discharge Duration, t_d	50ms
Energy Confinement time, τ_E	1-3ms [8]

3.1 Vacuum and Gas Feed Systems

The vacuum chamber is constructed of two 4mm thick type-304L stainless steel elbows of circular cross section having an outer minor diameter of 324mm [33]. Each half of the chamber is connected at one end to a stainless steel elbow to reduce mechanical stress on the chamber.

The two halves of the chamber are separated by 20mm thick alumina to prevent current flow being induced in the wall of the discharge chamber by the primary ohmic heating coil of the tokamak transformer. The toroidal shape chamber has a major radius of 460mm and an inner minor radius of 158mm.

The chamber consists of ten horizontal, eleven vertical, and two tangential ports. These ports are intended for pumping, gas feed, and diagnostics [28]. A combination of a circular and rail limiter were installed in the STOR-M chamber. The limiter determines 12cm minor radius, and it allows for up to 1cm of horizontal displacement without additional scrape-off.

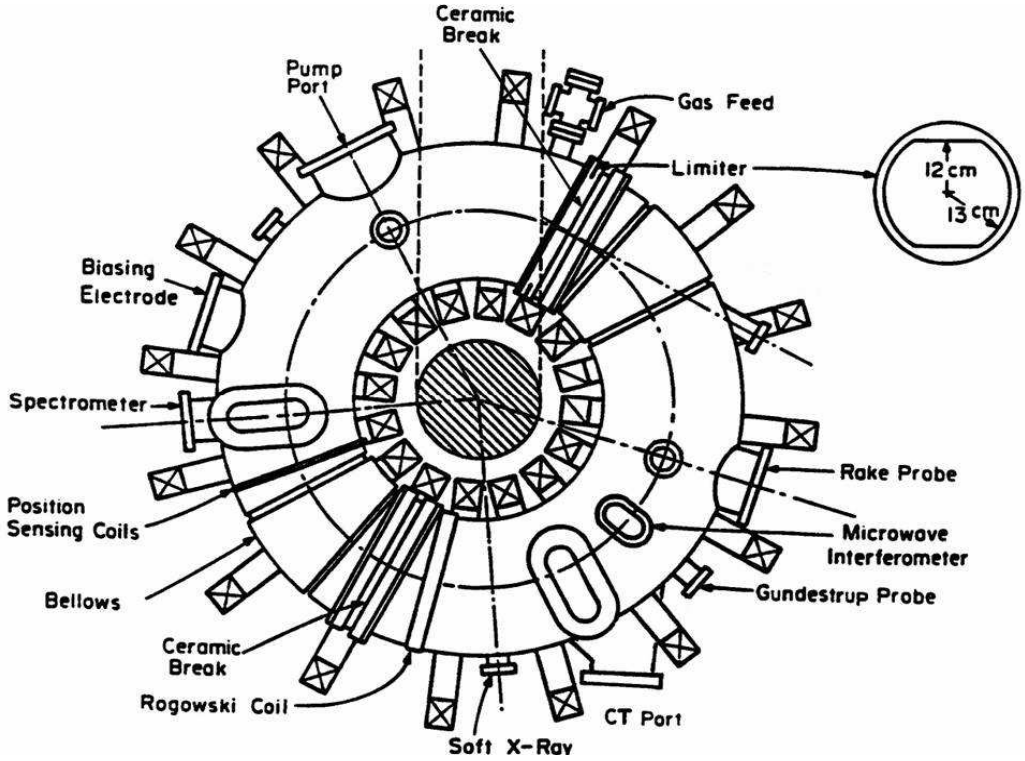

Figure 3.1: The schematic diagram of the top view of the STOR-M tokamak including diagnostic location, limiter, and chamber (not to scale).

The vacuum chamber is evacuated by a turbomolecular pump with a pumping speed of approximately 1000L s^{-1} supported by a rotary pump [34][35]. The tokamak chamber is pumped to 1×10^{-7}Torr (13.22µPa) and then filled with ultra high purity hydrogen (99.999%) to a pressure of 1.8×10^{-4}Torr (24mPa). Note: 1Torr is equal to 133.322Pa. Normally, the chamber pressure was held constant using a Veeco Automatic Pressure Controller [33][36]. Pressure had been controlled manually for 2011 experiment. The vacuum chamber is filled

through a PV-10 piezoelectric valve. The PV-10 has a response time of about 2ms. Two additional PV-10 equipped in the STOR-M, located approximately 180 toroidal degrees apart, are used with a preprogrammed open loop controller for the purpose of gas puffing during the discharge to control the plasma density. Two ionization gauges, one placed on the chamber and another installed on the pump inlet, monitor the gas pressure.

3.2 Toroidal and Poloidal Field Systems

The very strong toroidal magnetic field parallel to the current is used to suppress the main magnetohydrodynamic instabilities. The toroidal field intensity, B_ϕ, is greater than the poloidal magnetic field intensity, B_θ, produced by the current. The toroidal magnetic field system consists of 16 uniformly circular coils spaced evenly in the toroidal direction, each having nine turns of cross section, 70mm $\times$ 6.4mm copper for a total number of turns of wire, N=144. The windings are concentric, and mylar is inserted for insulation. Each coil is housed in a stainless steel case. A 1.3cm thick belt is used to compress the coils against the torsional forces that act on the coil during discharges as shown in Fig.3.2.

The coils are connected in series with a total equivalent circuit of a resistor of 13.5mΩ at room temperature in series with a total inductance of 2.06mH. The toroidal field at the center of the chamber is

$$B_\phi = \frac{\mu_0 N I_t}{2\pi R_0} = 6.261 \times 10^{-5} I_t \tag{3.1}$$

where I_t in A is the current in the toroidal magnet, N is the number of turns of wire, and R_0 in m is the major radius of the chamber. Since the maximum current is about 12kA, the peak toroidal field at the center of the discharge chamber, B_ϕ, is 0.75T [28].

3.3 Confinement Time

The energy confinement time, τ_E, of a plasma is a measurement of the rate of energy loss of a system to its environment without input. It is often misunderstood with the discharge

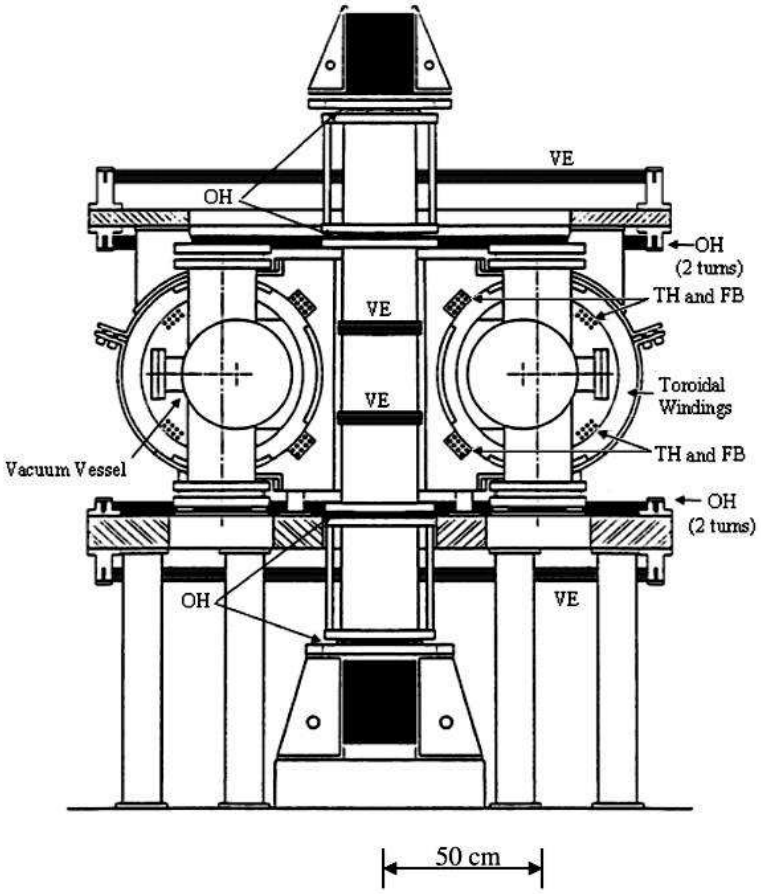

Figure 3.2: A vertical cross section of STOR-M tokamak by indicating the locations of the Vertical Equilibrium (VE) windings, the ohmic heating (OH) coils, the Turbulent Heating (TH), Feedback (FB) winding, and Vacuum Vessel.

duration [3]. The rate of energy loss in an ohmically heated plasma can be described by the following equation:

$$\tau_E = \frac{E_t}{P_{loss}} \tag{3.2}$$

where τ_E is the energy confinement time, E_t is the thermal energy, and P_{loss} is the rate of energy loss. The particles in the plasma with temperature, T, have an average energy of $\frac{3}{2}kT$. Assuming the case of $n_e \approx n_i$ and $T_e \approx T_i$, and applying the geometrical approximation of Fig.3.3, the total thermal energy of a system is $3nkT \times 2\pi^2 a_0^2 R_0$. The rate of energy loss measured by P_{loss} is the product of loop voltage, V_l, and plasma current, I_p. Remember $T(\text{eV}) = \frac{kT(\text{K})}{e}$. So τ_E can be determined from the experimental measurements [33]:

$$\tau_E = \frac{6nqT(\mathrm{eV})\pi^2 a_0^2 R_0}{V_l I_p} \tag{3.3}$$

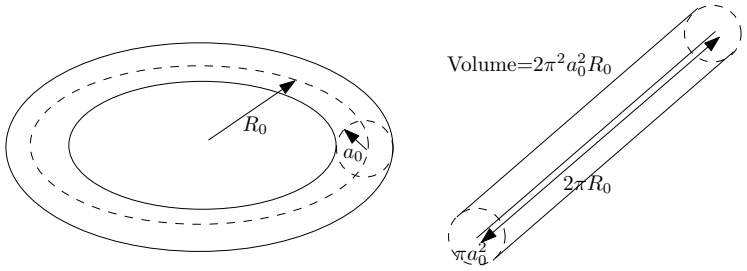

Figure 3.3: Geometric approximation of a torus from a cylinder.

For a typical ohmic heating ($I_p \approx 20\mathrm{kA}, V_l \approx 3\mathrm{V}, T \approx 190\mathrm{eV}$, and $n \approx 5\times10^{18}\mathrm{m}^{-3}$) of the STOR-M tokamak with $R_0 = 0.46\mathrm{m}$ and $a_0 = 0.158\mathrm{m}$, the confinement time, τ_E, is 1.7ms.

3.4 Langmuir Probe

This section is intended to serve as a helpful reminder of the technical details in analyzing data collected by applying a sweeping power to the probe, but it is not a complete theoretical effort. The experimental data is not on hand. So with the help of schematic diagram, the estimations of plasma density, temperature, and potential are discussed. A schematic of experimental setup of Langmuir probe in the chamber with the adjustable potential, V_{bias}, is shown in Fig.3.4.

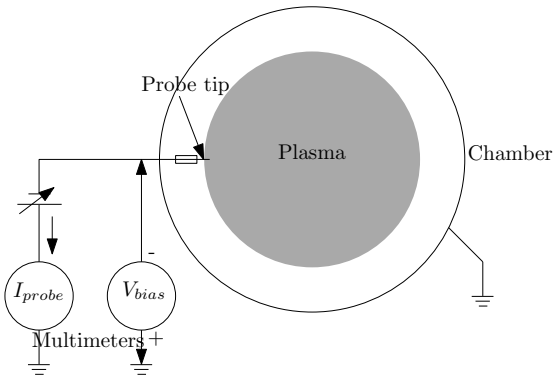

Figure 3.4: Schematic diagram of a Langmuir probe installed in a chamber.

The $I-V$ characteristic shown in Fig.3.5 can be divided into three regions:

- for $V_{bias} < \phi_f$(floating potential), the probe current is mainly positive ion current.
- for $\phi_f < V_{bias} < \phi_p$(plasma potential), the current is mostly due to electron diffusion to the probe. Note that when the applied voltage, V_{bias}, is as the same potential at plasma potential, electrons and ions diffuse to the probe as if they were unaffected by its presence.
- for $V_{bias} > \phi_p$, the current is space charge limited electron current.

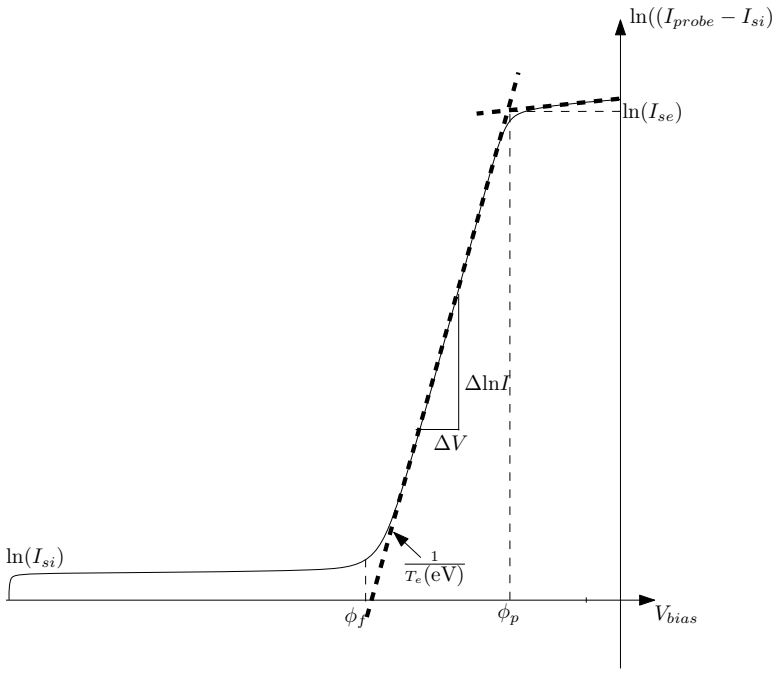

Figure 3.5: Flowing current to the probe, $\ln(I_{probe} - I_{si})$, versus applied potential at the probe, V_{bias}. Specific areas of interest are labeled. I_{se} is the electron saturated current.

Referring to Fig.3.5, the ion saturation current, I_{si}, is seen at biases well below ϕ_f. At ϕ_f, the electron current equalizes the ion current, and the net current to the probe is zero, $I_{probe} = 0$. When V_{bias} is increased enough, the current stops increasing. In that region, the space charge is limited, or electron current is saturated. The applied potential where this knee point occurs is the plasma potential, ϕ_p.

The relationship between the measurement and plasma parameters is given by,

$$\ln |I_{probe} - I_{si}| = \frac{1}{T_e(\text{eV})}(V_{bias} - \phi_f) + \text{constant} \tag{3.4}$$

Note that the above equation is in the form of a linear equation, $y = mx + c$, where slope, m, is analogous to $\frac{1}{T_e(\text{eV})}$ and y-intercept at $x = 0$ is analogous to constant. Linear fit to the curve gives the inverse electron temperature as shown in Fig.3.5. It is important to choose a bias range over which to perform this fit. Since I_{probe}, I_{si}, V_{bias}, ϕ_f, and constant can be determined from $\ln(I_{probe} - I_{si})$ vs V_{bias} curve, T_e can be calculated.

The electron density can be calculated from the known T_e and I_{si}:

$$n_e = \frac{I_{si}}{q^{\frac{3}{2}} A_s \exp(-\frac{1}{2})} \sqrt{\frac{m_i}{T_e(\text{eV})}} \tag{3.5}$$

where m_i is the ion mass and A_s is the area of the probe sheath. Generally the probe sheath is approximated as the probe tip area. If the electron Debye length, λ_{De}, is significant compared to the probe tip area, this is not a good approximation, and the area should be corrected. The detail explanations are widely discussed in [37].

3.5 Katsumata tunnel Probe

The CASTOR tokamak group used the Katsumata tunnel probe for ion temperature measurements. The Katsumata probe consists of a hollow conducting tunnel (whose radius is larger than ion gyroradius [18]) that is closed at one end by an electrically isolated conducting backplate. An electrically isolated diaphragm is mounted on the other end. The tunnel electrode is segmented axially into two equally long parts. All electrodes (diaphragm, both segments, and back plate) can be biased separately. Here we assume the axis of the tunnel probe is parallel to the magnetic field. Due to the diaphragm, which protrudes from the tunnel around the entire circumference, the electrons should in principle not be able to reach the tunnel segments because their gyroradii are very small (see Fig.3.6).

During the measurements, the sweeping voltages are applied simultaneously across the diaphragm and the two tunnel segments. The resulting three characteristics are recorded separately. The diaphragm acts as a single Langmuir probe. Ion saturation currents at the two tunnel segments, $I_{i,1}$ and I_{i_1}, can be determined at the externally applied voltages much below the plasma potential. The ratio of ion currents at the two segmented tunnel electrodes, $\frac{I_{i,2}}{I_{i,1}}$, has been taken as a measure for $T_{i\|}$. However, the precise relation between this current

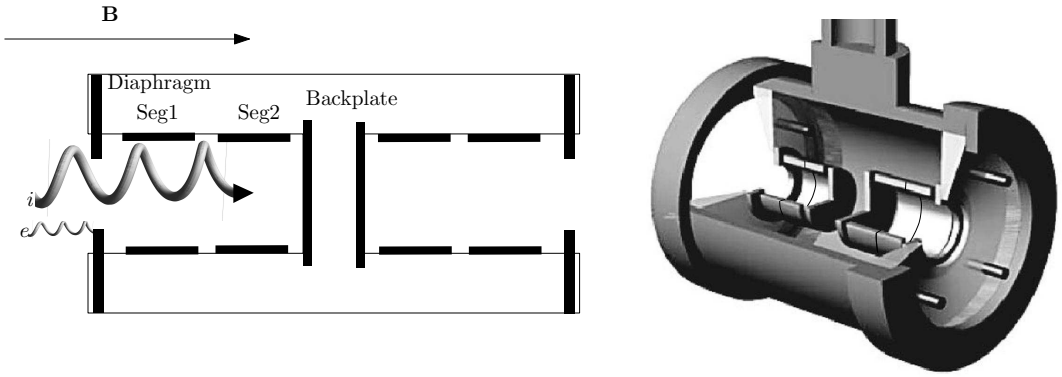

Figure 3.6: Left: scheme of the bidirectional ion-sensitive segmented Katsumata tunnel probe. Right: 3D design of the probe (image courtesy of [18]).

ratio and $T_{i\|}$ has to be determined by means of XOOPIC simulation [38] of this probe. Note: ions with a large parallel velocity component are able to reach the second segment, whereas those ions with a small parallel velocity (having on the other hand a large perpendicular velocity component) will mainly be attracted by the first segment. The above discussion follows [18].

Chapter 4

Experimental Results

In STOR-M, the discharge starts with an initial breakdown during which pre-ionization happens. This process is performed by the hot filament and the RF field. The purpose of this stage is to produce seed electrons. The collisions with neutral hydrogen produce more electrons. The next stage, current ramp up phase, lasts up to 10ms. This stage is powered by a fast ohmic capacitor bank. After 10ms, the slow ohmic capacitor bank maintains the quasisteady current state (plateu) for up to about 30ms. The discharge is terminated by a strong gas puff in order to prevent runaway electrons production [8].

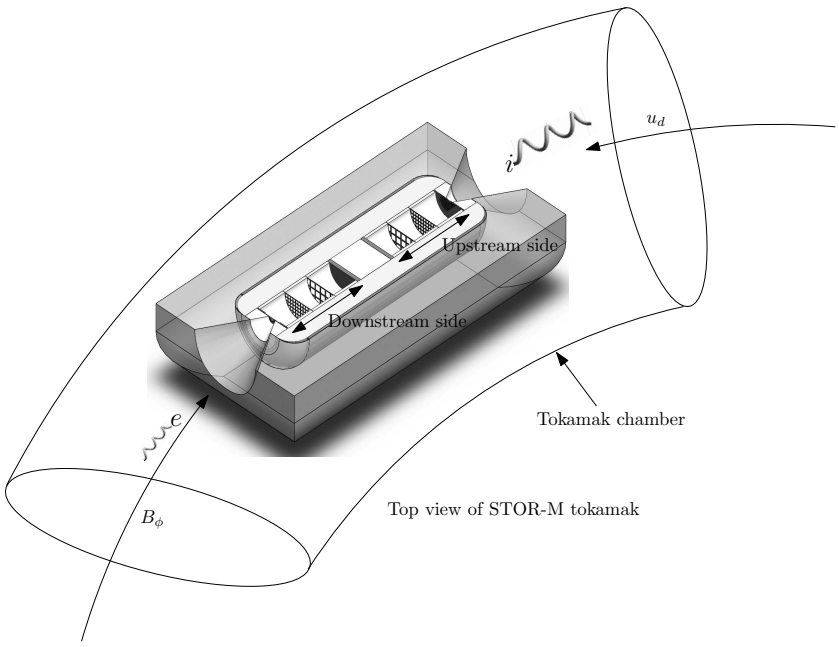

Figure 4.1: Schematic of cross-section view of the RFEA in the STOR-M tokamak chamber. The identical analyzers are mounted back to back.

The main purpose of the RFEA was to obtain ion temperature in the SOL region. The previous RFEA built by Damian Rohraff used in the STOR-M tokamak have only one sided

analyzer. In the earlier T_i measurement campaign, T_i were measured on the upstream side, and T_i values were corrected by Mach number measured by the Gundestrup probe to account for the plasma flow [14][22][8]. To access the direct averaging method in T_i measurement, RFEA with bidirectional energy analyzers is needed to measure T_i both on the downstream, d, side and on the upstream, u, side. A simple inexpensive bidirectional RFEA was built, and it was used for T_i measurement in both directions. A 3-dimensional schematic of bidirectional RFEA in the tokamak chamber is shown in Fig.4.1.

Referring to Fig.4.1, one analyzer measures the ion temperature on the downstream side, T_i^d, while the other one measure the ion temperature on the upstream side, T_i^u. The Maxwellian distribution function is shifted up on the upstream side while the function on the downstream side is shifted down because of ion drift velocity, u_d. Those shifted up and shifted down Maxwellian distribution function contribute to increasing and decreasing of T_i value respectively, $T_i^u > T_i^d$ [14]. The average ion temperature, T_i, is equal to $\frac{T_i^d + T_i^u}{2}$ [14][11].

4.1 Data Analyzing Method for Standard Mode

Ion temperature is estimated from $I-V$ slope (Chap.2.2). Proper data analysis is necessary to provide accurate T_i. Any changes of the slope of exponential fit to i_c while analyzing the data will provide inaccurate information about T_i.

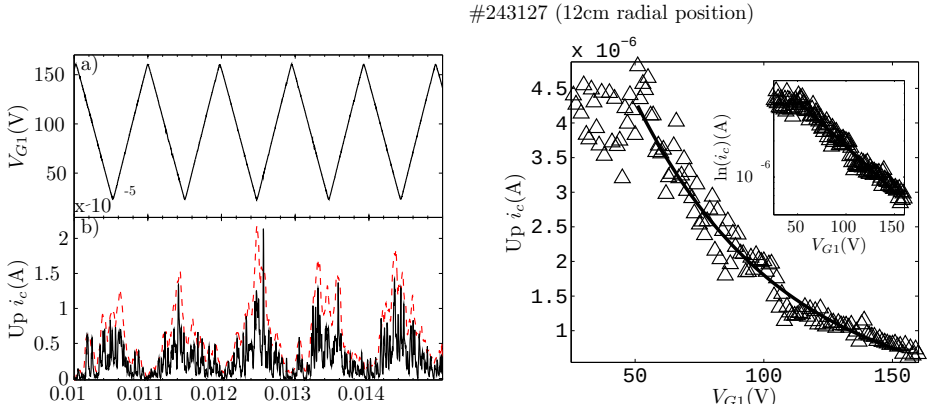

Figure 4.2: Left: (a) applied voltage at the the grid 1, V_{G1}, and (b) the collected upstream current (black solid), up i_c, and the smoothed i_c over 70µs rescaled (×3) (red) [39]. Right: the reconstructed i_c-V_{G1} characteristic curve.

In principle, T_i can be estimated by differentiating the ion current in regard to the scanning bias V_{G1}. In experiment, a fit to the $i_c - V_{G1}$ characteristic could provide the T_i value [40]. A specific time window was needed for averaging the slopes.

Referring to Fig.4.2, i_c between 10ms and 15ms had been averaged for reconstructed $I-V$ characteristic curve. The reconstructed $I-V$ curve is shown on the right side of Fig.4.2. An inset figure is the semi-log plot of $I-V$ characteristic curve. From the figure, knee point of $I-V$ curve, V_{shift}, is 51V, and T_i^u is 60eV. The plasma potential, ϕ_p, is $\approx$ 14V and it had been determined from V_{shift}. Note: $V_{shift} = V_p - V_{en}$. The externally applied voltage at the entrance slit was -37V. The plasma potential determined by the previous RFEA was also around $10-15$V [8]. The Matlab code for reconstruction of $I-V$ curve is given in Appendix.B.

4.2 Experimental Setup and the Reliability of SOL T_i Measurement

It is important to suppress noise while collecting i_c. An additional dummy wire parallel to the wire connected to the RFEA collector was used for the output system of the collector as shown in Fig.4.3. Similar technique was used in the previous ion temperature campaign of the STOR-M [8]. In the design, an instrumentation amplifier was used as an differential amplifier. If the collector picks up electromagnetic noise, a similar noise level appears on the dummy wire. Thus common noise appears on both cables. A differential amplifier suppresses the common noise picked up by the two inputs by the following equation:

$$V_{out} = A_d(V_{Col}^{+} - V_{CMR}^{-}) \tag{4.1}$$

where V_{Col}^{+} and V_{CMR}^{-} are the input voltages, and A_d is the differential gain. In theory, if the input voltages, V_{Col}^{+} and V_{CMR}^{-} are equal, the output will be zero. We used equal lengths of RG58 50Ω coaxial cables (from a single roll) both for the collector and for the dummy cable outside the chamber to have the same wire impedance [41]. 0.81mm mini coaxial cables were used inside the chamber. In the figure, the resistors, R, serve as the current to voltage

convertors.

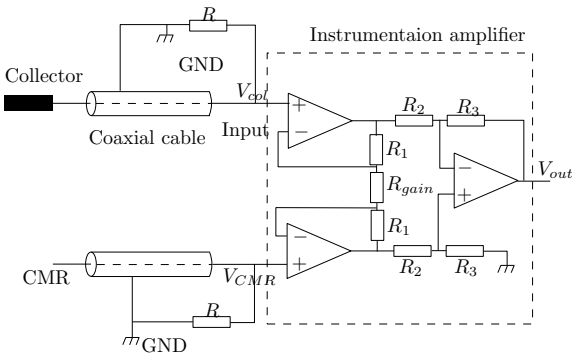

Figure 4.3: The electronic system of the collector plate connected to the differential amplifier.

Hysteresis pattern of i_c can be caused by either space charge effect or electronic artifact (see Chap.2.6). Collector current should avoid the hysteresis pattern while collecting i_c in normal operation (or while the location of the RFEA is close to the chamber wall). $I-V$ characteristic curves with different scanning frequencies are compared in Fig.4.4. When the scanning frequency is high enough, the hysteresis pattern occurs as shown on the left side of the figure. At 1kHz scanning frequency, the hysteresis pattern disappears. From the plots, the maximum scanning frequency of V_{G1} should be 1kHz. If the scanning frequency is decreased, the number of characteristics that can be collected during plasma discharge decreases. Here we chose 1kHz for scanning frequency.

If a plasma discharge duration is 40ms, and scanning frequency is 1kHz, 80 slopes are obtained approximately in a single shot. The maximum time resolution of T_i estimation available by the RFEA here is $\frac{1}{2\times\text{scanning frequency}} = 0.5\text{ms}$.

The RFEA was operating in both electron temperature measurement mode, e mode, and ion temperature measurement mode, ion mode. The applied voltage at the entrance slit was -37V for ion mode and +37V for e mode. -220V DC voltage was applied to the grid 2 for ion mode, and +220V for e mode. The collector was maintained at 0V.

We performed T_i campaigns twice. The first experiment was performed in mid 2010, and the other was performed at the end of 2011. In the first T_i campaign, the bipolar sweeping power supply ($-100\text{V} \longleftrightarrow +100\text{V}$) was applied at the grid 1 for data collection, and the entrance slit made out of molybdenum, the entrance slit 1 (Chap.2.4), was used in the first

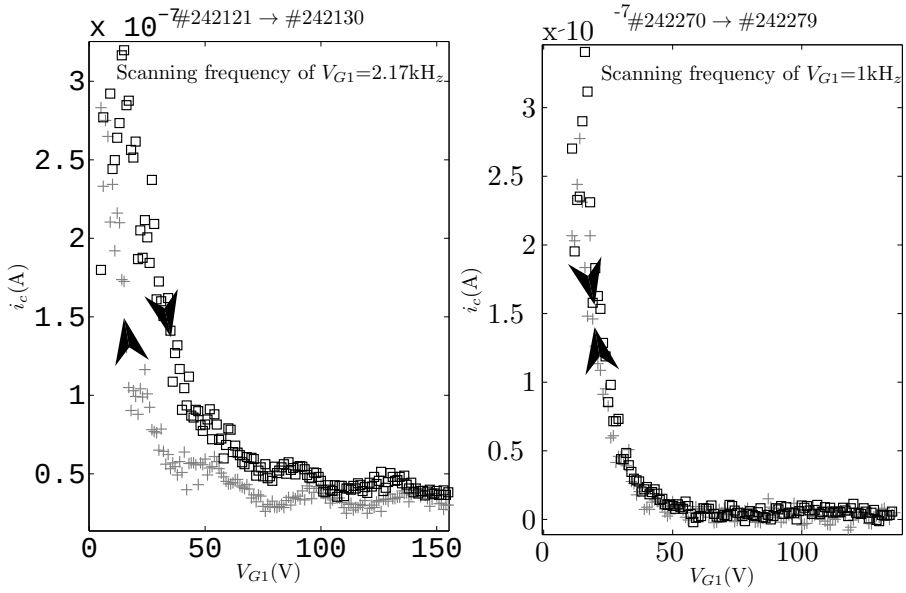

Figure 4.4: Left: $i_c - V_{G1}$ characteristic curve with 2.17kHz scanning frequency at the radial position of 15.5cm (measured from the plasma core). Right: $i_c - V_{G1}$ characteristic curve with 1kHz scanning frequency at 15.5cm.

campaign. For the second T_i campaign, the unipolar sweeping power supply (0V $\longleftrightarrow$ +160V) was applied at the grid 1 for ion mode. The entrance slit made out of tungsten, the entrance slit 2 (Chap.2.4), was used in the T_i measurement campaign. Upstream i_c and downstream i_c with some plasma parameters are shown in Fig.4.5. From the figure, the plasma current, I_p was about 20kA, and the loop voltage, V_l, was about 3V.

The entrance slit 1 was replaced with the entrance slit 2 because the slit 1 on the electron side was burned during the first T_i campaign (see Chap.2.4). The maximum sweeping voltage (+100V) at the grid 1, V_{G1}, in the first T campaign was not enough for the upstream side T_i measurement. The unipolar sweeping power supply had been used in the second experiment because there is no op-amp whose operating voltage is higher than 100V. Several interesting tests (such as entrance slit potential continuity, secondary electron emission test, etc.) can be made on analyzers by using bipolar sweeping power supply at the grid 1 [10].

The entrance slit must be wide enough to permit adequate flux transmission. On the other hand, disturbance of particle trajectories can be omitted by choosing an entrance slit aperture whose width is less than 2 Debye length in theory [12][13][14]. Since λ_{De} in the SOL region of the STOR-M is 33µm, entrance slit 1 with 54µm width and entrance slit 2

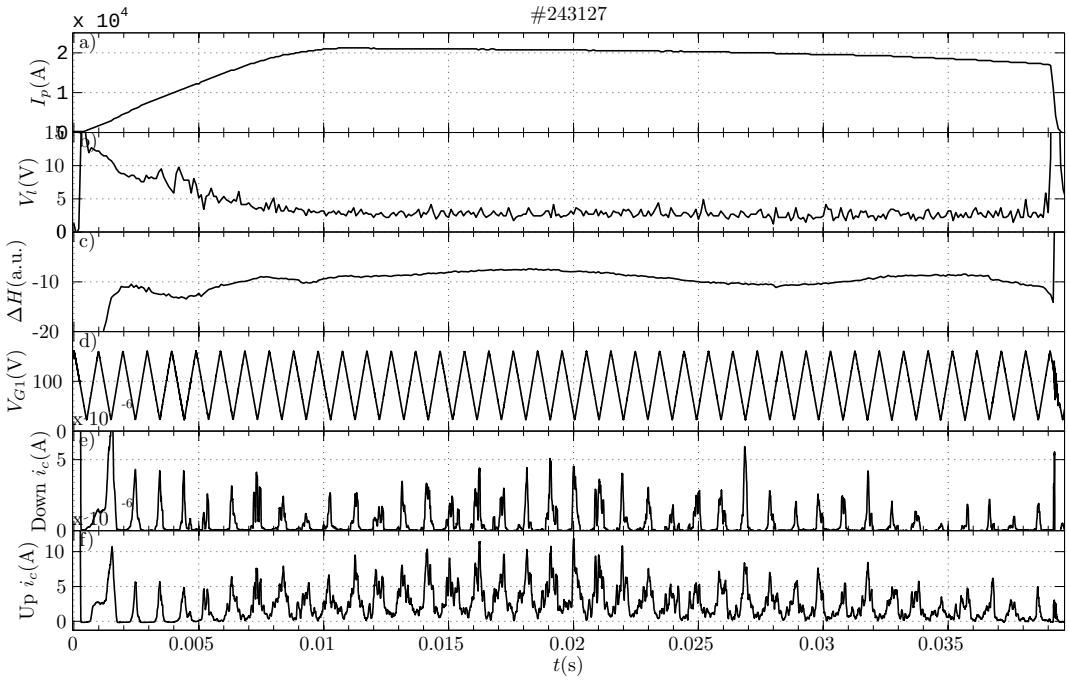

Figure 4.5: Plasma current, I_p, plasma loop voltage, V_l, plasma position, ΔH, the applied voltage at the grid 1, V_{G1}, the downstream current, down i_c, and the upstream current, up i_c, at the radial position of 15.5cm in ion mode. The data are from the second T_i campaign. The shot number is 243127.

with 40µm width satisfy the criterion to avoid perturbation by an uneven distribution of the sheath potential.

In [11], T_i were measured experimentally with different $V_{G2} = -10, -150, -250,$, and -550V. Despite the variation of V_{G2}, T_i is constant within the error bars. In other words, the T_i estimation cannot be perturbed by the external applied voltage at the grid 2. Such measurements have not been available in the STOR-M tokamak yet.

4.3 Evaluation of the SOL Temperature in the STOR-M Tokamak

Referring to Fig.4.6, T_i and T_e were measured by the bidirectional RFEA with the slit 2. r_c is the minor radius. Horizontal limiter is at 13cm, and vertical limiter is located at 12cm. The center of the minor radius of the chamber is at 0cm, and the wall is at 15.8cm.

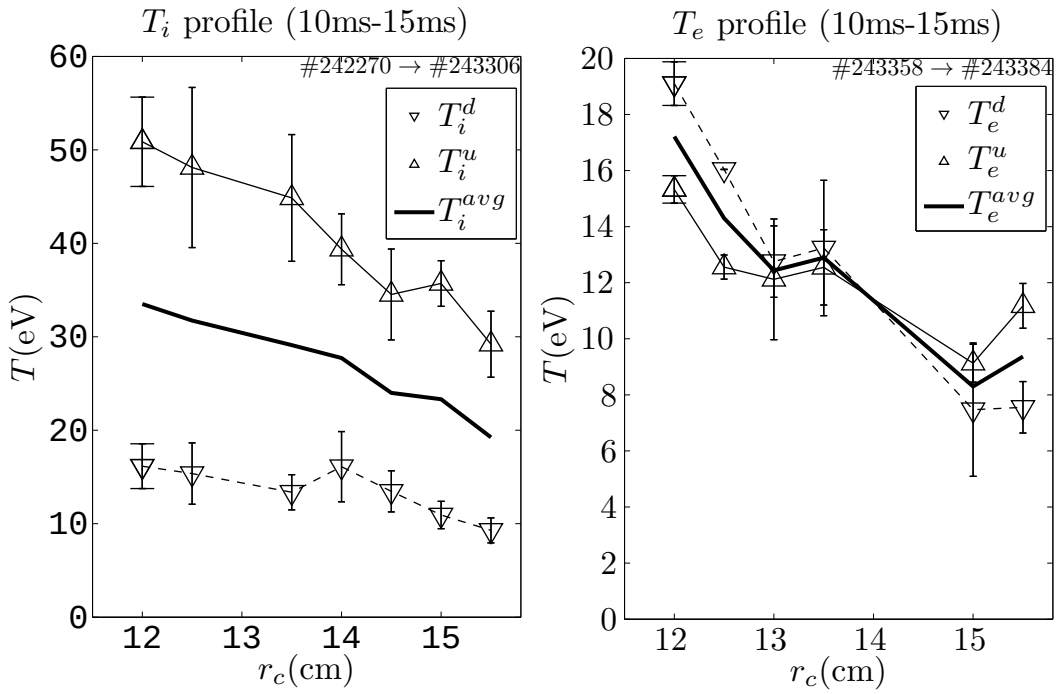

Figure 4.6: Left: T_i versus r_c. Right: T_e versus r_c.

Collector currents between 10ms and 15ms which is the I_p plateau region had been averaged for T_i and T_e profiles. By applying the averaging method as discussed in Chap.4.1, T_i and T_e had been estimated. Downstream T_i, T_i^d, downstream T_e, T_e^d, upstream T_i, T_i^u, and upstream T_e, T_e^u, are shown in the figure. The averaged T_i and T_e are shown in thick solid lines. Several data were collected at each radial position. Each value was estimated from the reconstructed slope of the time window between 10ms and 15ms of each shot. Temperatures regarding to each radial position had been treated statistically by finding mean value and standard deviation value. The estimated T_i measured by the bidirectional RFEA is between $\approx$ 19eV and $\approx$ 34eV in the SOL region. The previous T_i measured by one sided energy analyzer in the SOL region of the STOR-M corrected by Mach number is between $\approx$ 14eV and $\approx$ 29eV [22]. T_i measured in the TORE SUPRA [11] is between $\approx$ 5eV at 80mm and 50eV at 0mm from the last closed flux surface, LCFS. T_i of the ISTTOK [13] in low density plasma, $\langle n_e \rangle = 2 \times 10^{18} \mathrm{m}^{-3}$, is between 7eV at 2cm and 16eV at 0.4cm from the poloidal limiter. T_i increases radially in an inward direction. T_i^u is larger than T_i^d due to drift velocity. $\frac{T_i}{T_e}$ measured by the bidirectional RFEA in the SOL region of the STOR-M tokamak is between 1.8 and 2.8 as shown in Fig.4.7. The ratio increases with minor radius.

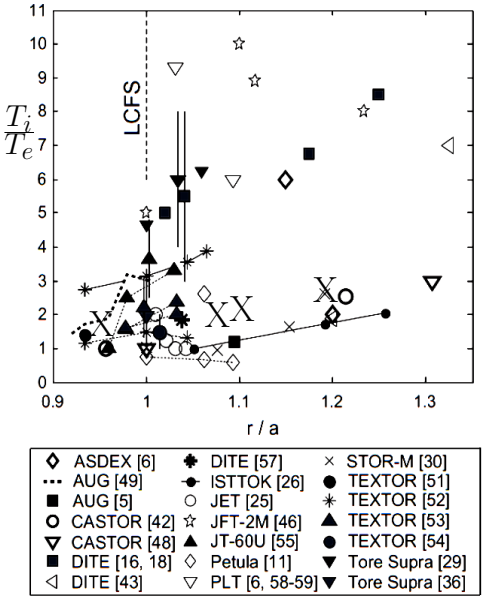

Figure 4.7: $\frac{T_i}{T_e}$ values over 30 years in several tokamaks (image courtesy of [19]). 'X' represent the most recent $\frac{T_i}{T_e}$ values measured by the bidirectional RFEA of the STOR-M tokamak.

From the radial profile of ion temperature, the ion pressure gradient can be obtained. The Rake probe measures floating potential and should provide E_r via the formula $E_r = -\nabla\phi_f - 3T_e$ [42]. But during our T_i measurement campaign, the Rake probe created shadow effect because the locations of the RFEA and the Rake probe were very close, and the current on the downstream side completely disappeared. The Rake probe had to be pulled out during RFEA operation. Without the E_r, the radial force balance equation Chap.1.5 cannot be verified.

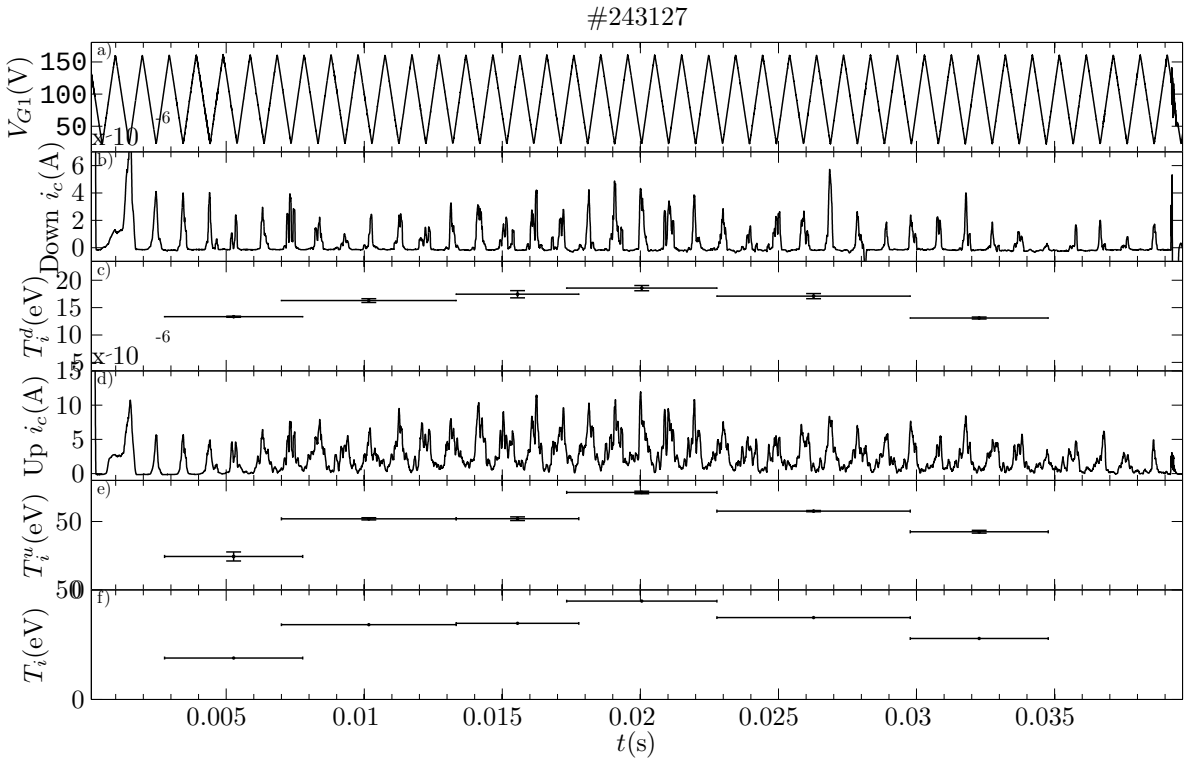

Figure 4.8: (a) Scanning voltage applied at the grid 1 (the applied voltage at the grid 2 is negative for T_i measurement mode), (b) downstream ion current, (c) downstream ion temperature, T_i^d, (d) upstream ion current, (e) upstream ion temperature, T_i^u, and (f) average T_i.

Referring to Fig.4.8, T_i^d, T_i^u, and average T_i are plotted as a function of time at the radial position of $r_c = 12$cm. The rise of T_i can be clearly seen at the beginning of the discharge, during plasma current ramp up. It decreases after 20ms. The maximum T_i is 45eV at 20ms. The averaged time window is shown by the line width.

By reversing the polarity of the grids, RFEA can be operated in e mode. The results

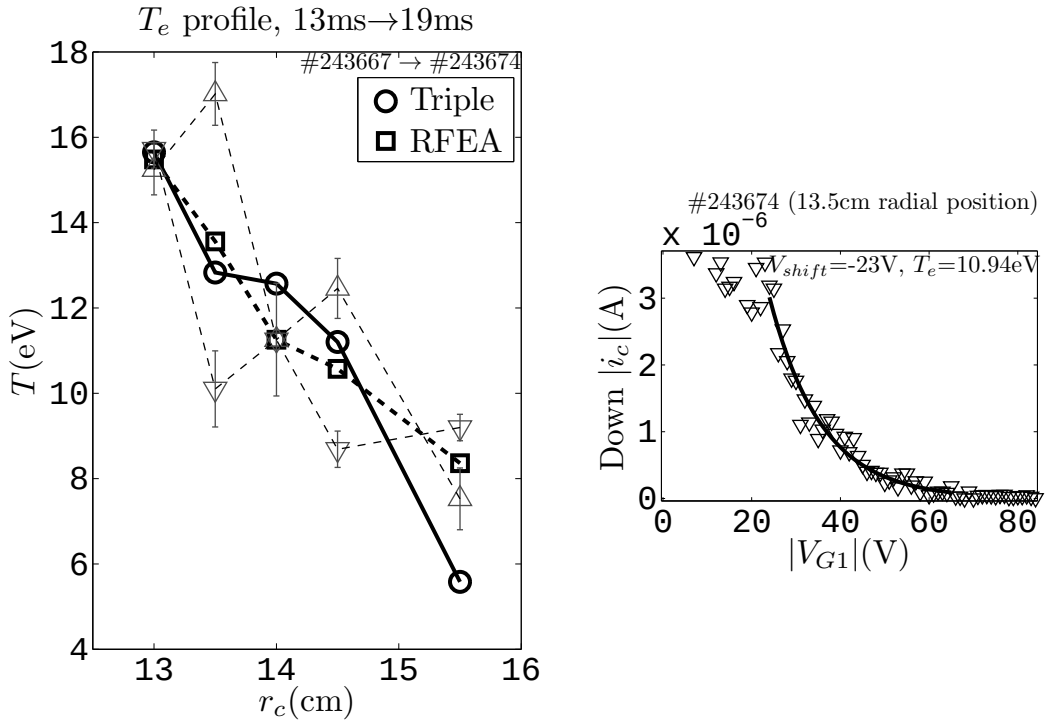

Figure 4.9: Left: electron temperatures measured by the RFEA and the Triple probe in the SOL. Right: $I-V$ characteristic curve of shot number 243674.

are compared with the results from the Triple probe. Simultaneous measurements of T_e by the two different instruments, the RFEA and the Triple probe, were performed between shot #243667 and #243674. The RFEA and the Triple probe were located almost 0.94m (quarter of the major radius) apart in the STOR-M tokamak. Referring to the left side of Fig.4.9, the averaged time window of T_e was between 13ms and 19ms. The sweeping V_{G1} was between 0V and -90V. In the e mode, i_c disappears if the absolute value of the retarding voltage is significantly lower than that in the ion mode. The electron temperature was expected to be lower than the ion temperature. As in the ion mode, RFEA measured T_e both on the downstream side and on the upstream side, and average T_e is equal to $\frac{T_e^d+T_e^u}{2}$. The T_e measured by the RFEA by reversing the externally applied voltages at the electrodes was juxtaposed by T_e measured by the Triple probe at each radial position on the left side of Fig.4.9. T_e gradient measured by the RFEA is less steep than T_e measured by the Triple probe. Downstream electron temperatures, T_e^d, and upstream electron temperature, T_e^u, marked by $\bigtriangledown$ and $\bigtriangleup$ with standard deviation values are shown on the left side of the figure.

The curve shown on the right side of Fig.4.9 is the $I-V$ characteristic collected by the

RFEA from which T_e^d was calculated. The estimated T_e^d from the exponentially fitted curve is 10.94eV, and V_{shift} is -23V at the radial position of 13.5cm.

4.4 T_i Measurement with Reverse I_p

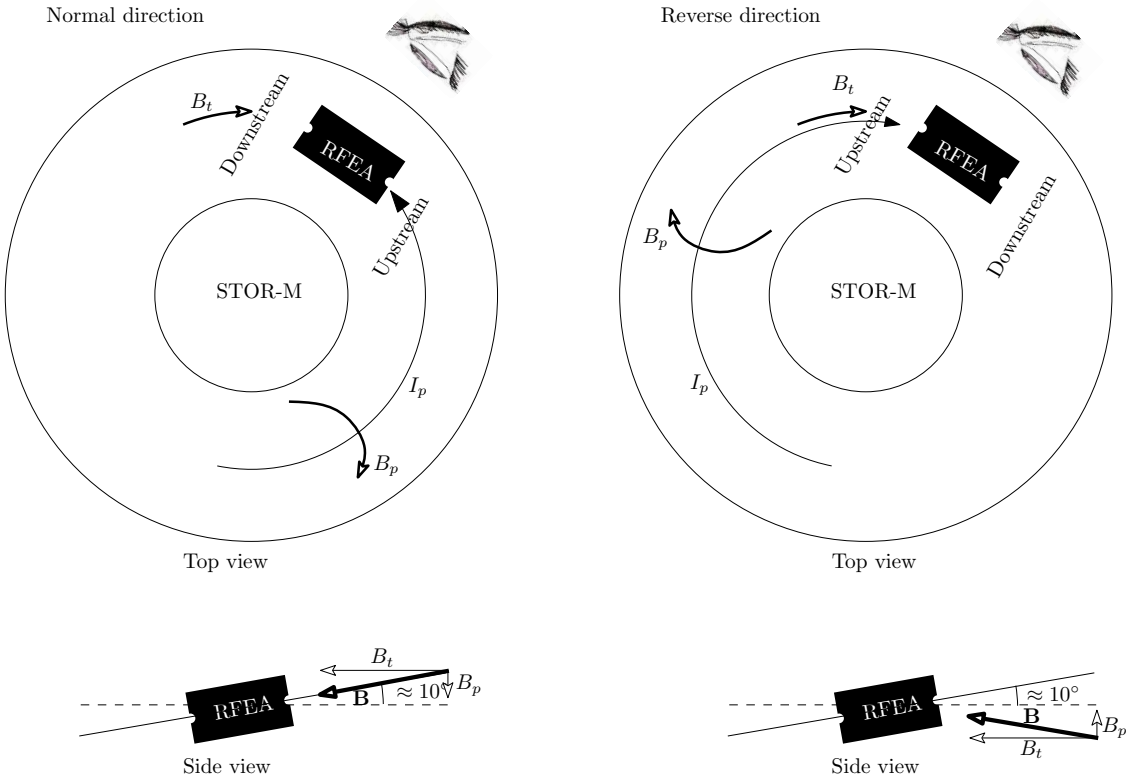

Figure 4.10: Left: the notations of the downstream and the upstream direction when the plasma current, I_p, is in the counterclockwise direction. Side view shows the orientation of the RFEA and the magnetic field direction when I_p is in the counterclockwise direction. Right: the notations of the upstream and the downstream direction when I_p is in the clockwise direction, and the magnetic field direction changes when I_p is reversed as shown in side view.

The previous T_i and T_e measurements were performed while I_p was in the counterclockwise direction viewed from the top of the STOR-M tokamak. A rotary motion manipulator was not available in the 2011 experiment. The probe can access different radial positions at a fixed angle. The probe was tilted $\approx +10^\circ$ to the right from the horizontal level to have good alignment with $\mathbf{B}$ while I_p was in the counterclockwise direction. While I_p was in the clockwise direction, poloidal magnetic field, B_θ, direction and total magnetic field direction

changed consequently as shown in Fig.4.10. The probe misalignment to the magnetic field line was expected to be $\approx 20^{\circ}$ in reverse I_p operation.

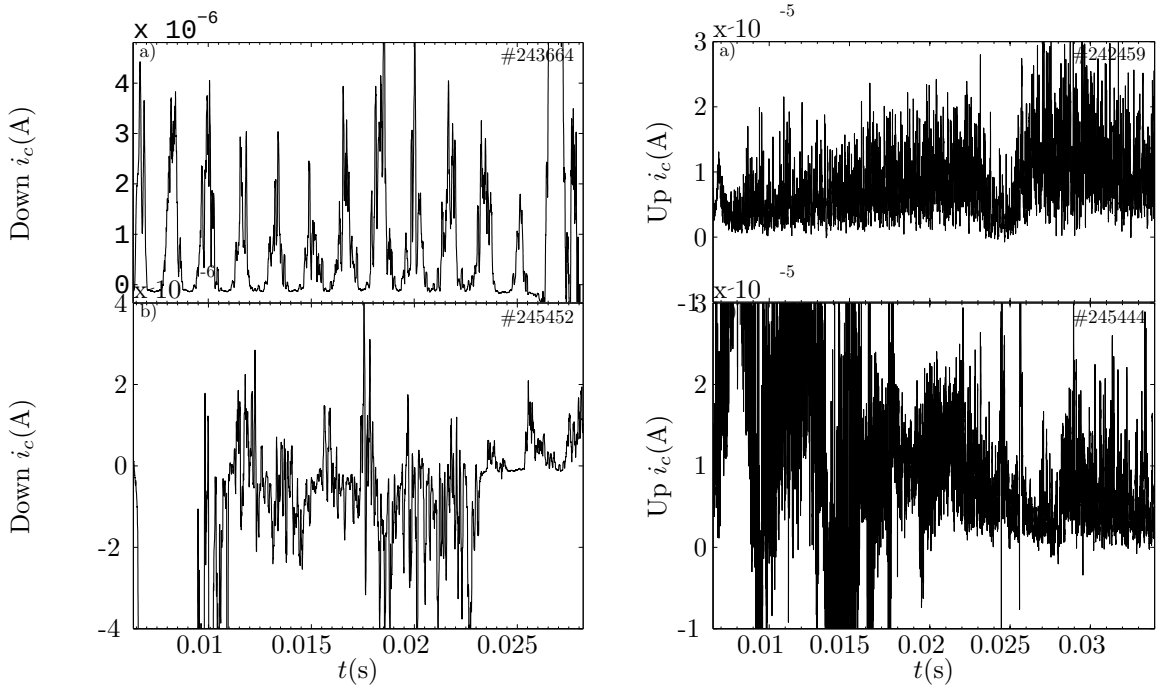

Figure 4.11: Left: The comparison of the downs i_c at the radial position of 13.5cm in standard mode operation while I_p was in the counterclockwise direction (top), and I_p was in the clockwise direction (bottom). Right: The comparison of the up i_c at the radial position of 12cm in DC mode operation while I_p was in the counterclockwise direction (top), and I_p was in the clockwise direction (bottom).

In standard mode operation, ion temperature value is extracted from the exponential slope of ion collector current. In DC mode operation, the method strictly demands positive current at the collector and at the grid 2 as given in Eq.2.6. The detail principle of each mode was discussed in Chap.2.2 and Chap.2.3. Data for standard mode and DC mode were collected by RFEA while I_p was in the counterclockwise and in the clockwise direction in 2011. The effect of magnetic field direction on ion current is shown in Fig.4.11. Referring to the left side of Fig.4.11, the exponential pattern of down i_c disappeared when I_p was in the clockwise direction in standard mode. From that, we cannot extract temperature information. Similar phenomenon occured in DC mode operation too. In DC mode, the negative i_c occured when I_p was in the clockwise direction. This indicates that the large misalignment of the RFEA

with magnetic field direction, $\approx 20°$, introduces abnormal behavior.

4.5 Comparison of Important Parameters for the RFEA Designs Used in the STOR-M, JET, and ISTTOK tokamaks

The parameters of the bidirectional RFEA currently used in the STOR-M tokamak are compared with the parameters from the JET RFEA [13] and the ISTTOK RFEA [12] [22]. During T_i measurement campaign, Two different slit designs were used. The parameters and the results are shown in Table.4.1.

Table 4.1: Some important parameters for the RFEAs

Parameter	**STOR-M**	**JET**	**ISTTOK**
Larmor radius(mm)	1.12	0.5	1.3
Critical current I_{max}^{C-L} in ion mode (µA)	110	250-360	230
Geometrical transmission (Grid 1)	0.56	0.81	0.8
Geometrical transmission (Grid 2)	0.81		
Entrance slit area (mm^2)(Slit 1)	0.047	0.12	0.28
Entrance slit area (mm^2)(Slit 2)	0.194		
Measured ion current on the upstream side (µA)(Slit 1)	25	80	15
Measured ion current on the downstream side (µA)(Slit 1)	14	35	
Measured ion current on the upstream side (µA)(Slit 2)	6		
Measured ion current on the downstream side (µA)(Slit 2)	3		
Measured current density on the upstream side ($\mu A\, mm^{-2}$)(Slit 1)	531	670	54
Measured current density on the upstream side ($\mu A\, mm^{-2}$)(Slit 2)	31		
Natural ambipolar collection length L_{col}^{amb} (m)	0.47	14	0.6
Magnetic connection length $L_{\parallel}$ (m)	0.72-2.16	40	1.41
Internal diameter of the RFEA (mm)	2.75	10	4

4.6 Space Charge Limitation

Although the RFEA did operate well under certain conditions, there were some regimes under which it did not. In 2010 T_i campaign, the RFEA operated abnormally at the radial

position of 12.5cm when the analyzed ion current increases. Even though the principles and design features of RFEA are simple, its abnormal behaviors (the potential variation across the entrance slit, space-charge limitation, secondary electron emission) are complicated [10]. Generation of negative i_c between $\approx$ 15ms and $\approx$ 18ms shown in Fig.4.12 indicates that the RFEA was in abnormal behavior, and a similar phenomenon is also reported in other RFEA. The phenomena observed in the JET [12], the ISTTOK [13], and the previous RFEA in the STOR-M [8] tokamaks have not yet been explained. Negative disruption current has been observed during T_i campaign when the location of the RFEA is deeper than r_c = 13.5cm. The experimentally measured currents when RFEA is operated normally are in the range of up to 14µA. The space-charge limited current predicted by Child-Langmuir limited current is 110µA. The predicted current is several times higher than the abnormally behavioral current. The similar situations are also reported in [12][13][8].

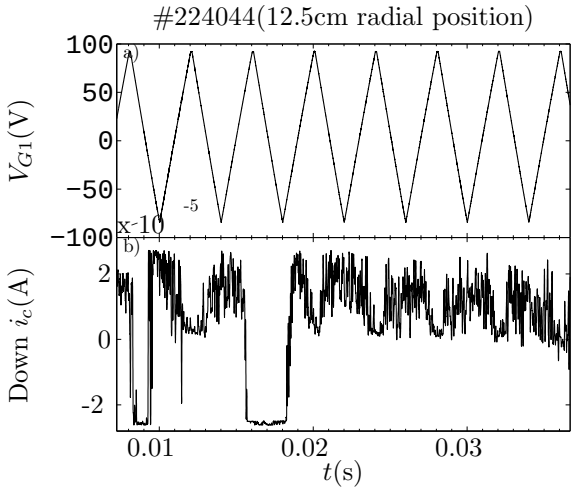

Figure 4.12: Typical abnormal RFEA signal collected at the radial position of 12.5cm in ion mode.

Chapter 5

Mechanical Structure

As shown in Fig.5.1, the RFEA includes protective housing, cover, insulators, grids, electrostatic shielding plate, and grid-positioning tube. Insulators separate electrodes. Grid-positioning tube aligns the grids. Electrostatic shielding plate prevents the electrostatic noise. Boron nitride housing protects the grids from high temperature environment. The Solidworks files are stored in `\\Spitzer\Work\LabOps\Equipment\STOR-M\ProbesinVacuum\bi_RFEA\SolidworksDesign`.

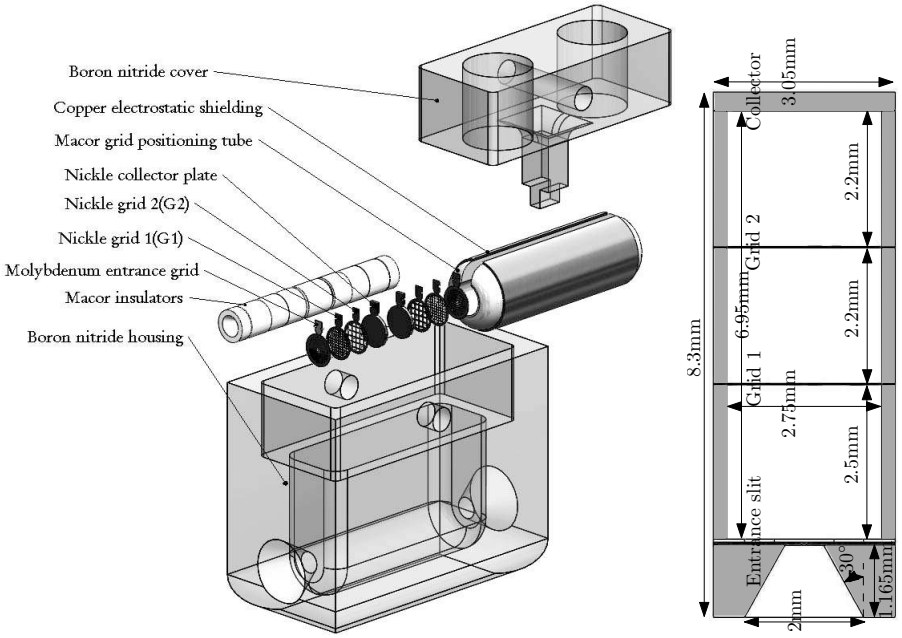

Figure 5.1: Left: exploded isometric decomposition view of the STOR-M RFEA probe head. Right: cross section view of an analyzer (not to scale).

The design shown in Fig.5.1 was chosen because of its compact and economical advantage. The design was based on commercially available transmission electron microscopy (TEM) grids because grids are the most expensive ones. In the design, the grids are sandwiched

between the insulators. The entrance slit 1 assembly consists of a stack of a molybdenum guard plate, a molybdenum grid with 54µm width hole, and a nickel slot grid. Molybdenum grid has 25µm thickness, and its part number is PYHD300-MO. It is available at Science Services GmbH, Goerzer Strasse 70 81549 Munich, Germany. Molybdenum guard plate has 25µm thickness and 0.4mm hole. Its part number is 1GM4H, and it is available at PYSER - SGI Limited Rircraft Way, United Kingdom. Nickel grid with 1×2mm slotted dimensions and 25µm thickness for wire connection is available at Ted Pella, Inc., Redding, CA 96049-2477, USA.

The experiment performed in 2011 used the tungsten entrance slit 2 which has 100µm thickness. It is available at GATEWAY laser services, 2345 Millpark Drive, Suite A, Maryland Heights, MO 63043, USA. Grid 1 and grid 2 made out of nickel are also available at Ted Pella, Inc., USA. Solid collector is not available commercially. We can obtain it by soft soldering a 3.05mm circular disk in front of a grid. A 5 mils thick electrostatic copper shield is available at Basic Copper, 1809 W. Main St. #244 Carbondale, IL 62901, USA. The TEM grids are very thin and fragile especially in their tabs. Placing tiny blown fuses among the grid tabs make their design stronger. Tiny fuses with the length of 2mm are available at Digikey Coporation, USA. Its part number is MFU0805.05CT-ND. Before placing them into the probe, fuses must be shorten to cut the connection inside. The location of fuse in the analyzer is shown in Fig.5.2.

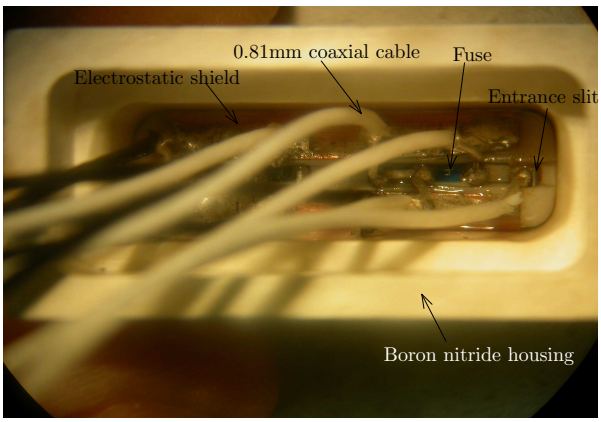

Figure 5.2: The inside of the RFEA.

The 27mm long probe body was machined from a single bar of boron nitride with AX05. The superior thermal and machinable properties of grade AX05 [43] over conventional hot-

pressed boron nitride makes it the best choice. It can be used in the atmosphere of over 2000° K. Grade AX05 can be machined to extremely close tolerances using standard high speed steel tool equipment. This is important for our small RFEA design. The material is available at Saint-Gobain Ceramics, 168 Creekside Drive, Amherst, NY 14228-2027, USA. The inner insulators and the grid-positioning tubes are made out of macor. Macor is able to withstand 0.15mm thin wall machining. The inner radius of an insulator should be greater than ion Larmor radius to avoid particles being scraped off. The outer diameter of the insulator should be the same size as the perimeter of the grids to keep them in place. PEP, Department of Physics and Engineering Physics, shop machined all the the insulating parts. The binding between the cover and the housing is achieved by using a 4-40×1" alumina screw. Ortech Ceramics (6720 Folsom Blvd. Suite219, Sacramento, CA 95819, USA) supplies the screw. Through use of the alumina screw, it is possible to replace the grids if necessary.

Chapter 6

Electronics

The input power supply circuit and the output data collection are the two main constituent parts in RFEA electronics. Ground loop occurs when a system is connected to more than one ground point. It can create an electric shock hazard because induced electromotive forces are produced across the ground loop due to the strong magnetic field produced by the tokamak. ISO-AMP in the RFEA electronics is for the purpose of breaking the ground loop. The Altium Designer files for ISO-AMP and power supply circuit are stored in `\\Spitzer\Work\LabOps\Equipment\STOR-M\ProbesinVacuum\bi_RFEA\Altium-designerCkt`

6.1 ISO-AMP and DAQ for the RFEA

Two parts of the output electronic system of a RFEA are the isolation amplifier, ISO-AMP, and the data acquisition system, DAQ. In the STOR-M tokamak, data acquisition system NI6133 from National Instruments are used. Since 1MHz sampling rate is much larger than the V_{G1} scanning frequency (1kHz), it conforms to the condition suggested by Nyquist-Shannon sampling theorem [44]. The output electronic system has to ensure that it provides original collector current waveform. The bandwidth of the data acquisition system is 1.3MHz. The bandwidth of a AD215BY is 120kHz. From the experimentally tested ISO-AMP system, the cutoff frequency of the system is 91kHz as shown in Fig.6.1. Since the cutoff frequency of the ISO-AMP system is high compared to the 1kHz sweeping bias of V_{G1}, the ISO-AMP doesn't suppress the amplitude of the collector current, and the phase delay is negligible. Note: if phase delay is significant, hysteresis pattern will involve in collector current (see Chap.4.2). The connections of the coaxial cables among the electronic systems of the RFEA should follow Fig.6.2 to avoid the ground loop.

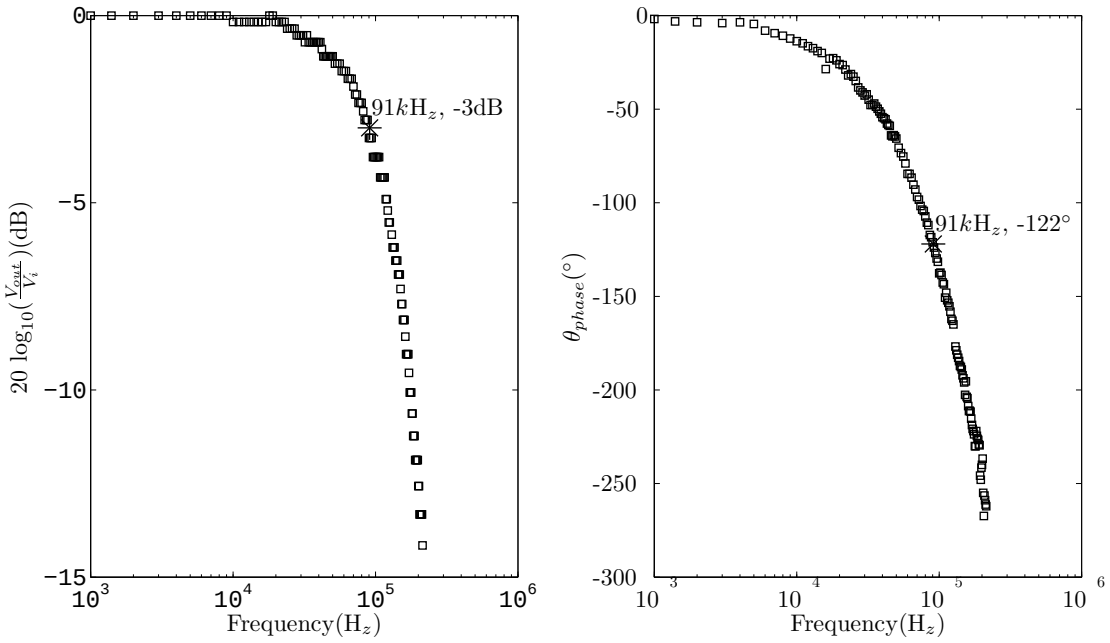

Figure 6.1: ISO-AMP circuit response to frequency. Left: Bode gain plot for the ISO-AMP. Right: Bode phase plot for the ISO-AMP.

In the ISO-AMP system, AD624AD op-amp is used as the differential amplifier. It amplifies the signal and suppresses the common noise picked up by the collector and the common mode rejection (the dummy wire), CMR, lines. The schematic diagram of the ISO-AMP system is shown in Fig.6.4. Note: CMR line is not connected to anywhere in the probe (see Fig.6.2 and Fig.6.3). It serves as an antenna. The detail explanation was given in Chap.4.2. Different gains are obtained by using SW-6WAY switch. It is useful when different radial positions give different ion saturation current. The relationship between the output terminal of the ISO-AMP and the input current is $i_c = \frac{V_{out}}{\mathrm{G}\times 15\mathrm{k}}$. G is the selected gain from the S1, and V_{out} is the output voltage produced by DAQ.

Isolated op-amp AD215BY has low Nonlinearity, ±0.005% [45]. It is used as unity gain isolation amplifier. HCNR200 optocoupler can be used as another option [46]. Build-in isolated power supply inside AD215BY helps the simplicity of the circuit design. 1500V_{rms} isolation provides pretty good voltage prevention for ground loop breaking. Printed circuit board, PCB, design of two channel ISO-AMP is shown in Fig.6.5. From the Altium file, the Gerber file can be generated by the steps as shown in [47]. The PCB two-layer board was

tested successfully with 500V for isolating input and output system. That PCB design is not only for the requirement of RFEA but also for general purposes.

If positive input level shifting is needed, R_+offset1 and R_+offset2 should be used. The required voltages at the input ends can be defined by voltage divided resistors via equations, $V \times \frac{\text{R6}}{(\text{R6})+(\text{R\_+offset1})}$ and $V \times \frac{\text{R3}}{(\text{R3})+(\text{R\_+offset2})}$. If negative voltages at the input ends are needed, R1 and R4 should be used. The voltage divisions are given by the equations, $V \times \frac{\text{R6}}{\text{R6+R1}}$ and $V \times \frac{\text{R3}}{\text{R3+R4}}$. Note: V is the supplied voltage to the ISO-AMP. If zero voltage is needed at the collector, just ignore R1, R4, R_+offset1, and R_+offset2. R3 is the adjustable resistor for compensating percentage error of R6. In our T_i measurement campaign, zero voltage had been applied to the collector of the RFEA. In_Com jumper passes the channel 1 ground to the channel 2. -15V_J, Out_GND_J and +15V_J are for exporting power to the second channel by using jumpers. R12 rheostat is for adjusting the DC output level. The output cable shields of the ISO-AMP system are connected to the ground and to the chassis of the system. Thus the switch to grounded input has to be used in the DAQ.

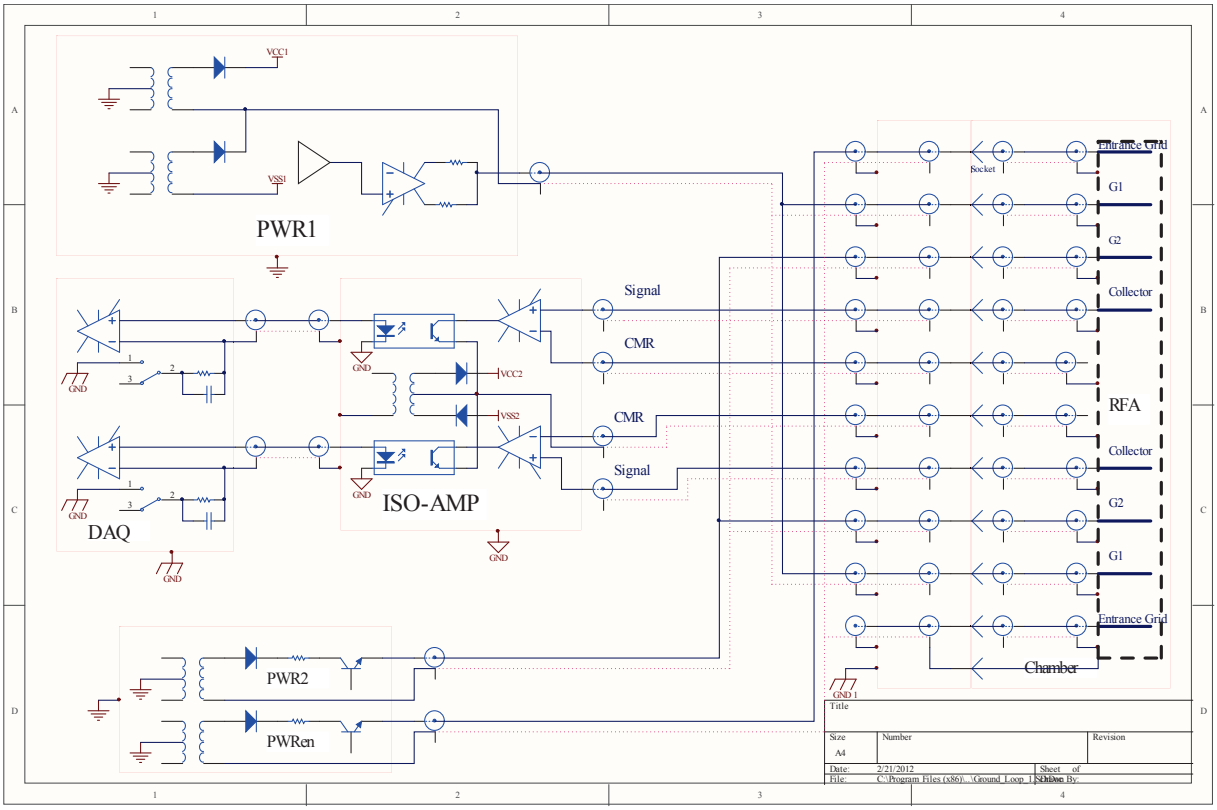

Figure 6.2: The outline of the electronic systems of the RFEA.

6.2 Power Supplies for the RFEA

There are four parts in RFEA input system. These are (1) entrance slit power supply, V_{en}, (2) the grid 1 power supply, V_{G1}, (3) the grid 2 power supply, and (4) the grid 1 monitoring circuit as shown in Fig.6.6.

The output V_{G1} and V_{G2} are controlled by the triggering pulse via the solid state relays, U11 and U10. When a monostable multivibrator, U5, receives the falling edge of a triggering pulse, it generates 1s wide pulse, and it turns on the relays. The voltages are supplied to the V_{G1} and the V_{G2} terminals during discharge. Since 0.81mm cables with the limited voltage of 200V AC per 1min are used inside the RFEA probe, it is the critical point compared to V_{G2} which has 220V and the maximum V_{G1} which has 150V. Minimum exposure time of the cable to high voltage is one of the key factors for a robust design. Turning off the voltage supplied to the terminals while tokamak is charging is also good from the safety point of view. By using switches s2, s4, and s6, one can select ion mode and electron mode. By using s3, one can select the various entrance slit potential, 0V, 37V, and 80V. The op-amp, U4, generates sawtooth waveform, and the transistor, Q1, amplifies the waveform. By turning the rheostats R11, R14, and R16, we can control scanning frequency, scanning DC level, and gain of the V_{G1} respectively. Isolation amplifier for V_{G1} monitoring, U9, is used for breaking ground loop between the chamber grounding point and the DAQ grounding point. For high voltage AC/DC convertors, commercially available IHB series in Mouser electronics are used.

6.3 Wire Connections Between the RFEA and the Feedthrough

Referring to the top of Fig.6.3, 20-pin feedthrough of part number 9132006 available from MDC Vacuum Products, Sarasota, FL USA, was used. The purpose of using bellows is to absorb mechanical shock produced during tokamak discharge. Very tiny 0.81mm coaxial cables are used inside the RFEA for limited space availability. A small tapered ceramic tube is placed between the wires and the alumina tube to cut the stress of external force exerted on the inner part of the RFEA while the probe is moving radially. A green color wire of part

number 83050 from BELDEN is used for high quality grounding. The conductor is made out of stranded silver-plated copper, and its overall diameter is 0.644mm.

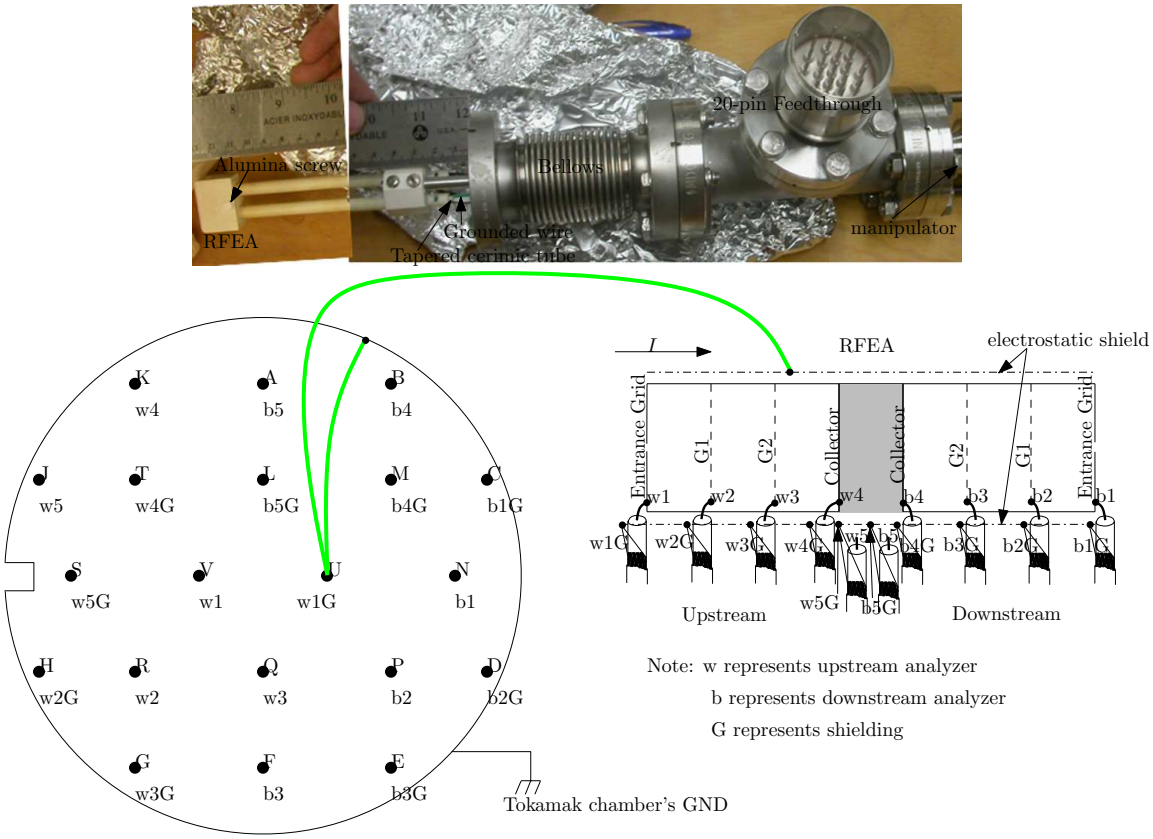

Figure 6.3: Top: a photo of the RFEA taken just before inserting into the chamber. Bottom: the schematic diagram of wiring between the feedthrough and the RFEA.

The cable connections between the RFEA and the feedthrough are shown at the bottom of Fig.6.3. Alphabets (A, B, C,... etc) are marked on the feedthrough. Note: the green color cable is the only cable that connects to the chamber ground. The coaxial outer conductors (b1G, b2G, b3G,... etc) connected to the RFEA shield on one end are connected to the feedthrough pins on the other end. Note: they are not connected to the ground on the feedthrough side to avoid ground loop. The coaxial outer conductors are connected to the feedthrough pins just for reinforcing the mechanical strength of the coaxial cable cores(b1, b2, b3,... etc). Since the cable is very small and fragile, w1 and b1, w2 and b2, and w3 and b3 are electrically connected in parallel outside the chamber, for simultaneous measurement of the downstream and the upstream sides. Signals at w4, w5, b4, and b5 are supplied to the ISO-AMP. w5 and b5 are used as antenna for removing the common noise picked up by

the cable w4 and b4 respectively.

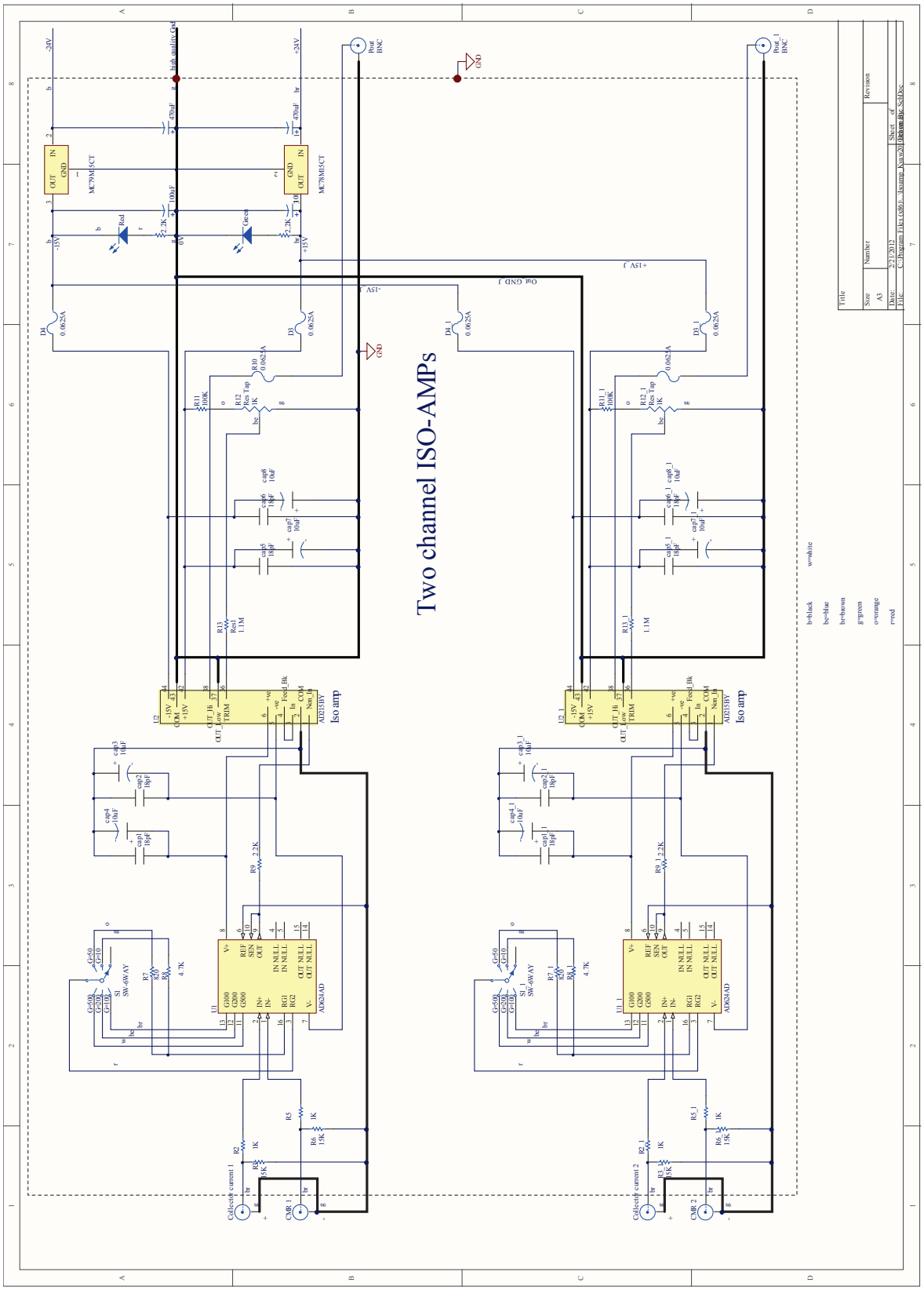

Figure 6.4: The schematic of two channel ISO-AMP system.

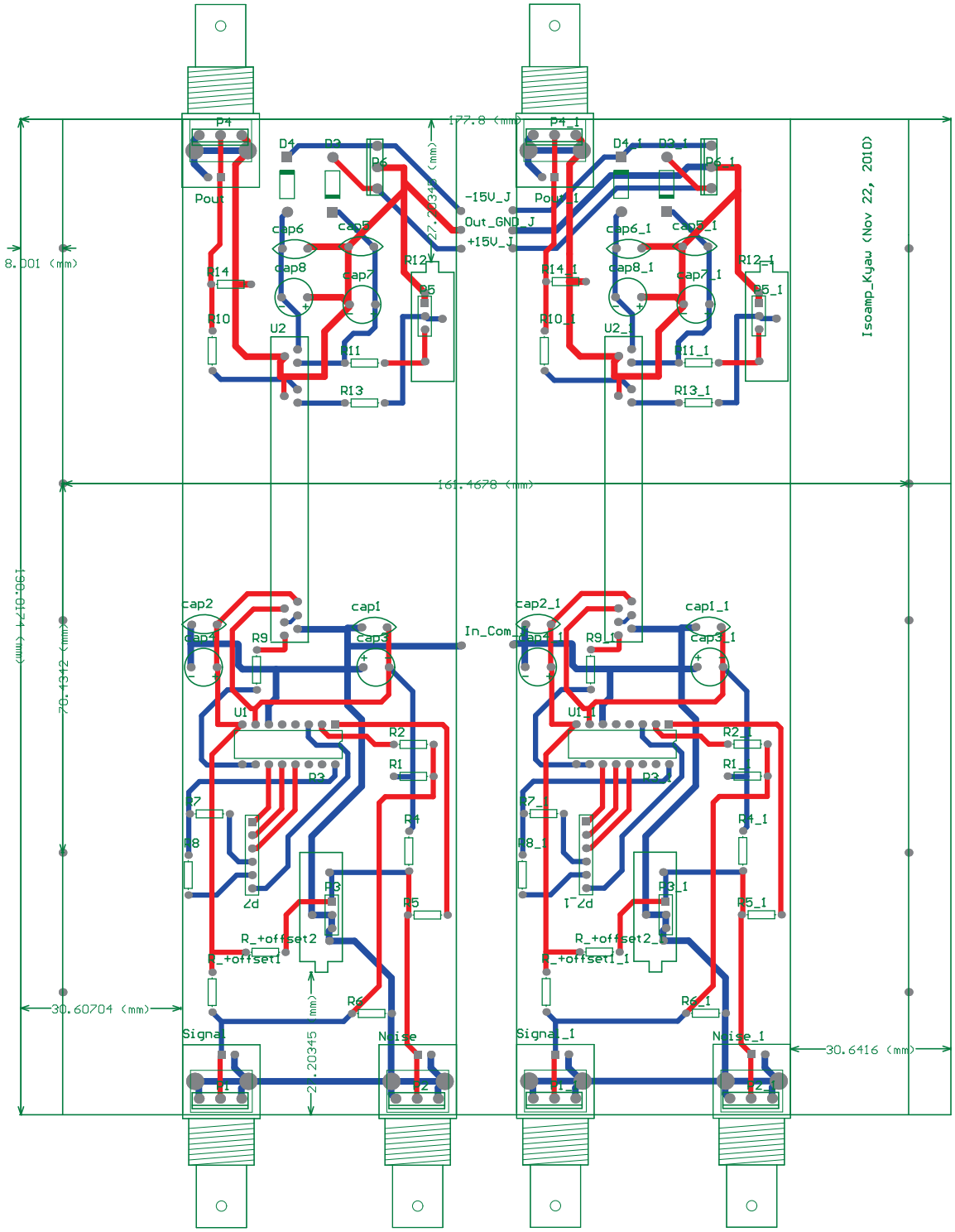

Figure 6.5: The PCB design of two channel ISO-AMP system.

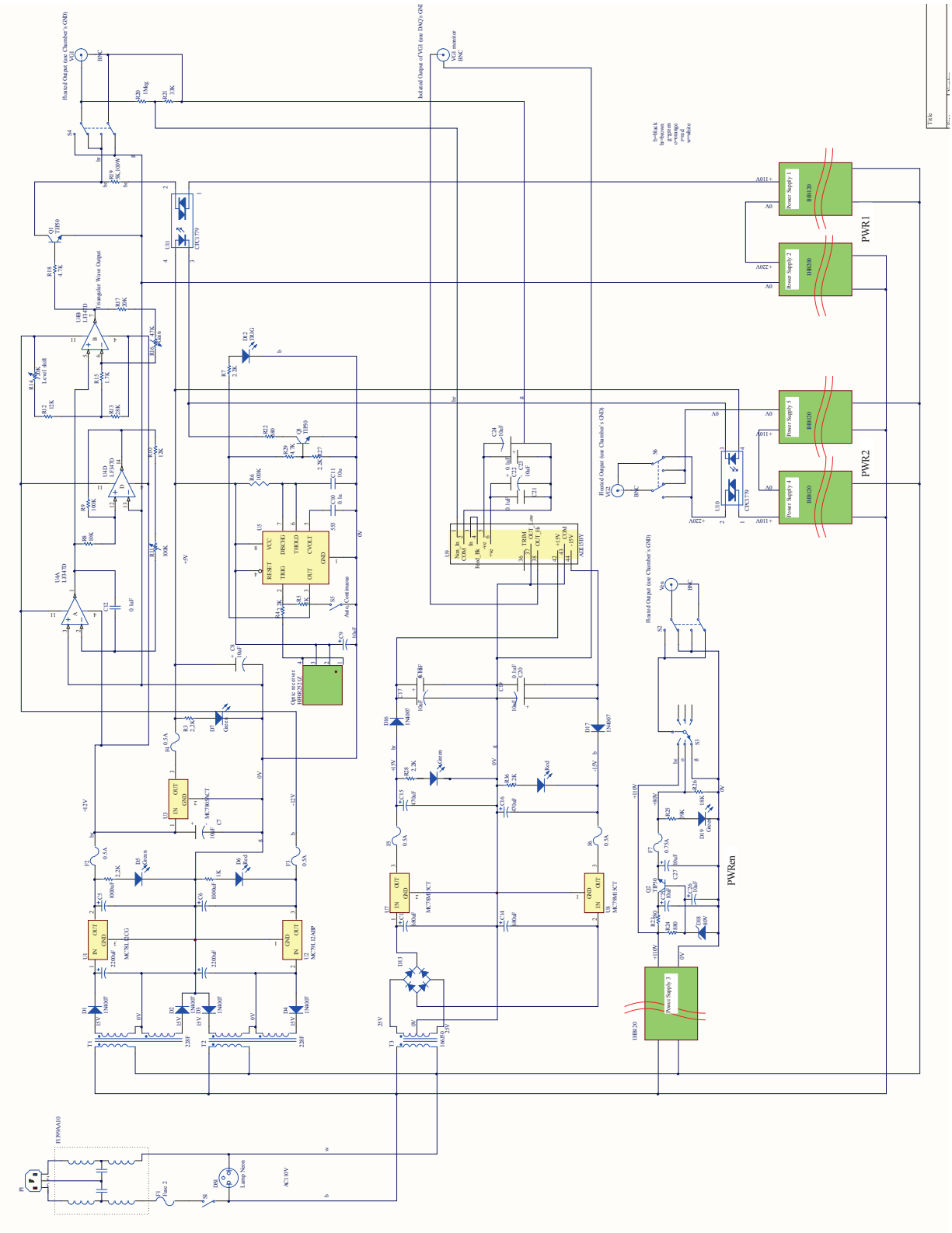

Figure 6.6: The schematic diagram of the power supply of the RFEA.

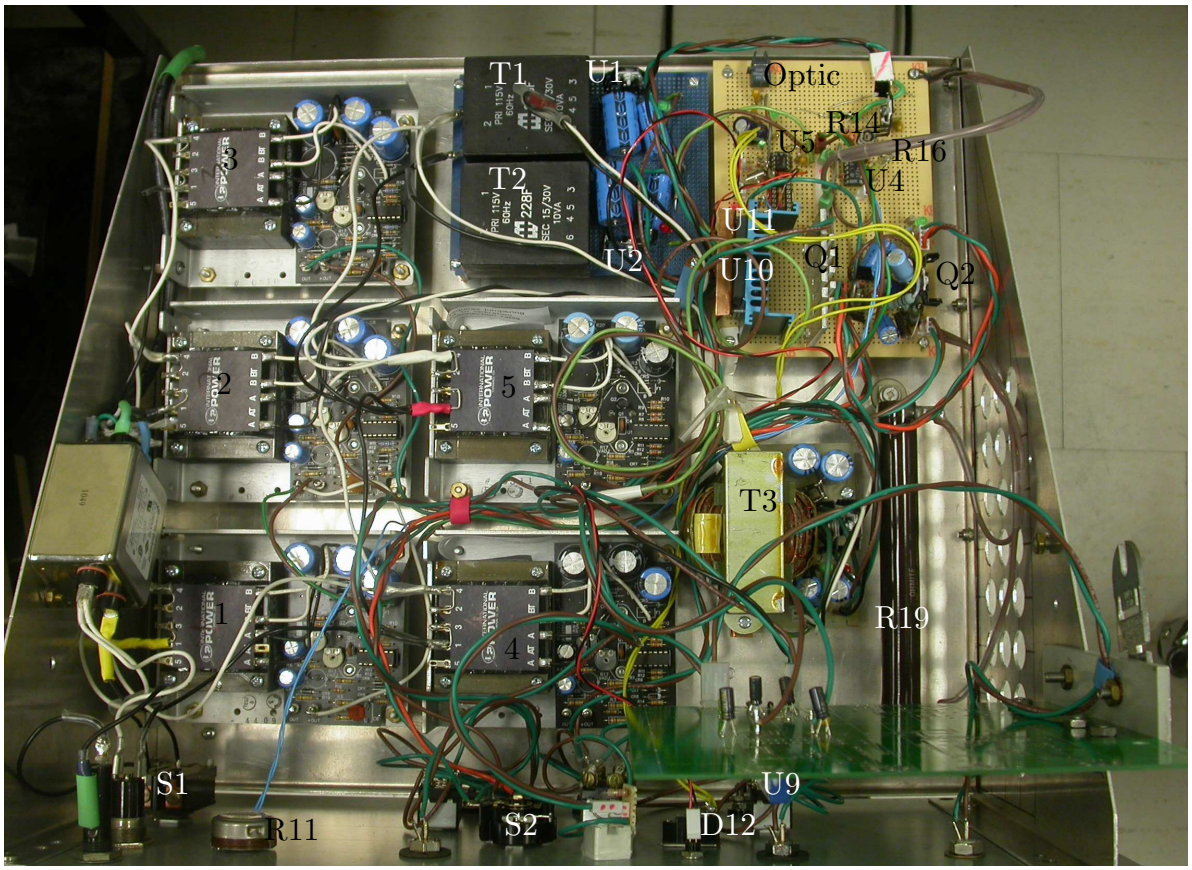

Figure 6.7: The power supply of the RFEA. Named components should be compared with the schematic diagram for tracing the circuit easily.

Chapter 7

Summary and Future Work

7.1 Summary

The work of my thesis can be summarized as follows:

- A simple, compact, and inexpensive bidirectional RFEA was built and employed in the STOR-M tokamak for T_i measurement.

- Measured T_i in the SOL region of the STOR-M tokamak by the bidirectional RFEA is from 19eV to 34eV. The ion temperature measured by previous single sided RFEA is between 14eV and 32eV in the SOL region. By the single sided RFEA, T_e, V_{shift}, and V_{G1} are initially required even though simultaneously measured Mach number is available [22]. Thus it is assumed that the direct averaging method performed by the bidirectional RFEA could provide more accurate results than the method used by the single sided RFEA.

- $\frac{T_i}{T_e}$ values in the SOL are between 1.8 and 2.8. It is frequently assumed that $T_i = T_e$ in the SOL by the plasma boundary community, but $T_i > T_e$ in the SOL except at high collisionality regimes [19][48].

- The RFEA operation is validated in e mode. T_e values were measured by the RFEA and the Triple probe simultaneously. The measured values are comparable when the probes are far away from the chamber.

- Large misalignment of magnetic field with the entrance slit plate, $\approx 20^{\circ}$, is crucial for both standard mode operation and DC mode operation.

- The probe should avoid ultra sonic cleansing and a huge amount of Torr Seal® applied on the probe head.

- Electronic circuit used in the current RFEA worked pretty well, and it is reliable.

7.2 Future Work

Much of the work of this thesis is devoted to commissioning of the bidirectional RFEA in the STOR-M tokamak in standard ramping mode. Several possible improvements to the mechanical structure and electronics of the RFEA are suggested.

- High current can be achieved by tapering the entrance slit surface (suggested by [21]). If possible, the entrance slit 2 should be tapered to achieve high current.

- Replace the linear positioner with a linear-rotary positioner to provide the rotational adjustment. A rotational manipulator may provide the maximum current with the probe head aligned to the magnetic field. It may probably help positive DC level shifting in DC mode operation.

- Try the experiment with large entrance slit openings ($4\lambda_{De}$, $6\lambda_{De}$) to test the entrance slit width criterion, $< 2\lambda_{De}$.

- Build the adjustable DC power supply (-150V, -250V, and -300V) for the grid 2 to test the effect of potential at the grid 2 on T_i values [11] in standard ramping mode.

- Build the adjustable DC power supplies for the grid 2 and the collector for DC mode operation.

- If possible, improve the monopolar sweeping at the grid 1 by replacing bipolar sweeping to investigate the knee voltage of the $I-V$ characteristic curve. By analyzing the knee structure of the characteristic curve, we can roughly speculate the space charge effect, the sheath potential drop at the entrance slit, and the potential perturbation across the entrance slit surface.

- Build the two pulse generators for the grid 1 and the collector to measure the secondary electron emission at the collector. The experimental setup is available in [10].

Bibliography

[1] M. Zucchetti. The Zero-Waste Option for Nuclear Fusion Reactors: Advanced Fuel Cycles and Clearance of Radioactive Materials. *Annals of Nuclear Energy*, 32:1584–1593, 2005.

[2] I. Cook, R. L. Miller, and D. J. Ward. Prospects for Economic Fusion Electricity. *Fusion Engineering and Design*, 63-64:25–33, 2002.

[3] D. J. Dallas. Diamagnetic Flux Measurements on the STOR-M Tokamak. Master's thesis, University of Saskatchewan, April 2009.

[4] S. Pfalzner. *An Introduction to Inertial Confinement Fusion*. CRC, 2006.

[5] V. P. Smirnov. Tokamak Foundation in USSR/Russia 1950-1990. *Nucl. Fusion*, 50:014003, 2010.

[6] K. Miyamoto. *Plasma Physics and Controlled Nuclear Fusion*. Springer, 2005.

[7] K. Miyamoto. *Fundamentals of Plasma Physics and Controlled Nuclear Fusion*. Iwanami, 1997.

[8] D. Rohraff. Ion Temperature Measurements in STOR-M Boundary Plasmas Using a Retarding Field Energy Analyzer. Master's thesis, University of Saskatchewan, August 2009.

[9] G. S. Yun, W. Lee, M. J. Choi, J. Lee, H. K. Park, C. W. Domier, N. C. Luhmann, Jr., B. Tobias, A. J. H. Donne, J. H. Lee, Y. M. Jeon, S. W. Yoon, and KSTAR Team. Two-Dimensional Imaging of Edge-Localized Modes in KSTAR Plasmas Unperturbed and Perturbed by n=1 External Magnetic Fields. *Phys. Plasmas*, 19:056114, 2012.

[10] R. T. Nachtrieb. *Ion Mass Spectrometry on the ALCATOR C-Mod Tokamak*. PhD thesis, Massachusetts Institute of Technology, March 2000.

[11] M. Kocan, J. P. Gunn, M. Komm, J. -Y. Pascal, E. Gauthier, and G. Bohmme. On the Reliability of Scrape-Off Layer Ion Temperature Measurements by Retarding Field Analyzers. *Rev. Sci. Instrum.*, 79:073502, 2008.

[12] R. A. Pitts and R. Chavan. Retarding Field Energy Analyzer for the JET plasma boundary. *Rev. Sci. Instrum.*, 74:4644–4657, 2003.

[13] I. S. Nedzelskiy, C. Silva, H. Figueiredo, H. Fernandes, and C. A. F. Varandas. Compact Retarding Field Energy Analyzer for the Tokamak ISTTOK Boundary Plasma. *Rev. Sci. Instrum.*, 77:10E729, 2006.

[14] F. Valsaque, and G. Manfredi. Kinetic Simulations of Ion Temperature Measurements from Retarding Field Analyzers. *Phys. Plasmas.*, 9:1806–1814, 2002.

[15] G. F. Matthews. A Combined Retarding Field Analyzer and E×B Probe for Measurement of Ion and Electron Energy Distribution in Tokamak Edge Plasmas. *J. Phys. D*, 17:2243–2254, 1984.

[16] M. Kocan, J. P. Gunn, J. -Y. Pascal, and E. Gauthier. Ion Temperature Measurements in the Tore Supra Scrape-Off Layer Using a Retarding Field Analyzer. *Contrib. Plasma Phys.*, 50:836–840, 2010.

[17] A. W. Molvik. Large Acceptance Angle Retarding Potential Analyzers. *Rev. Sci. Instrum.*, 52:704–711, 1981.

[18] J. P. Gunn, R. Schrittwieser, P. Balan, C. Ioniţă, J. Stöckel, J. Adámek, I. Ďuran, M. Hron, R. Hrach, M. Vicher, G. Van Oost, T. Van Rompuy, and E. Martines. Tunnel Probes for Measurements of the Electron and Ion Temperature in Fusion Plasmas. *Rev. Sci. Instrum.*, 75:4328–4330, 2004.

[19] M. Kocan, J. P. Gunn, S. Carpentier-Chouchana, A. Herrmann, A. Kirk, M. Komm, H. W. Muller, J. -Y. Pascal, R. A. Pitts, V. Rohde, and P. Tamain, ASDEX Upgrade and

Tore Supra Teams. Measurements of Ion Energies in the Tokamak Plasma Boundary. *J. Nucl. Mater.*, 415:S1133–S1138, 2010.

[20] A. S. Wan, T. F. Yang, B. Lipschultz, and B. LaBombard. Janus, a Bidirectional, Multifunctional Plasma Diagnostic. *Rev. Sci. Instrum.*, 57:1542, 1986.

[21] A. S. Wan. *Ion and Electron Parameters in the ALCATOR C Tokamak Scrape-Off Region.* PhD thesis, Massachusetts Institute of Technology, 1986.

[22] M. Dreval, D. Rohraff, C. Xiao, and A. Hirose. Retarding Field Energy Analyzer for the Saskatchewan Torus-Modified Plasma Boundary. *Rev. Sci. Instrum.*, 80:103505, 2009.

[23] I. S. Nedzelskiy, C. Silva, P. Duarte, and H. Fernandes. Ion Temperature Fluctuation Measurements Using a Retarding Field Analyzer. *Rev. Sci. Instrum.*, 82:043505, 2011.

[24] H. Y. Guo, G. F. Matthews, S. J. Davies, and S. K. Erents. Ion Temperature Measurements in JET Boundary Plasmas Using a Retarding Field Analyzer. preprint (1995), available at `http://www.iop.org/Jet/fulltext/JETP95062.pdf`.

[25] R. A. Pitts. *Ion Energy, Sheath Potential and Secondary Electron Emission in the Tokamak Edge.* PhD thesis, University of London, 1990.

[26] R. A. Pitts. Retarding Field Energy Analysis for Ion Temperature Measurement in the Tokamak Edge. *Contrib. Plasma Phys.*, 36:87–94, 1996.

[27] P. C. Stangeby. Large Probes in Tokamak Scrape-Off Plasmas. The Collisionless Scrape-Off Layer: Operation in the Shadow of Limiters or Divertor Plates. *J. Phys. D*, 18:1547–1559, 1985.

[28] G. M. R. St. Germaine. Plasma Flow Velocity Measurements with a Gundestrup Probe in the STOR-M Tokamak. Master's thesis, University of Saskatchewan, July 2006.

[29] W. Zhang, C. Xiao, and A. Hirose. Plasma Autobiasing During Ohmic H-Mode in the STOR-M Tokamak. *Phys. Fluids B*, 5:3961, 1993.

[30] O. Mitarai, C. Xiao, L. Zhang, D. McColl, W. Zhang, G. Conway, A. Hirose, and H. M. Skarsgard. Alternation Current Plasma Operation in the STOR-M Tokamak. *Nucl. Fusion.*, 36:1335, 1996.

[31] C. Xiao, K. K. Jain, W. Zhang, and A. Hirose. Measurement of Plasma Roatation Velocities with Electrode Biasing in the Saskatchewan Torus-Modified (STOR-M) Tokamak. *Phys. Plasmas.*, 1:2291–2296, 1994.

[32] S. Sen, C. Xiao, A. Hirose, and R. A. Cairns. Role of Parallel Flow in the Improved Mode on the STOR-M Tokamak. *Phys. Rev. Lett.*, 88:185001, 2002.

[33] J. E. Morelli. *Plasma Position Control in the STOR-M Tokamak: a Fuzzy Logic Approach*. PhD thesis, University of Saskatchewan, January 2003.

[34] Leybold-Heraeus Vacuum Products Inc. *TMP/NT 1000 Turbomolecular Pump and Frequency Converter Manual*.

[35] Leybold Vacuum Products Inc. *Trivac A Dual Stage Rotary Vane Pump Manual*.

[36] Veeco Instruments Inc. *Precision Leak Valve PV-10 Operation and Maintenance*.

[37] I. H. Hutchinson. *Principles of Plasma Diagnostics*. Cambridge University, 1987.

[38] Tech-X Corporation, 5621 Arapahoe Avenue, Suite A, Boulder, CO 80303, USA. *OOPIC Pro User's Guide*, 2 edition.

[39] P. Tamain, M. Kocan, J. Gunn, A. Kirk, J. -Y. Pascal, M. Price. Ion Energy Measurements in the Scrape-Off Layer of MAST Using a Retarding Field Analyzer. *J. Nucl. Mater.*, 415:S1139–S1142, 2011.

[40] M. Kocan and J. P. Gunn. Influence of Impurities on Ion Temperature Measurements in the Tokamak Scrape-Off Layer by Retarding Field Analyzers. *Plasma Phys. Control. Fusion*, 53:085016, 2011.

[41] Analog Devices. *Precision Instrumentation Amplifier AD624*.

[42] M. Dreval, C. Xiao, D. Trembach, A. Hirose, S. Elgriw, A. Pant, D. Rohraff, and T. Niu. Simultaneous Evoluation of Plasma Rotation, Radial Electric Field, MHD Activity and Plasma Confinement in the STOR-M Tokamak. *Plasma Phys. Control. Fusion*, 50, 2008.

[43] Combat Boron Nitride Grade AX05. Technical report, Saint-Gobain Ceramics.

[44] F. L. Lou, H. Ye, and M. H. Rashid. *Digital Power Electronics and Applications*. Elsevier Academic, 2005.

[45] 120kH_z Bandwidth, Low Distortion, Isolation Amplifier, AD215. Technical report, Analog Devices, 1996.

[46] High-Linearity Analog Optocouplers, HCNR200. Technical report, Hewlett Packard.

[47] H. J. Koch. How to Export Gerber Files from Altium Designer (Protel) Matching Olimex' PCB Production. 2009.

[48] M. Kocan, R. Panek, J. P. Gunn, J. Stockel, J. D. Skalny. 32nd eps conference on plasma phys, tarraona. In *A New Probe for Ion Temperature Measurements in the Tokamak Scrape-Off Layer*, 2005.

[49] M. A. Lieberman and A. J. Lichtenberg. *Principles of Plasma Discharges and Materials Processing*. John Wiley and Sons, second edition, 2005.

[50] F. F. Chen. *Introduction to Plasma Physics and Controlled Fusion*. Plenum, second edition, 1984.

[51] A. Dinklage, T. Klinger, G. Marx, and L. Schweikhard (Eds.). *Plasma Physics Confinement, Transport and Collective Effects*. Springer, 2005.

[52] A. I. Smolyakov. Phys461.3. University Assignments and Solutions, 2010.

[53] X. Zou, J-Y. Liu, Y. Gong, Z-X. Ohno, Y. Liu, and X-G. Wang. Plasma Sheath in a Magnetic Field. *Vacuum*, 73:681–685, 2004.

[54] B. P. Pandey, A. Samarian, and S. V. Vladimirov. Plasma Sheath in the Presence of an Oblique Magnetic Field. *Plasma Phys. Control. Fusion*, 50:055003, 2008.

Appendix A

Sheath Theory

Sheath boundary problem is important in the theory of material interfaced probes or in the interaction of a plasma with the limiter or divertor plate in tokamak.

A.1 Boltzmann Relation

In thermal equilibrium, the density of electrons at varying positions in a plasma follows Boltzmann distribution. In the absence of electron drifts ($u_e = 0$), the inertial, magnetic, and frictional forces are zero. The electron force balance with $\frac{\partial}{\partial t} = 0$,

$$en_e\mathbf{E} + \nabla p_e = 0 \tag{A.1}$$

Since electric field is the gradient of the electric scalar potential, $-\nabla\phi$, and pressure, p_e, can be written as $n_e kT_e$,

$$en_e\nabla(-\phi) + kT_e\nabla n_e = 0 \tag{A.2}$$

where T_e is electron temperature, and it is constant. By applying the identity $\frac{1}{f}\frac{df}{dx} = \frac{d\ln f}{df}\frac{df}{dx} = \frac{d\ln f}{dx}$, it gives

$$\begin{aligned} \nabla e\phi - kT_e\frac{1}{n_e}\nabla n_e &= 0 \\ \nabla e\phi - kT_e\nabla\ln n_e &= 0 \\ \nabla(e\phi - kT_e\ln n_e) &= 0 \end{aligned} \tag{A.3}$$

Eq.A.3 implies that

$$e\phi - kT_e\ln n_e = K \tag{A.4}$$

By applying the boundary condition, $n_e|_{\phi=0} = n_0$,

$$K = -kT_e\ln n_0 \tag{A.5}$$

When Eq.A.5 is plugged into Eq.A.4, Eq.A.4 becomes

$$\begin{aligned} n_e(\mathbf{r}) &= n_0\exp\left(\frac{e\phi(\mathbf{r})}{kT_e}\right) \\ n_e &= n_0\exp\left(\frac{\phi}{T_e(\mathrm{eV})}\right) \end{aligned} \tag{A.6}$$

Eq.A.6 is Boltzmann relation for electrons. From the above equation, when positive potential is increased, number of electron density increases.

We can drive the Boltzmann relation for positive ions by a similar way. Since electric field direction of electrons and ions are opposite, $-en_i\mathbf{E}$ is replaced instead of $en_e\mathbf{E}$ in Eq.A.1.

$$n_i = n_0 \exp\left(\frac{-\phi}{T_i(\mathrm{eV})}\right) \tag{A.7}$$

Eq.A.7 suggests that positive ions in thermal equilibrium are repelled from regions of positive potential. The above derivation follows [49].

A.2 Debye Length in a Plasma

This section discusses the ability of a plasma to shield DC electric fields. For plasmas much bigger in dimension than a Debye length, the shielding is extremely effective. The following derivation follows [50]. With the assumption of a uniform ion density ($n_i = n_0$) and the Boltzmann relation of electron density, $n_e = n_0 \exp(\frac{e\phi}{kT_e})$, 1D Poisson equation can be written as

$$\frac{d^2\phi}{dx^2} = \frac{en_0}{\epsilon_0}\left(\exp\left(\frac{e\phi}{kT_e}\right) - 1\right) \tag{A.8}$$

If we assume $e\phi \ll kT_e$, Eq.A.8 becomes by Taylor expansion, to the lowest order in $\frac{e\phi}{kT_e}$,

$$\frac{d^2\phi}{dx^2} = \frac{en_0}{\epsilon_0}\frac{\phi}{T_e(\mathrm{eV})} \tag{A.9}$$

The general solution of standard second order differential equation is

$$\phi = K_6 \exp\left(\frac{x}{\sqrt{\frac{\epsilon_0 T_e(\mathrm{eV})}{en_0}}}\right) + K_7 \exp\left(\frac{x}{-\sqrt{\frac{\epsilon_0 T_e(\mathrm{eV})}{en_0}}}\right) \tag{A.10}$$

By applying the conditions, $\phi|_{x=0} = \phi_0$ and $\phi|_{|x|\to\infty} = 0$, Eq.A.10 becomes

$$\phi = \phi_0 \exp\left(-\frac{|x|}{\sqrt{\frac{\epsilon_0 T_e(\mathrm{eV})}{en_0}}}\right) \tag{A.11}$$

Eq.A.11 leads to the definition of characteristic length scale

$$\lambda_{De} = \sqrt{\frac{\epsilon_0 T_e(\mathrm{eV})}{en_0}} = \sqrt{\frac{\epsilon_0 kT_e}{e^2 n_0}} \tag{A.12}$$

Sometimes λ_{De} is defined as e-folding length scale of a sheath because the potential, ϕ_0, drops by a factor of $\exp(-1)$ at $|x| = \lambda_{De}$ in Eq.A.11. In a sheath, potential drops more rapid than potential in a vacuum.

A.3 Sheath

Analytical calculation of a high voltage sheath will be introduced in the later part of this section. The calculation shows the thickness of the sheath is of the order of several electron Debye length. At the sheath edge, most of the electrons are repelled. With this qualitative picture in hand, plasma potential, ϕ_p, is derived from the assumption of floated wall.

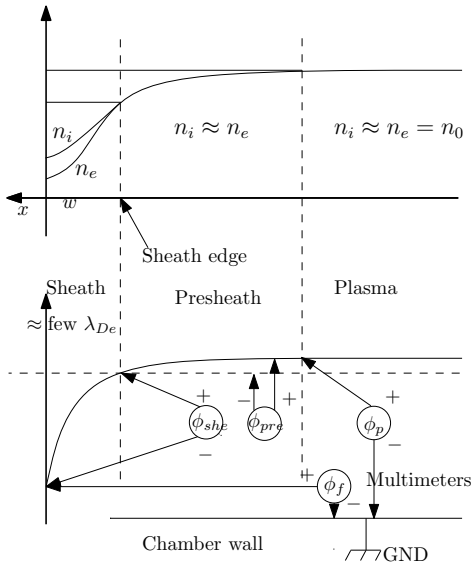

Figure A.1: Qualitative behavior of a sheath and a presheath while plasma is in contact with a conductor. In the presheath, quasineutral condition is hold. Multimeters represented by circles help us to see the clear reference points of respective potential differences.

While a conductor is inserted into a plasma, the electrode will be negatively charged because the electron thermal velocity $\sqrt{\frac{eT_e(\mathrm{eV})}{m_e}}$ is ≈50 times larger than the ion thermal velocity $\sqrt{\frac{eT_i(\mathrm{eV})}{m_i}}$ when T_i is assumed to be equal to T_e. The plate which has negative electric potential repels electrons, and it is surrounded by ions. Density and potential profiles are shown in Fig.A.1. Bohm sheath criterion suggests that a small potential drop ,$\phi_{pre} = \frac{1}{2}\frac{kT_e}{e}$ [51], is required to accelerate positive ions to ion sound speed, c_s. Since the conductor surface is floated, the net current is zero, $i_e + i_i = 0$. Assume $T_i = T_e$ [21]. Ion current, i_i, and electron current, i_e, are given as follows with the quasineutral condition:

$$\begin{aligned} i_e &= en_e\sqrt{\frac{kT_e}{2\pi m_e}}\exp(-\frac{1}{2})\exp(-\frac{e\phi_{she}}{kT_e}), \\ i_i &= en_i\sqrt{\frac{kT_e}{m_i}}\exp(-\frac{1}{2}), \\ n_i &= n_e \text{ (quasineutral at the sheath edge)} \end{aligned} \tag{A.13}$$

By solving a group of Eq.A.13 in floating condition, ϕ_{she} becomes

$$\begin{aligned}\phi_{she} &= \frac{1}{2}\frac{kT_e}{e}\ln(\frac{m_i}{2\pi m_e}),\\ \phi_{she} &= 2.8\frac{kT_e}{e} \qquad \text{(for hydrogen atom)}\end{aligned} \tag{A.14}$$

The above derivation follows [51]. Since the floating potential on the conductor can be written as $\phi_f = \phi_p - \phi_{she} - \phi_{pre}$ and $\phi_{pre} = \frac{1}{2}\frac{kT_e}{e}$,

$$\begin{aligned}\phi_f &= \phi_p - \phi_{she} - \phi_{pre},\\ \phi_f &= \phi_p - 2.8\frac{kT_e}{e} - 0.5\frac{kT_e}{e},\\ \phi_f &= \phi_p - 3.33T_e(\text{eV})\end{aligned} \tag{A.15}$$

where ϕ_{she} is the potential drop in the sheath in V, ϕ_{pre} is the potential drop in the presheath in V, ϕ_f is the floating potential measured in V, ϕ_p is the plasma potential in V, and T_e is the electron temperature in eV. If we neglect the presheath and assume $\phi_f = 0$ in Eq.A.15, $\phi_p = \phi_{she}$.

Consider a plasma of width, l, with $n_i = n_e$ initially confined between two grounded, $\phi = 0$, absorbing walls. Because the net charge density, $\rho = e(n_i - n_e)$, is zero, the electric potential, ϕ, and the electric field, E_x, is zero everywhere. Hence, the fast-moving electrons are not confined and will rapidly be lost to the walls. On a very short timescale, however, some electrons near the walls are lost. Note: $v_{Ti} \ll v_{Te}$. Thin positive sheaths form near each wall in which $n_i \gg n_e$. The net positive charge density, ρ, within the sheaths leads to a potential profile that is positive within the plasma, and the potential falls sharply to zero near both walls.

If we assume the sheath voltage is very large compared to T_e, the decreasing potential inside the sheath with respect to the sheath edge has enough energy to repel all of the incoming electrons [49]. For simplicity, high voltage sheath also known as a matrix sheath was assumed for estimating sheath thickness, δ.

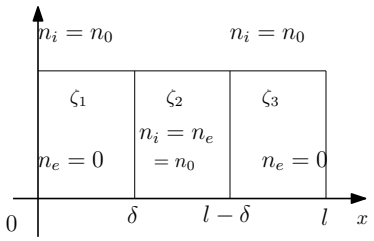

Figure A.2: Density distributions in a matrix sheath.

Referring to Fig.A.2, ion density, n_i, is assumed to be uniform in all regions. Electron density is zero in regions ζ_1 and ζ_3. Electron density is n_0 in ζ_2 region. By following the calculation in [52], consider 1D Poisson equation for estimating sheath thickness:

$$\frac{d^2\phi}{dx^2} = -\frac{en}{\epsilon_0} \tag{A.16}$$

If we integrate the poisson equation in region ζ_1, region ζ_2, and region ζ_3 and apply the conditions $n_e(\zeta_1, \zeta_3) = 0$ and $n_e(\zeta_2) = n_0$, then

$$\begin{aligned} \frac{d\phi}{dx} &= -\frac{en_0}{\epsilon_0}x + K_1 \qquad (\zeta_1) \\ \frac{d\phi}{dx} &= 0 \qquad (\zeta_2) \\ \frac{d\phi}{dx} &= -\frac{en_0}{\epsilon_0}x + K_2 \qquad (\zeta_3) \end{aligned} \tag{A.17}$$

By applying the conditions $\frac{d\phi}{dx}|_{\zeta_1} = \frac{d\phi}{dx}|_{\zeta_2}$ at δ and $\frac{d\phi}{dx}|_{\zeta_2} = \frac{d\phi}{dx}|_{\zeta_3}$ at $l - \delta$,

$$\begin{aligned} K_1 &= \frac{en_0}{\epsilon_0}\delta \\ K_2 &= \frac{en_0}{\epsilon_0}(l - \delta) \end{aligned} \tag{A.18}$$

where K_1 and K_2 are the integrating constants here. By plugging Eq.A.18 into Eq.A.17,

$$\begin{aligned} E = -\frac{d\phi}{dx} &= \frac{en_0}{\epsilon_0}(x - \delta) \qquad (\zeta_1) \\ E = -\frac{d\phi}{dx} &= 0 \qquad (\zeta_2) \\ E = -\frac{d\phi}{dx} &= \frac{en_0}{\epsilon_0}(x - l - \delta) \qquad (\zeta_3) \end{aligned} \tag{A.19}$$

where $E = -\frac{d\phi}{dx}$ is the electric field here. Note: E also represented as energy per reaction in Chap.1.1. Integrating Eq.A.19 results in

$$\begin{aligned} \phi &= -\frac{en_0}{\epsilon_0}(\frac{x^2}{2} - \delta x) + K_3 \qquad (\zeta_1) \\ \phi &= K_4 \qquad (\zeta_2) \\ \phi &= -\frac{en_0}{\epsilon_0}(\frac{x^2}{2} - lx - \delta x) + K_5 \qquad (\zeta_3) \end{aligned} \tag{A.20}$$

where K_3, K_4, and K_5 are the constants of integrations. Applying the boundary conditions $\phi|_{x=0} = 0$, $\phi|_{\zeta_1} = \phi|_{\zeta_2}$ at δ, and $\phi|_{\zeta_2} = \phi|_{\zeta_3}$ at $(l - \delta)$ gives

$$\begin{aligned} K_3 &= 0 \\ K_4 &= -\frac{en_0}{\epsilon_0}(\frac{\delta^2}{2}) \\ K_5 &= -\frac{en_0}{\epsilon_0}(\frac{l^2}{2} - l\delta) \end{aligned} \tag{A.21}$$

By plugging Eq.A.21 into Eq.A.20

$$\begin{aligned}
\phi &= -\frac{en_0}{\epsilon_0}(\frac{x^2}{2} - \delta x) \qquad (\zeta_1) \\
\phi &= \frac{en_0}{\epsilon_0}(\frac{\delta^2}{2}) \qquad (\zeta_2) \\
\phi &= -\frac{en_0}{\epsilon_0}(\frac{x^2+l^2}{2} + (\delta - l)x - \delta l) \qquad (\zeta_3)
\end{aligned} \tag{A.22}$$

If we assume $\phi_{she} = \phi = 2.8\frac{kT_e}{e}$(Eq.A.14) at $x = \delta$, the matrix sheath thickness, δ, is

$$\begin{aligned}
2.8\frac{kT_e}{e} &= -\frac{en_0}{\epsilon_0}(\frac{x^2}{2} - \delta x) \\
\delta &= \sqrt{5.6\frac{kT_e\epsilon_0}{e^2 n_0}} \\
\delta &= \sqrt{5.6}\lambda_{De}
\end{aligned} \tag{A.23}$$

The sheath thickness is of the order of Debye length.

A.4 Sheath in a Magnetic Field

Magnetic field, **B**, is normally ignored while studying plasma boundary sheath. In some cases, the effect of **B** cannot be ignored in strong magnetic field devices like tokamak. In a magnetic field, electrons and ions move no longer in straight lines, but they rotate around the magnetic field lines in Larmor radius. X. Zou and his group [53] emphasizes the case how the magnitude and the direction of magnetic field affect ion density, ion velocity, electron density, and potential variation in a collisionless sheath for $\tau = \frac{T_{i0}}{T_e} = 1$. Based on [53], we study the case of $\tau = 2$ which is the tokamak SOL parameter.

We consider the external magnetic field, **B**, is embedded on the $x - z$ plane with θ degree tilt regarding to the x axis as shown in Fig.A.3. While particle 1 is continuously accelerated between time intervals, t_1 and t_2, and t_2 and t_3, by traveling through plasma potential gradient, particle 2 is decelerated between t_1 and t_2, and it is accelerated between t_2 and t_3. This experiencing of nonuniform potential of particle 2 causes ion velocity fluctuation and density fluctuation. First we assume electrons and ions are isothermal. The electrons are assumed to be in isothermal equilibrium with the density given by

$$n_e = n_0 \exp(\frac{e\phi}{kT_e}) \tag{A.24}$$

The ion continuity equation and the ion equation of motion equation are

$$\nabla \cdot (n_i \mathbf{v}_i) = 0 \tag{A.25}$$

$$m_i \mathbf{v}_i \cdot \nabla \mathbf{v}_i = -e\nabla\phi + e\mathbf{v}_i \times \mathbf{B} \qquad \text{(collsionless condition)} \tag{A.26}$$

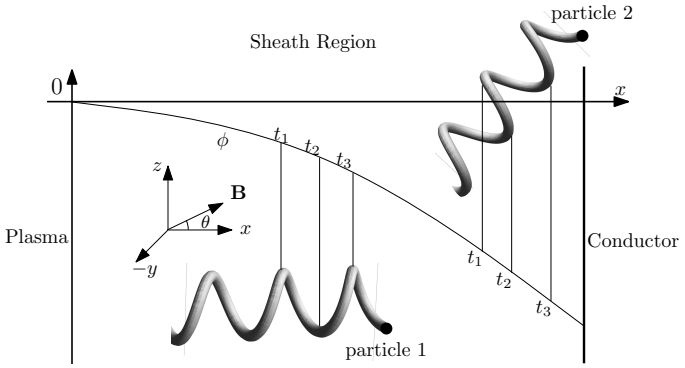

Figure A.3: Geometry of a magnetic sheath model with particle 1 gyrating about perpendicular magnetic field line while particle 2 gyrating about oblique magnetic field.

where m_i is the ion mass, $\mathbf{v}_i$ is the ion velocity, e is the electric charge, ϕ is the electric potential, and $\mathbf{B}$ is the magnetic field. Poisson equation is

$$\bigtriangledown^2\phi = -e\frac{(n_i - n_e)}{\epsilon_0} \tag{A.27}$$

For 1D analysis, Eq.A.25 and Eq.A.27 become

$$\frac{\partial^2\phi}{\partial x^2} = -e\frac{(n_i - n_e)}{\epsilon_0} \tag{A.28}$$

$$\frac{\partial(n_i v_{ix})}{\partial x} = 0$$

$$n_i v_{ix} = K \tag{A.29}$$

Since $n_i = n_0$ and $v_{ix} = v_{i0}$ at the sheath edge,

$$K = n_0 v_{i0}$$

$$n_i v_{ix} = n_0 v_{i0} \tag{A.30}$$

Ion sound speed, ion cyclotron frequency, ion Larmor radius, and electron Debye length are defined as:

$$c_s = \sqrt{\frac{kT_e}{m_i}}, \qquad \omega_{ci} = \frac{eB}{m_i}, \qquad r_{Li} = \frac{m_i v_{i\perp}}{eB} = \sqrt{2\tau}\sqrt{\frac{m_i kT_e}{e^2B^2}} = \sqrt{2\tau}\frac{c_s}{\omega_{ci}}, \qquad \lambda_{De} = \sqrt{\frac{\epsilon_0 kT_e}{n_0 e^2}} \tag{A.31}$$

The non-dimensional forms of the parameters are

$$
\begin{aligned}
M_i &= \frac{v_{i0}}{c_s} \qquad \gamma = \frac{\lambda_{De}}{r_{Li}} \qquad \tau = \frac{T_{i0}}{T_e} \quad (T_e \text{ is constant}) \qquad \mathrm{n}_i = \frac{n_i}{n_0}, \\
\mathrm{n}_e &= \frac{n_e}{n_0}, \qquad \mathrm{x} = \frac{\omega_{ci} x}{c_s} = \frac{\sqrt{2\tau} x}{r_{Li}}, \qquad \mathrm{v}_{ix} = \frac{v_{ix}}{c_s}, \qquad \mathrm{v}_{iy} = \frac{v_{iy}}{c_s}, \\
\mathrm{v}_{iz} &= \frac{v_{iz}}{c_s}, \qquad \phi = -\frac{e\phi}{kT_e} = -\frac{\phi}{T_e(\mathrm{eV})}
\end{aligned} \tag{A.32}
$$

where M_i is the ion Mach number, γ is the ratio of electron Debye length to ion Larmor radius, ϕ is the normalized potential, etc. If we apply non-dimensional parameters in Eq.A.24 and Eq.A.30, they become

$$
\begin{aligned}
\mathrm{n}_e &= \exp(-\phi) \\
\mathrm{n}_i \mathrm{v}_{ix} &= M_i
\end{aligned} \tag{A.33}
$$

Assuming $\mathbf{B} = \cos(\theta)\hat{x} + \sin(\theta)\hat{z}$, the equation of motion (Eq.A.26) and Poisson equation becomes

$$
\begin{aligned}
\mathrm{v}_{ix}\frac{\partial \mathrm{v}_{ix}}{\partial \mathrm{x}} &= \frac{\partial \phi}{\partial \mathrm{x}} + \mathrm{v}_{iy}\sin(\theta) \\
\mathrm{v}_{ix}\frac{\partial \mathrm{v}_{iy}}{\partial \mathrm{x}} &= -\mathrm{v}_{ix}\sin(\theta) + \mathrm{v}_{iz}\cos(\theta) \\
\mathrm{v}_{ix}\frac{\partial \mathrm{v}_{iz}}{\partial \mathrm{x}} &= -\mathrm{v}_{iy}\cos(\theta) \\
\frac{d^2\phi}{d\mathrm{x}^2} &= \frac{1}{2\tau}\frac{(\mathrm{n}_i - \exp(-\phi))}{\gamma^2}
\end{aligned} \tag{A.34}
$$

By applying the conditions, $M_i = 1, \phi|_{\mathrm{x}=0} = 0$ and $\frac{d\phi}{d\mathrm{x}}|_{\mathrm{x}=0} = 0.01$, the interactive equations, Eq.A.33 and Eq.A.34, can be solved by numerical method. For two different cases of $\frac{\lambda_{De}}{r_{Li}} = 5$ (extreme case) and $\frac{\lambda_{De}}{r_{Li}} = \frac{33\mu\mathrm{m}}{1.12\mu\mathrm{m}} = 0.03$ (STOR-M SOL parameter), the calculation results are shown in Fig.A.4 while the magnetic field directions, θ, are taking into account.

Referring to (a) and (b) of Fig.A.4, one can see that an ion flow makes a helical movement with the action of electrostatic force and magnetic field. The ion makes several rotations about the strong magnetic field line in (b) while it can't finish one rotation about the weak magnetic field in (a). The axis of the helical movement is the direction of magnetic field.

In plot (d), ion velocity fluctuation occurs in a strong magnetic field because while a steeper gradient of electric potential (see plot (c)) speeds up the ion with a smaller Larmor radius in a part of the orbit, it causes slowing down the particle in the other portion of the rotation in the oblique magnetic field.

Plot (e) compares the electron density distribution and ion density distribution for different magnetic field strengths. In the case of less magnetic field, $\gamma = 0.03$, the density distributions are very similar to the nonmagnetic sheath behavior. For $\gamma = 5$, the ion density fluctuates because of ion continuity equation. In both cases, the ion densities are always

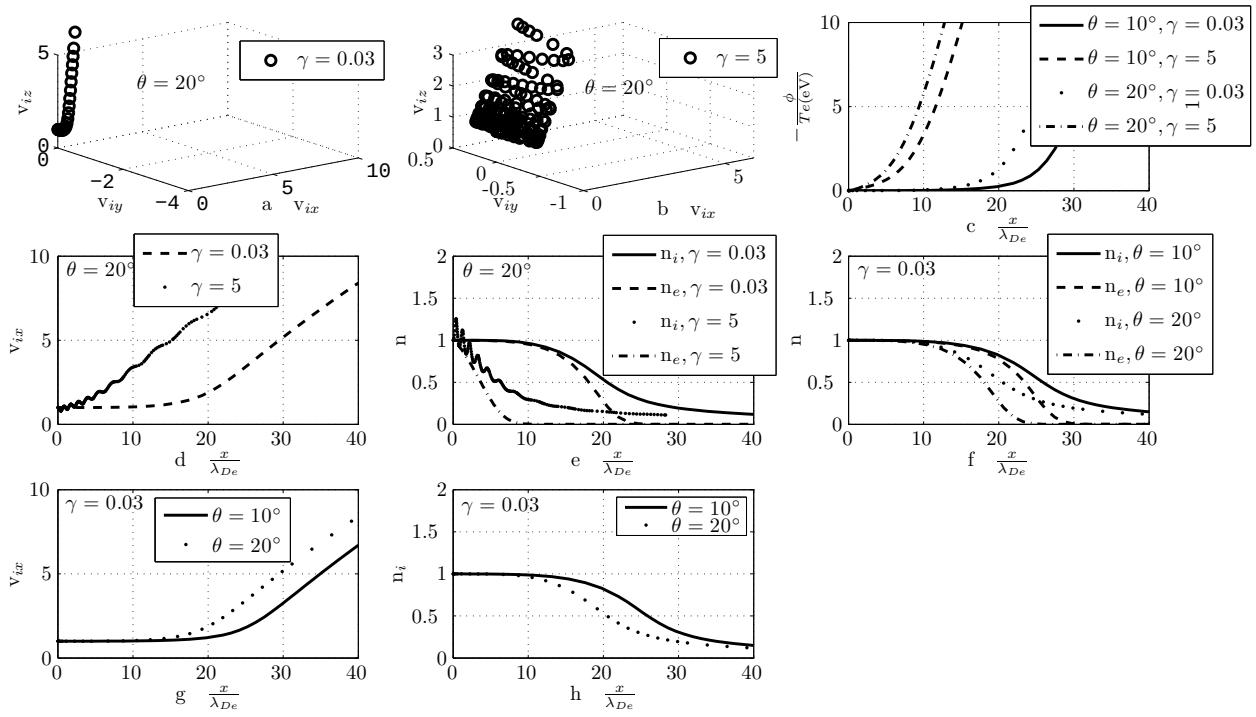

Figure A.4: Results from calculations for $\tau = 2$, or $T_{i0} = 2T_e$. (a): Ion helical motion in velocity space with $\gamma = 0.03$. (b): ion helical motion in velocity space with large magnetic field $\gamma = 5$ for $\theta = 20°$. (c): potential gradients with different magnetic field strengths and different magnetic field directions. (d) and (e): ion velocity distributions and the comparison of ion and electron density distributions inside the sheath with different γ values in a fixed magnetic field tilt, $\theta = 20°$. (f): ion and electron density distributions inside the sheath with different magnetic field directions and different magnetic field strengths. (g) and (h): ion velocity distributions, ion density distributions with different θ in a fixed magnetic field strength, $\gamma = 0.03$.

higher than the electron density in any given values of magnetic field as being suggested in the requirement of Bohm criterion in the nonmagnetic sheath region.

The ion density and electron density for different magnetic field directions in the fixed magnetic field strength, $\gamma = 0.03$, are shown in (f). n_i is always higher than n_e in the sheath regardless of the magnetic field direction as suggested by Bohm criterion. No fluctuations occur.

For a sheath with different magnetic field directions in a fixed magnetic field strength, $\gamma = 0.03$, the results of ion velocity distribution and ion density distribution are shown in (g) and (h). No fluctuation occurs up to 20° tilt of magnetic field line.

The electric potentials in a sheath with different magnetic field strengths and different orientations of magnetic field are compared in (c). The potential gradient is steeper when the magnetic field strength is larger or when the tilted angle of the magnetic field line is larger. From the plot (c), we learn that the size of the sheath layer decreases either due to

the increment of misalignment of magnetic field or due to the increment of magnetic field strength. The similar results were also reported in [54].

In conclusion, for the case of the STOR-M SOL parameter, $\gamma = 0.03$, no density and velocity fluctuation occurs up to 20° misalignment of the plate with magnetic field. The sheath layer is dependent not only on the plasma magnetization but also on the angle of magnetic field orientation.

Appendix B

Matlab Code for Estimating T_i

Proper data analysis is necessary to provide the ion temperature, T_i. Here Matlab scripts are used for smoothing, averaging, reconstruction, and ion temperature estimation within the given time window set by 'allDownlimit' and 'allUplimit' of the downstream data and the upstream data. T_i estimation from the fitted exponential slope is also included in the code. The code named as Ti_estimation.m is shown in Lst.B.1. The script does data smoothing, curve fitting, and ion temperature computing. #243127 on line 29 is the shot number of the STOR-M tokamak. The path of the file location should be provided on Line number 37. Column numbers of the data must be provided between lines 32 and 35 depending on the channels used in the DAQ. Current gain used in the OP-AMP should be provided on line 23. By providing the necessary information, T_i can be estimated. T_i regarding to the increasing and decreasing parts of V_{G1} can be calculated separately by removing one of the variables (*L, *R) inside each square bracket of lines between 92 and 94. DownIc in the code represents the downstream current and UpIc represents the upstream current from the output of the DAQ. The alphabets, L and R, represent the collector current regarding to the increasing and the decreasing parts of sweeping V_{G1} respectively. The code can be used for T_e estimation too. For electron temperature measurement, negative signs should be placed in front of the right side of the equations on lines 42 and 43. Necessary Matlab file, myginput.m, can be downloaded from Matlab file exchange. That file is for interactive graphical input of choosing the low limit and up limit of the slope manually. The codes are available in the file path `\\Spitzer\Work\LabOps\Equipment\STOR-M\ProbesinVacuum\bi_RFEA\MatlabCode`.

Script Lst.B.2 does averaging and reconstruction of the smoothed i_c generated by the upper part of Lst.B.1. i_c values regarding to L and R are outputted by Lst.B.2. The script is named as Avg_VG1base_func.m. avg_Point represents the number of average points. The input resistor of the OP-AMP should be provided on line number 6 of the code. The ratio of the V_{G1} value and the V_{G1} monitor value should be provided on line 7. The brief structure of the code (Lst.B.2) is that the collected currents, DownIc and UpIc, are averaged regarding to the rounded VG1 values as shown in the square box of Fig.B.1. Note: myinput.m, Ti_estimation.m, and Avg_VG1base_func.m should be located in the same folder.

Listing B.1: Matlab script for smoothing, averaging, reconstruction of the downstream current, upstream current, and T_i estimation for standard mode operation.

```
1  %Choose parameters for graphs (if you don't like the default values set by factory.
2  set(0,'defaultaxesfontsize',12);
3  set(0,'DefaultAxesFontName', 'latex')
4  set(0,'defaulttextfontsize',12);
5  set(0,'DefaultTextInterpreter', 'latex')
6  set(0,'DefaultFigureColor', 'White');
7  set(0,'defaultlinelinewidth',1);%2 default
8  set(0,'defaultlinecolor',[0 0 0])
9  set(0,'DefaultTextFontName','latex')
10 set(0,'DefaultLineMarkerSize',3); % Default size of graph markers
11 set(0,'DefaultAxesColorOrder',[0 0 0]);
```

```
set(0,'DefaultAxesLineStyleOrder',{'-'} ) ; %{'--','-',':', '-.'} Default line order, use line styles instead of colors for multiline plots
set(0,'DefaultLineLineStyle', '-')
set(0,'DefaultTextHorizontalAlignment', 'left');

clear
close all;

%This code does the smoothing, DC level shifting correction, local normalization, averaging, and reconstruction within the given time window set by 'allDownlimit', lower limit, and 'allUplimit', upper limit, of downstream ic and upstream ic.

Neg_1=[];%Neglect some part of the data (if disruption occurs). Gives integers regarding to number of crests of VG1. For good shot, just leave it empty.
avg_Point=1;%Averaging degree of the downstream and the upstream currents. In my case, I use 1.
icAtten=10;%Current gain used in OP-AMP
Avg_po =70;%Number of smoothing points

allDownlimit=0.01377;%Range of time window
allUplimit=0.01877;

FileName_1=num2str(243127);%Shot number

%Column that represents downstream current, upstream current, and VG1 (should be known from DAQ). Normally, time is in column 1.
T_col=1;%nth column of Time
Up_col=33;%nth column of Upstream ic
Down_col=32;%nth column of Downstream ic
VG1_col=31;%nth column of Sweeping VG1 monitor

FileDir_1=['\\cti\Wk\2011\September\133C' FileName_1];%File path of the stored data. You can see the file path in the "properties" after "right-clicking" on the data file.

A_1 = importdata(FileDir_1,'\t',22);%Import the output data of DAQ from the specific directory set by previous file path (set tab, \t, for delimiter, and exclude 22 rows for text)

T1_1_a1=A_1.data(:,T_col);%Time
UpIc1_1_a1=A_1.data(:,Up_col);%Upstream ic
DownIc1_1_a1=A_1.data(:,Down_col);%Downstream ic
VG11_1_a1=A_1.data(:,VG1_col);%VG1

%Cut unwanted portion of the downstream and upstream currents.
T1Index_1=find((T1_1_a1>allDownlimit)&(T1_1_a1<allUplimit));%Find indices for time window
T1_1=T1_1_a1(T1Index_1);%Time within the time window set by 'allDownlimit' and 'allUplimit'
UpIc1_1_a=UpIc1_1_a1(T1Index_1);%Upstream ic within the time window
DownIc1_1_a=DownIc1_1_a1(T1Index_1);%Downstream ic within the time window
VG11_1=VG11_1_a1(T1Index_1);%VG1 within the time window

DownIc1_1 = smooth(DownIc1_1_a,Avg_po);%Smooth downstream and upstream
UpIc1_1 = smooth(UpIc1_1_a,Avg_po);


sep_T2_1=T1_1;
sep_UpIc2_1=UpIc1_1;
sep_DownIc2_1=DownIc1_1;
sep_VG12_1=VG11_1;

%%%%%%%%%%%%%%%%%%%START RECONSTRUCTION%%%%%%%%%%%%%%%%%%%%%%%%%%%%%%%%%%%%%%%%

%Avg_VG1base_func.m file is required to run this part.
%Call Avg_VG1base_func.m function, and average and reconstruct the data. Moreover each array is separated into L, left side, and R, right sides regarding to decreasing and increasing parts of VG1 respectively.
```

```
[VG12L_XX_1,DownIc3L_XX_1,UpIc3L_XX_1,VG12R_XX_1,DownIc3R_XX_1,UpIc3R_XX_1] = Avg_VG1base_func(Neg_1,avg_Point,icAtten,sep_DownIc2_1,sep_UpIc2_1,sep_VG12_1);

VG12L_1=VG12L_XX_1;%Averaged and reconstructed left side VG1
DownIc3L_1=DownIc3L_XX_1;%Averaged and reconstructed left downstream ic
UpIc3L_1=UpIc3L_XX_1;%Averaged and reconstructed left upstream ic

VG12R_1=VG12R_XX_1;%Similarly for right side
DownIc3R_1=DownIc3R_XX_1;
UpIc3R_1=UpIc3R_XX_1;


figure(2);
subplot(2,2,1); plot(VG12L_1,DownIc3L_1,'ro')%Plot I-V curve for averaged and reconstructed left downstream ic
hold on;
subplot(2,2,2); plot(VG12R_1,DownIc3R_1,'ro')
hold on;
subplot(2,2,3); plot(VG12L_1,UpIc3L_1,'ro')
hold on;
title(['VG1 decreasing'])
subplot(2,2,4); plot(VG12R_1,UpIc3R_1,'ro')
hold on;
title(['VG1 increasing'])

%%%%%%%%%%%%%%%%%%START COMBINING LEFT AND RIGHT%%%%%%%%%%%%%%%%%%%%%%%%%%%%%%%%

%Attach left side and right side data of VG1, downstream ic, and upstream ic for estimating ion temperature, Ti. You can estimate Ti for left side and right side separately if you can get long and stable discharge. It is pretty hard in STOR-M tokamak. For simplicity, words, level-shift, normalized, averaged, and reconstructed, will not be used repeatedly here. It should be understood automatically that the parameters being used in here are last updated ones.
VG1L_Total_XX=[VG12L_1 VG12R_1];%Attach left VG1 and right VG1 into a single array.
DownIcL_Total_XX=[DownIc3L_1 DownIc3R_1];
UpIcL_Total_XX=[UpIc3L_1 UpIc3R_1];

uni_VG1L_Total_XX=unique(VG1L_Total_XX);%Take unique values of VG1 if VG1 has repeated values.
sort_VG1L_Total_XX=sort(uni_VG1L_Total_XX);%Sort VG1 by ascending order.
len_sortL_Total_XX=length(sort_VG1L_Total_XX);

sumL_Total_XX=0;

for j=1:len_sortL_Total_XX
    sumL_Total_XX=sumL_Total_XX+1;
    [lev_indexL_Total_XX]=find(VG1L_Total_XX-sort_VG1L_Total_XX(j)==0);%Find indices which point to a specific value of VG1
    DownIcL_Avg_shots_XX(sumL_Total_XX)=median(DownIcL_Total_XX(lev_indexL_Total_XX));%Median value of downstream ic regarding to a specific value of VG1
    UpIcL_Avg_shots_XX(sumL_Total_XX)=median(UpIcL_Total_XX(lev_indexL_Total_XX));%Similarly for upstream ic
    VG1L_Avg_shots_XX(sumL_Total_XX)=median(VG1L_Total_XX(lev_indexL_Total_XX));%Similarly for VG1 (this line is not required)
end

%%%%%%%%%%%%%%%%%%%%%%%START Ti ESTIMATION%%%%%%%%%%%%%%%%%%%%%%%%%%%%%%%%%%%%%%

%myginput.m file from MATLAB file exchange is required to run this section
%In our case, the up limit and low limit of ic for Ti estimation cannot by judged by ln(-1)) and (ln(-4)) suggested by M. Kocan in Influence of Impurities on Ion Temperature...
%Choosing the up limit and low limit by eyes is the best way so far.
    figure(3);

    subplot(2,2,1);semilogy(VG1L_Avg_shots_XX,DownIcL_Avg_shots_XX,'bo')
    subplot(2,2,3); semilogy(VG1L_Avg_shots_XX,UpIcL_Avg_shots_XX,'ro')
    zoom on;
```

```
120     waitfor(gcf,'CurrentCharacter',13)%This function allows zoom in and zoom out before graphical input of low limit and up limit. After doing so, press enter on the graph. The crosshair pointer appears on the graph for locating low and up limit of ic to be curve-fitted for Ti estimation.
121     zoom reset
122     zoom off
123     [In_x_Down,In_y_Down] = myginput(2,'fullcrosshair');%wait graphical manual inputs for determining the lower and upper limit of I-V downstream curve to do graph fitting
124     hold on;
125
126     [In_x_Up,In_y_Up] = myginput(2,'crosshair');% wait graphical manual inputs for determining the lower and upper limit of I-V upstream curve to do graph fitting
127     hold on;
128
129     x_Down_min=min(In_x_Down);%Low threshold limit of downstream ic for exponential curve fitting
130     x_Down_max=max(In_x_Down);%up threshold limit of downstream ic for exponential curve fitting
131
132     x_Up_min=min(In_x_Up);%Similarly for upstream ic
133     x_Up_max=max(In_x_Up);
134
135     In_DetermineIndexDownL=find((VG1L_Avg_shots_XX>=min(In_x_Down))&(VG1L_Avg_shots_XX<=max(In_x_Down)));%Find indices between low limit and up limit chosen by graphical input
136     In_best_fit_VG1L_DownIcL_XX=VG1L_Avg_shots_XX(In_DetermineIndexDownL);%Remove VG1 values beyond the low and up limit.
137     In_r_best_fit_DownIcL_XX=DownIcL_Avg_shots_XX(In_DetermineIndexDownL);%Remove downstream ic beyond the low and up limit.
138
139     In_best_fit_pcoeff_DownIcL_XX=polyfit(In_best_fit_VG1L_DownIcL_XX,log(In_r_best_fit_DownIcL_XX),1);%Required coefficients for exponential curve fitting
140     In_best_fit_DownIcL_XX=exp(In_best_fit_pcoeff_DownIcL_XX(2)).*exp(In_best_fit_pcoeff_DownIcL_XX(1)*In_best_fit_VG1L_DownIcL_XX);%Exponentially fitted downstream ic
141
142     In_DetermineIndexUpL=find((VG1L_Avg_shots_XX>=min(In_x_Up))&(VG1L_Avg_shots_XX<=max(In_x_Up)));%Similarly for upstream
143     In_best_fit_VG1L_UpIcL_XX=VG1L_Avg_shots_XX(In_DetermineIndexUpL);
144     In_r_best_fit_UpIcL_XX=UpIcL_Avg_shots_XX(In_DetermineIndexUpL);
145
146     In_best_fit_pcoeff_UpIcL_XX=polyfit(In_best_fit_VG1L_UpIcL_XX,log(In_r_best_fit_UpIcL_XX),1);
147     In_best_fit_UpIcL_XX=exp(In_best_fit_pcoeff_UpIcL_XX(2)).*exp(In_best_fit_pcoeff_UpIcL_XX(1)*In_best_fit_VG1L_UpIcL_XX);
148
149     %Estimate Ti
150     In_knee_point_VG1L_DownIcL_XX=In_best_fit_VG1L_DownIcL_XX(1);%VG1 located at the low limit of downstream ic or V_shift.
151     In_DownIcL_0_XX=In_best_fit_DownIcL_XX(1);%Downstream at V_shift
152     In_DownIcL_Ti_XX=-(In_best_fit_VG1L_DownIcL_XX-In_knee_point_VG1L_DownIcL_XX)./(log(In_best_fit_DownIcL_XX/In_DownIcL_0_XX));%Downstream Ti calculation from the fitted slope of downstream ic
153     In_DownIcL_Ti_XX=In_DownIcL_Ti_XX(isfinite(In_DownIcL_Ti_XX));%Eliminate infinite or nan values.
154     In_DownIcL_Ti_XX(In_DownIcL_Ti_XX<0) = [];%Eliminate negative value.
155     Avg_DownIcL_Ti=mean(In_DownIcL_Ti_XX);%Downstream Ti
156
157     In_knee_point_VG1L_UpIcL_XX=In_best_fit_VG1L_UpIcL_XX(1);%Similarly for upstream
158     In_UpIcL_0_XX=In_best_fit_UpIcL_XX(1);
159     In_UpIcL_Ti_XX=-(In_best_fit_VG1L_UpIcL_XX-In_knee_point_VG1L_UpIcL_XX)./(log(In_best_fit_UpIcL_XX/In_UpIcL_0_XX));
160     In_UpIcL_Ti_XX=In_UpIcL_Ti_XX(isfinite(In_UpIcL_Ti_XX));
161     In_UpIcL_Ti_XX(In_UpIcL_Ti_XX<0) = [];
162     Avg_UpIcL_Ti=mean(In_UpIcL_Ti_XX);
163
```

```
164      %Semilog plot
165      figure(4);
166      subplot(2,2,1);semilogy(In_best_fit_VG1L_DownIcL_XX,In_best_fit_DownIcL_XX,'c')%↩
             Exponential fitted downstream ic-VG1 curve
167      hold on;
168      subplot(2,2,1);semilogy(In_best_fit_VG1L_DownIcL_XX,In_r_best_fit_DownIcL_XX,'o')%↩
             Downstream ic-VG1 curve
169      title(['DownTi=' num2str(Avg_DownIcL_Ti) 'plot' num2str(FileName_1)])%Print ↩
             downstream Ti and shot number on the graph
170
171      subplot(2,2,3);semilogy(In_best_fit_VG1L_UpIcL_XX,In_best_fit_UpIcL_XX,'c')%↩
             Similarly for upstream ic
172      hold on;
173      subplot(2,2,3);semilogy(In_best_fit_VG1L_UpIcL_XX,In_r_best_fit_UpIcL_XX,'o')
174      hold on;
175      title(['UpTi=' num2str(Avg_UpIcL_Ti)])%Print upstream Ti
176
177     %Linear plot
178      subplot(2,2,2);plot(VG1L_Avg_shots_XX,DownIcL_Avg_shots_XX,'v','MarkerSize',10)%↩
             Similarly for linear plot
179      hold on;
180      subplot(2,2,2);plot(In_best_fit_VG1L_DownIcL_XX,In_best_fit_DownIcL_XX,'k','↩
             Linewidth', 3)
181      hold on;
182      xlabel('$V_{G1}(\mbox{V})$')%Label on x-axis
183      ylabel('$i_c(\mbox{A})$')%Label on y-axis
184
185      subplot(2,2,4);plot(VG1L_Avg_shots_XX,UpIcL_Avg_shots_XX,'^','MarkerSize',10)
186      hold on;
187      subplot(2,2,4);plot(In_best_fit_VG1L_UpIcL_XX,In_best_fit_UpIcL_XX,'k','Linewidth',↩
             3)
188      hold on;
189      xlabel('$V_{G1}(\mbox{V})$')
190      ylabel('$i_c(\mbox{A})$')
```

Listing B.2: Matlab code for Avg_VG1base_func function.

```
1
2  %Left side of the equation -> output parameters, right side of the equation -> input ↩
       parameters
3  function [VG12L,DownIc3L,UpIc3L,VG12R,DownIc3R,UpIc3R] = Avg_VG1base_func(Neg,avg_Point↩
       ,icAtten,sep_DownIc2,sep_UpIc2,VG12)%Input parameters or arrays from previous code
4
5  %Convert actual values from measured data.
6  Thev_Res=15000;%Input resistance used at the input of op-amp
7  vg1beta=29*avg_Point;%Here avg_Point is used for degree of rounding different VG1 to ↩
       nearest integers values for averaging ic regarding to rounded VG1.
8  sep_UpIc2=sep_UpIc2/(icAtten*Thev_Res);%Convert voltage to current and divided by gain ↩
       of op-amp for upstream ic
9  sep_DownIc2=sep_DownIc2/(icAtten*Thev_Res);%Convert voltage to current and divided by ↩
       gain of op-amp for downstream ic
10 VG12a=VG12*vg1beta;%Convert to VG1 (included avg_Point factor) from VG1 monitoring ↩
       output.
11 VG12aa=VG12a/avg_Point;%Convert to actual VG1
12
13 %Reconstruct the VG1 for VG1-base averaging
14 VG12b=round(VG12a);%Rounding different VG1 to nearest integers
15 VG12c=VG12b/avg_Point;%Return Rounded VG1 to its actual value
16 uni_VG12=unique(VG12c);%Take unique rounded values of VG1 if VG1 has repeated values
17 sort_VG12=sort(uni_VG12);%Sort unique rounded values of VG1 by ascending order.
18 len_sort=length(sort_VG12);
19
20 sumLL=0;
21 sumRR=0;
22
23 %Average downstream and upstream currents regarding to each specific
```

```
%value of sort_VG12
for i=1:len_sort
    clear('*XX')%Remove all arrays which names are ended with XX
    [lev_index_XX]=find(VG12c-sort_VG12(i)==0);%Find indices which indicate each single value of VG1

    sumL=0;
    sumR=0;
    %Protect overflowing while separating ic regarding to increasing and decreasing part of VG1.
    cut_upperbound=find(lev_index_XX>=(length(VG12c)-5));%Find indices that is greater than total data size-5
    lev_index_XX(cut_upperbound)=[];%Remove overflow data

%%%%%%%%%%%%%%%%%%%%%START SEPARATING ic INTO TWO PARTS%%%%%%%%%%%%%%%%%%%
```

```
76          UpIc3R(sumRR)=mean(sep_UpIc2(temp_lev_indexR_XX));
77
78      end
79  end
80
81  %Return empties if there are no input parameters
82  if ~exist('VG12L','var')
83      VG12L=[];
84  end
85  if ~exist('DownIc3L','var')
86      DownIc3L=[];
87  end
88  if ~exist('UpIc3L')
89      UpIc3L=[];
90  end
91  if ~exist('VG12R','var')
92      VG12R=[];
93  end
94  if ~exist('DownIc3R','var')
95      DownIc3R=[];
96  end
97  if ~exist('UpIc3R','var')
98      UpIc3R=[];
99  end
```

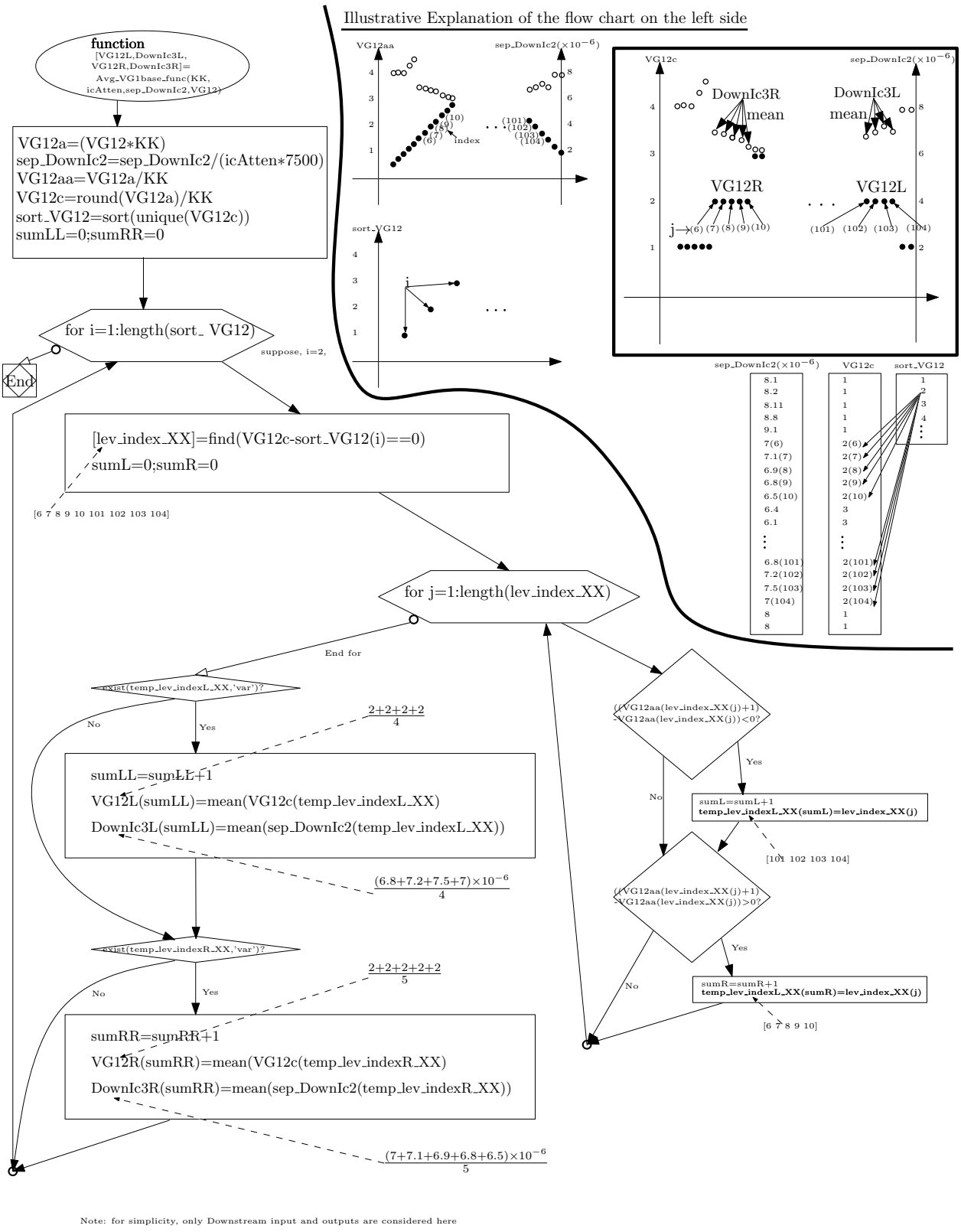

Figure B.1: Simplified flow chart diagram of the averaging code (Avg_VG1base_func.m).